Flow-induced Alignment in Intrinsically Anisotropic Polymeric Materials

Thesis by

Rangaramanujam Mudumbai Kannan

In Partial Fulfillment of the Requirements

for the Degree of

Doctor of Philosophy

California Institute of Technology

Pasadena, California

1995

(Defended 13 May 1994)

To my mother Santhalakshmi, and my father Rangaramanujam:

For their love and encouragement

Acknowledgments

I am extremely grateful to my advisor Prof. Julia Kornfield for giving me an opportunity to work with her and learn several experimental techniques. She has been a great source of inspiration, guidance and encouragement. Thanks, Julie, for all the fun. I have learned many valuable lessons which I will cherish for the rest of my life. I would also like to thank my commitee members Prof. John Brady, Prof. Rick Flagan and Prof. Zhen-Gang Wang for their helpful comments and encouragement. It was a great pleasure discussing my work with Prof. Masao Doi.

I owe most of my "success" to my parents. They placed my interests before theirs, and have made a lot of sacrifices to help me pursue my career. They have always been there whenever needed and provided me with inspiration, guidance and total support. I would like to thank my sister (Akhila) and brother (Srivatsan) for being great friends. I am thankful to Sujatha (SK) for being supportive and fun during the last few months.

I have thoroughly enjoyed my years at Caltech, which is largely due to a great set of friends. I would like to thank Chung, Vinay, Susan, Barbara and Ramanan & Steve (the members of the Kornfield group), for several valuable discussions. Special thanks are due to Suresha Guptha for all the help during the preparation of the manuscript. Thanks are also due to Janet, Alicia, Maha and Jose, the undergrads I had a chance to interact very closely during their SURFing.

Flow-induced Alignment in Intrinsically Anisotropic Polymeric Materials

Rangaramanujam M. Kannan

Advisor: Julia A. Kornfield

Abstract

To understand the processing behavior of complex polymeric materials, it is imperative that we understand the distinct underlying molecular and microstructural contributions to macroscopic mechanical response. We have developed rheo-optical methods to isolate the dynamics at such length scales, by combining conventional mechanical testing with polarimetry. The rheology and flow-induced alignment in side-group liquid-crystalline polymers (SG-LCPs) and lamellar diblock copolymers (BCPs) have been investigated using the rheo-optical apparatus.

The rheology of SG-LCPs arises from a combination of the polymeric nature of the backbone, the ordering tendency of the mesogens, and the coupling between the two introduced by the spacer. Contrary to previous studies, we find that the nematic order *can* significantly affects the macroscopic viscoelastic response in SG-LCP melts. In the nematic state, we have discovered that oscillatory shear is effective in inducing macroscopic orientation of the sample. Shear flow may prove to be an economical, efficient way to obtain macroscopically aligned SGLCPs, which have potential as optical data storage media and nonlinear optical materials. In contrast to magnetic field induced alignment, the mechanism of shear induced alignment appears to be

driven by the distortion of the polymer backbone.

We study the mechanisms of flow-induced alignment in a poly(ethylenepropylene)-poly(ethylethylene) lamellar diblock copolymer, which produce macroscopic alignment with lamellae normal along the shear gradient direction ('parallel' alignment), or along the vorticity direction ('perpendicular' alignment). We accomplish this by monitoring the evolution of the microstructure and viscoelasticity *in situ* during the alignment process. Our results suggest that 'parallel' alignment occurs due to irreversible 'rocking' of grains which tends to align the grains along the shear direction, whereas 'perpendicular' alignment occurs at conditions where the microscale deformation is nearly homogeneous.

Contents

List of Figures

List of Tables

Chapter 1

Introduction

1.1 Viscoelasticity

The shear stress in a viscous liquid depends only on the the rate of deformation. The mechanical work spent in producing the deformation is dissipated instantaneously. The relationship between the shear stress and the rate of deformation is characterized by Newton's law of viscosity. The stress in a perfect solid, elastic body depends on the magnitude of deformation. The mechanical work is stored in the form of elastic energy. When the deformation is removed, the material returns to its original shape ('perfect' memory). Under stress, polymeric materials exhibit both viscous dissipation and elastic energy storage, and thus are termed viscoelastic [4]. In these materials the stress depends on the history of deformation, making the viscoelastic response more complex compared to a liquid or a solid. It takes a polymer molecule a certain time, referred to as terminal relaxation time, to lose its memory. At strain rates rapid compared to the terminal relaxation time, the material behaves like a solid, and at slower rates, it behaves essentially like a liquid. Rheology is the study of deformation of materials under flow.

The viscoelastic behavior of polymers can be classified into two regimes depending on the nature of deformation : linear and nonlinear [2]. When the deformation is sufficiently weak, such that the molecules are disturbed from their equilibrium conformations only to a negligible extent, the response is said to be linear. In melts, which exhibit a 'fading' memory and can flow, this behavior is observed at 'small' strains and/or at 'slow' deformation. One consequence of linear behavior is that the viscoelastic properties are independent of strain. For example, in response to a

sinusoidal strain $\gamma(t) = \gamma_o \sin \omega t$, the shear stress σ_{12} is given by,

$$\sigma_{12} = \gamma_o[G' \sin\omega t + G'' \cos\omega t] \tag{1.1}$$

where G' is the storage modulus describing the elastic response, and G'' is the loss modulus describing the viscous response. When the deformation is sufficiently large or rapid, the response becomes a function of the the size, rate and the kinetics of deformation and the response is said to be nonlinear. One familiar consequence of nonlinear behavior is the presence of 'normal' stresses. These are the reason for the 'Weissenberg' effect, which is the tendency of an elastic liquid to rise up around a rotating rod partially immersed in it. Flow provides a powerful means not only in characterizing the material, but also in manipulating the properties of the polymer. For example, through appropriate processing, polyethylene can be made into fibers with tensile properties better than steel at a fraction of the price. Therefore, understanding the rheological properties becomes crucial in industrial processes such as injection molding, extrusion and fiber spinning. Studying the viscoelastic properties of polymers is crucial to understanding and manipulating the rheology of these materials during processing. While deformation in the linear regime can be useful in characterizing the material, deformation in the nonlinear regime can be used to enhance the properties of the polymer. In this work, we will study polymers both in the linear and nonlinear regime to address both these aspects. While the mechanical properties are useful in studying the macroscopic response of the polymer, they do not provide much insight into why the material behaves the way it does. For example,

in polymers which possess intrinsic anisotropy, the macroscopic mechanical properties can have various underlying molecular and microstructural contributions which contribute differently to stress depending on the time scale, temperature, strain amplitude etc. The ultimate objective of this thesis is to understand the physics of flow behavior of polymeric materials from a microscopic point of view, to evolve strategies for manipulating their processing properties. Studying just the mechanical properties does not reveal *why* a material behaves in a certain manner. Therefore, we use a combination of mechanical and optical methods to understand the molecular origin of macroscopic viscoelasticity.

1.2 Optical Rheometry

Optical rheometry involves the study of interaction of light with a material under flow, to determine the state of fluid microstructure [4]. In addition to providing important, complimentary information to mechanical testing, optical methods offer some distinct advantages:

- Ability to isolate the dynamics of separate constituents in multicomponent systems using labeling techniques
- Ability to isolate microstructural changes at different length scales by choice of the optical property and the wavelength of light used
- Provide faster response times and higher sensitivity

- In some cases, experimental observables can be directly related to parameters predicted by theory.

In general, optical rheometric techniques can be divided into two categories:

- Polarimetric experiments where the change in the polarization of light emanating from the sample are studied
- Light scattering or diffraction experiments where the angular dependence of light scattered or diffracted from the sample are analyzed.

In our work, we combine polarimetric methods with mechanical measurements. Under flow, the optical properties of the material (*e.g., refractive index*) become anisotropic. By impinging the sample with a well-defined polarized light and analyzing the changes in the state of polarization (*e.g., anisotropy in refractive index*) induced by flow, we gain information about the fluid microstructure. Using polarization-modulation scheme of Johnson, Frattini and Fuller [17], we measure the real and imaginary parts of the anisotropic refractive index tensor ($\mathbf{\Delta n}$), in a rapid, sensitive manner. In general, ($\mathbf{\Delta n}$) can be described by

$$\mathbf{\Delta n} = \mathbf{\Delta n'} + \mathbf{i}\mathbf{\Delta n''}. \tag{1.2}$$

The real part of the anisotropic refractive index tensor ($\mathbf{\Delta n'}$) describes the anisotropy in the retardation of light and is referred to as Birefringence. The imaginary part of the anisotropic refractive index tensor ($\mathbf{\Delta n''}$) describes the anisotropy in the attenuation of the sample and is referred to as Dichroism. In general, birefringence can

arise from two distinct origins. Intrinsic birefringence arises due to the anisotropic orientation of the polymer molecules. Form birefringence arises due to the shape, spatial arrangement of the microstructure suspended in a medium when there is a refractive index mismatch between the two media. Dichroism can also arise from two distinct origins. Consumptive dichroism arises due to the anisotropic absorption of light at a given wavelength. Conservative dichroism arises from the scattering of the polarized light by the sample due to anisotropy in the shape, or spatial arrangement [4].

At a wavelength where a strong vibrational absorption occurs, dichroism arises primarily from the anisotropic orientation of the specific chemical moiety which contributes to the absorption. Using a combination of deuterium labeling and infrared (IR) light at the carbon-deuterium absorption wavelength, IR dichroism can be used to study the dynamics of individual components in a multicomponent system [20], or even different parts of a polymer chain [6, 7].

When both birefringence and stress arise from the distortion of the chain configuration of the polymer, they can be related to each other through the familiar stress-optical rule (SOR). The stress-optical rule supposes that the deviatoric part of the refractive index tensor and the stress tensor (τ) are coaxial, *i.e.,* they have the same principal axes, and that the differences in principal stresses are proportional to the corresponding differences in the principal values of the refractive index tensor ($\mathbf{n}$).

$$\mathbf{n} - \mathbf{n_m I} = \mathbf{C}(\tau + \mathbf{pI}), \tag{1.3}$$

where n_m is the mean refractive index and p is the hydrostatic pressure [4, 31]. For many materials the simple, linear relationship has a wide range of validity. For homopolymer melts and solutions, it is found to be independent of molecular weight and has a weak temperature dependence. SOR serves as a useful tool to measure the shear stress and normal stress differences in polymeric materials, by measuring birefringence.

In complex polymer melts, such as blends or intrinsically anisotropic polymers, the SOR should be expected to breakdown in general. This is due to the fact that birefringence can have several contributions due to the individual species, intrinsic and form contributions due to the microstructure. Throughout the course of this thesis, we will illustrate how the breakdown in SOR for complex polymer melts, when characterized in a systematic and quantitative manner, can reveal the response arising from these distinct origins.

1.3 Polymers of Interest

In our work, we study polymers which possess an intrinsic ability to order at a microscopic level. In particular we study side-group liquid-crystalline polymers and block copolymers. Side-group liquid-crystalline polymers (SG-LCPs) consist of a polymeric backbone, with the liquid-crystalline molecules (mesogens) attached as pendant to the

backbone, through the use of flexible molecules known as spacer. We focus on thermotropic SG-LCPs, which are nematic. This means that they exhibit orientational order with no positional order (nematic) below a certain temperature (thermotropic). Block copolymers (BCPs) are made of sequences of chemically distinct repeat units which are covalently linked. Below a certain temperature known as the order-disorder transition (ODT), the two blocks segregate into ordered microphases. The morphology of the ordered microphase depends on the relative length of the constituent blocks. We focus on diblocks which are nearly symmetric. They form lamellar microphases.

1.4 Thesis Synopsis

This thesis deals with understanding the microscopic origin to macroscopic viscoelasticity. It can be classified into three parts:

- Development and demonstration of the rheo-optical apparatus
- Rheology and flow-induced alignment in side-group liquid-crystalline polymers
- Mechanism of flow-alignment in lamellar block copolymers

In the first part, we address the motivation behind the development of experimental tools to study mechanical and optical properties simultaneously, quantitatively, and along different orthogonal projections. We describe the two rheo-optical apparatus we have developed in our lab (Chapter 2). In chapters 3 and 4, we illustrate the applications of the rheo-optical apparatus by applying it to study homopolymer melts, miscible blends, block copolymers and side-group liquid crystalline polymers.

In chapter 3, we show how the stress-optical rule can be applied to study normal stresses in homopolymer melts in a quantitative manner to verify constitutive relationships. In chapter 4, we demonstrate how the failure of the stress-optical rule can be used to isolate molecular and microstructural response in complex polymer melts.

In the second part, we discuss several new, intriguing aspects on the rheology of SG-LCPs. The rheology of these materials arises from a combination of the polymeric nature of the backbone, ordering tendency of the mesogens and the nature of the coupling between the two introduced by the spacer. In Chapter 5, we show how the nematic ordering is manifested in the flow behavior in the pretransitional regime, and in the nematic state. We have discovered that oscillatory shear flow can induce macroscopic alignment in SG-LCPs. We use rheo-optical methods to study the factors that influence the mechanism of alignment (Chapter 6).

In the third part, we shift our focus to lamellar diblock copolymers, which show some analogy to SG-LCPs in terms of rheology (Chapter 7). While the phenomenon of flow-induced alignment in these systems has been known for a long time, the *mechanism* of alignment is not clearly understood. In specific, using rheo-optical methods, we seek to study the mechanism responsible for 'flipping', whereby the lamellar orientation can be flipped by 90°C, simply by changing the frequency.

Bibliography

[1] Ferry, J. D., *Viscoelastic Properties of Polymers*, 3rd ed. Wiley, New York **1980**.

[2] Dealy, J .M.; Wissbrun, K. F., *Melt Rheology and Its Role in Plastics Processing*, van Nostrand Reinhold, **1990**.

[3] Fuller, G. G., *Ann. Rev. Fluid Mech.*, **1990**, 22, 387.

[4] Johnson, S. J.; Frattini, P. L.; Fuller, G. G., *J. Colloid Sci.*, **1985**, 104 (2), 440.

[5] Kornfield, J. A.; Fuller, G. G.; Pearson, D. S., *Macromolecules*, **1989**, 22 (3), 1334.

[6] Ylitalo, C. M.; Fuller, G. G.; Abetz, V.; Stadler, R; Pearson, D. S., *Rheo. Acta*, **1990**, 29 (6), 543.

[7] Kannan, R. M.; Zewail, M.; Kornfield, J. A., "Infrared dichroism studies of the middle and the end segments of a polystyrene chain in a melt," unpublished results.

[8] Janeschitz-Kriegl, H., *Polymer Melt Rheology and Flow Birefringence*, **1983** Springer-Verlag, New York.

Chapter 2

Development of the Rheo-optical Apparatus

2.1 Motivation

Rheology of complex polymer melts have several underlying molecular and microstructural contributions. To understand the behavior of these materials under flow, and to describe how their properties are modified by flow, it is imperative that we isolate the qualitatively different contributions to the viscoelastic properties. For example, in a microphase-separated block copolymer or liquid-crystalline polymer, macromolecular contributions to the viscoelasticity must be understood in relation to meso-structural contributions, which in turn are related to still larger scale dynamics of defect structures [1, 2, 3]. The challenge we face as rheologists is to develop experimental methods to discriminate among such dynamics and relate them to macroscopic flow behavior.

A variety of optical methods have been established to obtain the selective information required regarding the fluid microstructure during flow (for a recent review, see Fuller [4]). Birefringence is used to characterize molecular and microstructural orientation [5, 6, 7, 8, 9]. The effect of flow on the orientation of selected molecular species or segments can be probed by infrared dichroism [10, 11, 12], anisotropy in Raman scattering [13], or fluorescence anisotropy [14]. Light, X-ray, and neutron scattering are used to monitor effect of flow on the size and orientation of microstructures ranging from micron scale (e.g., compositional heterogeneities [15, 16]), to nanometer scale (e.g., microphase structure in block copolymers) [17]. Microscopy is used to visualize the formation and destruction of structures in the fluid, e.g., orientation patterns or disclination lines in a liquid crystal [18, 19].

In the vast majority of rheo-optical studies the mechanical and optical measure-

ments are conducted separately. This has limited the type of phenomena that can be examined. When nonlinear responses are investigated or when samples evolve with time due to chemical or flow-induced changes, it is essential that the conditions of the optical and mechanical experiments be identical to make quantitative comparisons; to ensure that conditions are indeed identical, it is necessary to make the two types of measurements at the same time [6, 7, 20]. To address these needs, we focus on two aspects : First, we want to be able to perform optical and mechanical measurements simultaneously and quantitatively. Second, we want to be able to observe different orthogonal projections of the anisotropic refractive index tensor. The rheo-optical apparatus will be used to gain a molecular view of macroscopic viscoelasticity in polymer melts.

We focus on polymer melts, and describe the development of instruments that are particularly well suited to study their dynamics. Although the general approach we describe can be extended to a variety of optical methods, we show examples that use polarimetry, i.e., analysis of changes in the polarization state of light upon propagating through the sample to determine the anisotropy of the optical properties of the material. We integrate optical arrangements for measuring transient flow birefringence and dichroism with a commercial rheometer that is modified to accommodate optical measurements. Two different configurations are described. One provides simultaneous birefringence and dichroism measurements using a single optical train with either visible or infrared light. This instrument is well suited to problems in which the isolation of distinct relaxations requires selectivity based on length scale

and/or molecular structure. The other optical rheometer probes the sample using two orthogonal optical axes at the same time. This fully characterizes the deviatoric refractive index tensor, and consequently gives a more complete picture of the dynamics of the fluid microstructure. This approach is well suited to determine, for example, the complete stress tensor in transient flow of materials that obey the stress optic rule or the evolving state of alignment of the ordered microstructure in a block copolymer during flow.

In this chapter we describe the development of the two optical rheometers, then illustrate how the stress-optical signature of each of these systems reveals their molecular and microstructural dynamics.

2.2 Experimental Methods

To perform simultaneous dynamic optical and mechanical measurements, we use optical trains for polarization-modulation polarimetry, built around a conventional dynamic mechanical testing system, the Rheometrics Solids Analyzer (RSAII). While this general approach is compatible with a variety of mechanical rheometers, it is worth noting that the RSAII offers the following features that facilitate integrated rheo-optical measurements: 1) the raw signals from the displacement and force transducers are readily accessible, so they can be acquired simultaneously with separate optical signals; 2) the shear sandwich geometry provides rectilinear flow, which makes it convenient to observe optical anisotropy in the 1,2-plane and/or in the 1,3-plane (Figure 2.3); 3) the flow cell is accessible for viewing over an angular range of more

than 270° about the flow direction, providing clear lines of sight along both the velocity gradient and vorticity axis of the flow cell, or any axis in between; and 4) the environmental chamber and flow cell are readily modified to provide access for the optical beam(s), so that the operating temperature range of the RSAII is retained (-100°C to 400°C, in an air or inert atmosphere).

We perform all our shearing experiments in oscillatory mode using a shear sandwich fixture. The instruments allows us to characterize four decades of dynamic response, from 0.001 to 100 rad/s. Two temperature transducers (PRT and Type J thermocouple) are used to monitor the temperature near the flow cell; the PRT is used for feedback control. The uniformity and stability of the temperature is specified to be ±0.5°C. Displacement amplitudes of 0.001–0.5 mm can be applied; the standard gap widths of the shear flow cell are 0.5, 1 and 2 mm. In order to facilitate optical measurements, custom shear sandwich fixtures were fabricated with the plates replaced by polished CaF_2 windows. The thickness of the windows can be adjusted to obtain gap sizes smaller than 0.5 mm. The force transducer has a range of 1 g to 1 kg force. The RSAII forms the center piece for both the rheometers that will be described in the next two sections. Only minor modifications to the RSA-II were required to accommodate simultaneous optical measurements. To obtain a clear optical path through the flow cell, apertures were cut through the walls of the environmental chamber and covered with NaCl windows.

2.3 Single-axis Optical Rheometer

The single axis instrument, shown schematically in Figure 2.1, is equipped with two optical sources: a helium-neon (HeNe) laser (633nm) and an infrared diode laser that operates at the wavelength of a carbon-deuterium stretching absorption (4.53μm) (Laser Photonics L5820 system equipped with a lead salt diode that has an operating range from 2170-2255 cm^{-1}). The arrangement of the polarizing and analyzing optics (before and after the flow cell) is that developed by Johnson, Frattini and Fuller [21] to achieve simultaneous measurement of transient birefringence and dichroism, and extended to infrared polarimetry by Kornfield, Fuller and Pearson [11]. The advantage of this arrangement arises from the use of a modulator to provide a periodic variation in the polarization state of the light incident on the sample. This provides for the high sensitivity and speed of the measurements.

The polarization modulating optics consist of an achromatic, Brewster-effect polarizer made of CdTe (provides polarization ratio of 450:1 at 633nm and 1000:1 at 4.53μm), oriented parallel to the flow direction taken as 0° (Cleveland Crystals Model IR 1600), a photoelastic modulator (PEM) oriented at 45° with respect to the flow direction (37 kHz, zinc-selenide, Hinds Model PEM-80 Series II, ZS 4560), and a quarter-wave plate oriented at 0° (Melles-Griot 02WRM005 at 633nm, uncoated MgF_2 plates at 4.53 μm). After passing through the sample, the beam is split into two parts using a beam splitter. The intensity of the transmitted light is primarily sensitive to the anisotropic attenuation of the sample (dichroism) and is measured at detector D1 (Figure 2.1). The reflected light is passed through a circular polarizer (Meadowlark

Model BK7 at 633 nm) (or a combination of a quarter waveplate and a polarizer oriented at 45° with respect to each other) and is sensitive primarily to the anisotropic retardation of the sample (birefringence) and is measured at detector D2. Silicon photodiodes are used for 633nm (Analog Modules Model 710-167), and indium antimonide detectors are used for 4.5μm (EG&G Judson Model J-10D-M208T-R01M-45)

To facilitate switching between visible and infrared measurements, most of the optics are compatible with both modes of operation. The modulator is made of ZnSe, which is transparent to visible and infrared light; the retardation amplitudes required at 630nm and 4.5μm are both within the operating range of its piezo-electric driver. The windows on the environmental chamber and flow cells are NaCl and CaF_2, which are transparent to the wavelengths of interest. Therefore, few adjustments are required to switch between operating at visible and infrared wavelengths: the pair of quarter wave retarders and the detectors used must be appropriate to the operating wavelength and the modulator must be adjusted to provide the appropriate retardation amplitude.

The detected intensity is demodulated, as described earlier [21], using a low-pass filter (Rockland Model 442 with cut-off set to 100 Hz) to determine the mean intensity I_{dc}, and four lock-in amplifiers (Stanford Research Model SR510)(two each for each detector), two locked to the reference frequency f of the PEM and the other two locked to $2f$. The first (I_{11}) and second (I_{21}) harmonics of the intensity from the dichroism detector D1, and the first (I_{12}) and second (I_{22}) harmonics of the intensity from the birefringence detector D2 are determined using the lock-in amplifiers. The

amplitude A of the PEM is adjusted so that I_{dc} is independent of the birefringence of the sample at that wavelength. Ideally, this corresponds to A set to the first zero of $J_o(A)$, where J_o is the Bessel function of the first kind evaluated at A.

2.3.1 Data Acquisition and Analysis

The signals from the displacement and force transducers, the low-pass filter and the lock-in amplifiers are recorded by a microcomputer (Macintosh IIci with National Instruments NB-MIO-16XL and NB-DMA8G A/D and DMA boards) at a rate that provided 128 points per cycle of the oscillatory strain at frequency ω. The strain, stress, $R_{11} \equiv I_{11}/I_{dc}$, $R_{21} \equiv I_{21}/I_{dc}$, $R_{12} \equiv I_{12}/I_{dc}$ and $R_{22} \equiv I_{22}/I_{dc}$ are calculated from these results.

The ratios R_{11}, R_{21}, $R_{12}$and R_{22} are related to the retardance μ, orientation angle χ of the retardation, attenuation ν and the orientation angle of the attenuation Ψ of the sample by

$$R_{11} = 2J_{11}(A)\sin 2(\Psi)\nu \tag{2.1}$$

$$R_{21} = 2J_{21}(A)\cos 2\Psi\nu \tag{2.2}$$

$$R_{12} = -2J_{12}(A)\cos 2\chi \sin\mu \tag{2.3}$$

$$R_{22} = 2J_{22}(A)\sin 2\chi \sin\mu \tag{2.4}$$

for a sample with $\Psi = \chi$ and $\nu \ll \mu$. $J_{11}(A)$ and $J_{12}(A)$ are Bessel functions of the first kind, and $J_{21}(A)$ and $J_{22}(A)$ are Bessel functions of the second kind, all evaluated at the amplitude of the modulator [21]. In practice the 'J-values' are treated

as calibration constants, measured using a polarizer as a sample. These expressions allow us to calculate μ, ν, χ and Ψ. We calculate birefringence ($\Delta n'$) and dichroism ($\Delta n''$) in the plane normal to the optical axis using the relationships

$$\mu = \frac{2\pi d}{\lambda}\Delta n', \tag{2.5}$$

$$\nu = \frac{2\pi d}{\lambda}\Delta n'', \tag{2.6}$$

where d is the optical path length and λ is the wavelength of incident light.

The flow cell geometries (Figure 2.3) are designed for measurements either with the optical beam along (i) the vorticity direction (axis 3) or (ii) the velocity gradient (axis 2). Infrared dichroism measurements are performed only with the optical axis along the velocity gradient, since the optical path length must be kept short ($<$ 1mm) due to attenuation.

2.4 Two-axis Optical Rheometer

In certain rheological problems, it is necessary to simultaneously observe two orthogonal projections of the optical properties to gain a complete understanding of the physics. To do this, we have constructed an apparatus to monitor the complete refractive index tensor (real part) during dynamic mechanical testing. Two identical, orthogonal optical trains for measuring birefringence are built around an RSAII (Figure 2.2). It should be noted that two axes at arbitrary angle could be used, as described by Brown and Burghardt [22]. Instead of photo-elastic modulation used in

the single-axis optical rheometer, electro-optic (EO) modulation is chosen because it can be operated in a mode that simplifies signal analysis and provides higher speed than can be achieved with PEMs. To illustrate the use of the EO modulator, note that if the retardation of this element in the optical train in Figure 2.2 could be increased linearly with time $\delta = at$, the intensity transmitted through the optical train would vary sinusoidally. If the sample is birefringent, but not dichroic, the amplitude of the oscillatory intensity is related simply to the magnitude of the retardation, and the phase of the oscillation with respect to $\sin(at)$ is related directly to the orientation angle of the birefringence, as described below. A linearly increasing retardation is indistinguishable from one that ramps from an initial value δ_o to $\delta_o + 2\pi$, then drops instantly to δ_o, and repeats this saw-tooth indefinitely. For this purpose we use a Stanford Research DS340 function generator to synthesize the saw-tooth function, which is amplified 40 times using a New Focus high-voltage amplifier (HVA 3211) to drive a $LiTaO_3$ EOMs. The protocol for aligning the optical elements as indicated in Figure 3.1b and calibration are described in Appendix A.

2.4.1 Data Acquisition and Analysis

For the case of a sample that is birefringent, but not dichroic, the intensity modulation observed at the end of the optical train is

$$I(t) = I_{dc}[1 + b(\cos\Omega t \sin\mu \sin 2\chi - \sin\Omega t \sin\mu \cos 2\chi)] \tag{2.7}$$

where I_{dc} is the steady component of the intensity, b is a calibration factor. $\mu = (2\pi d/\lambda)\Delta n$ is the retardation of the sample with optical path length d and birefringence Δn, λ is the wavelength of light, χ is the orientation angle of the birefringence, and Ω is the modulation frequency.

In the case of the two-axis optical rheometer, the design of the flow cell (Figure 2.3) allows for measurements either with the optical beam along (i) the vorticity direction (axis 3) or (ii) the velocity gradient (axis 2), or (iii) along both of these axes simultaneously.

Both the magnitude and orientation of the birefringence in the 1,2-plane are unknown, which requires determination of both the $\sin\Omega t$ and $\cos\Omega t$ components of the modulated intensity $I(t)$ observed with the beam along the vorticity axis. The intensity of these two components, when normalized by I_{dc} and the appropriate calibration factor b, are given by

$$X_{12} = \sin\mu_{12}\cos 2\chi_{12}, \tag{2.8}$$

and

$$Y_{12} = \sin\mu_{12}\sin 2\chi_{12}, \tag{2.9}$$

where the symbols are as defined above and the subscript 12 designates values observed in the 1,2-plane of the flow.

The birefringence in the 1,3-plane (observed by the beam propagating along the velocity gradient direction) is oriented along the flow direction by symmetry. The magnitude of the 1,3-birefringence is determined from the intensity of the $\sin\Omega t$ component X_{13} of the observed signal $I(t)$, normalized by I_{dc} and by the calibration factor

b,

$$X_{13} = \sin \mu_{13}, \tag{2.10}$$

where the subscript 13 designates values observed in the 1,3-plane of the flow. Given the symmetry of the shear flow, these three observables (X_{12}, Y_{12} and X_{13}) are sufficient to characterize the real part of the deviatoric refractive index tensor when the retardation does not exceed the first order, i.e., $-\pi/2 < \mu < \pi/2$.

These instruments provide quantitative information regarding the microrheology of complex polymer melts. In the next two chapters, we illustrate how direct comparison of dynamic birefringence, dichroism and stress can reveal molecular and microstructural dynamics that underlie the flow behavior of melts using examples from our research on homopolymer melts [23], miscible polymer blends [24], block copolymers (BCPs) [9], and side-group liquid crystalline polymers (SG-LCPs) [3, 25]. Normal stress measurements on homopolymer melts requires quantitative measurements of stress and birefringence at small strains. In chapter 3, we demonstrate the sensitivity of the method by quantitative measurements of flow birefringence at small strains, to study normal stresses in homopolymer melts through the use of stress-optical rule. In blends, SG-LCPs and BCPs, it is necessary that we distinguish between the various contributions to the viscoelasticity of the fluid: each species gives a distinct contribution to the viscoelasticity of a miscible blend; macromolecules, microphase structures and defects combine to give rise to the flow behavior of ordered block copolymers; and the flexible backbone, director field and disclinations are all involved in the rheology of side-group liquid crystals. In chapter 4, we will use the

failure of the stress-optical rule to isolate molecular and microstructural contributions in SG-LCPs, diblock copolymers and blends. In chapters 6 and 7, we will use the apparatus to study the mechanisms of flow-alignment in SG-LCPs and BCPs.

Bibliography

[1] Koppi, K. A.; Tirrell, M; Bates, F. S; Almdal, K; Colby, R. H., *J. Physique II*, **1992**, 2 (11), 1941.

[2] Morrison, F. A.; Winter, H. H; Gronski, W; Barnes, J. D., *Macromolecules*, **1990**, 23 (19), 4200.

[3] Kannan, R. M.; Kornfield, J. A; Schwenk, N. Boeffel, C., *Macromolecules*, **1993**, 26, 2050-2056.

[4] Fuller, G. G., *Ann. Rev. Fluid Mech.*, **1990**, 22, 387.

[5] Janeschitz-Kriegl, H., *Polymer Melt Rheology and Flow Birefringence*, **1983** Springer-Verlag, New York.

[6] Osaki, K.; Takatori, E.; Ueda, M.; Kurata, M.; Kotaka, T., *Macromolecules*, **1989**, 22 (5), 2457.

[7] Inoue, T.; Okamoto, H.; Osaki, K., *Macromolecules*, **1991**, 24 (20), 5670.

[8] Hongladarom, K.; Burghardt, W. R.; Baek, S. G.; Cementwala, S.; Magda, J. J., *Macromolecules*, **1993**, 26, 772.

[9] Kannan, R. M.; Kornfield, J. A., *Macromolecules*, **1994**, 27, 1177.

[10] Tassin, J. F.; Monnerie, L.; Fetters, L. J., *Macromolecules*, **1988**, 21 (8), 2404.

[11] Kornfield, J. A.; Fuller, G. G.; Pearson, D. S., *Macromolecules*, **1989**, 22 (3), 1334.

[12] Zawada, J. A.; Ylitalo, C. M.; Fuller, G. G.; Colby, R. H.; Long, T. E., *Macromolecules*, **1992**, 25 (11), 2896.

[13] Archer, L. A.; Fuller, G. G.; Nunnelley, L., *Polymer*, **1992**, 33 (17), 3574.

[14] Viovy, J. L.;Monnerie, L; Merola, F., *Macromolecules*, **1985**, 18 (6), 1130.

[15] van Egmond, J. W.; Werner, D. E.; Fuller, G. G., *J. Chem. Phys.*, **1992**, 96 (10), 7742.

[16] Dhaene, P.; Mewis, J.; Fuller, G. G.; *J. Colloid Sci.*, **1993**, 156 (2), 350.

[17] Koppi, K. A., M. Tirrell and F. S. Bates, "Shear-Induced Isotropic-to-Lamellar Transition", Phys. Rev. Lett. **70**, 1449-1452 (1993).

[18] Horn, R. G.; Kleman, M., *Ann. Phys.*, **1978**, 3, 229.

[19] Mather, P. T.; Pearson, D. S., *ACS Meeting Abstracts*, **1992**, 203, 584.

[20] Mead, D. W.; Larson, R. G., *Macromolecules*, **1990**, 23 (9), 2524.

[21] Johnson, S. J.; Frattini, P. L.; Fuller, G. G., *J. Colloid Sci.*, **1985**, 104 (2), 440.

[22] Brown, E. F.; Burghardt, W. R., *Proc. ACS Div. PMSE*, **1993**, 69, 349.

[23] Kannan, R. M.;Kornfield, J. A., *Rheol. Acta*, **1992**, 31 (6), 535.

[24] Arendt, B. H.; Kannan, R. M.; Zewail, M.; Kornfield, J. A.; Smith, S., "Dynamics of Each Species in Miscible Polymer Blends of Polyisoprene and Polyvinylethylene", *Rheol. Acta*, accepted in March 1994.

[25] Kannan, R. M.; Kornfield, J. A.; Schwenk, N.; Boeffel, C., *Adv. Mat.* , **1994**, 6 (3), 214.

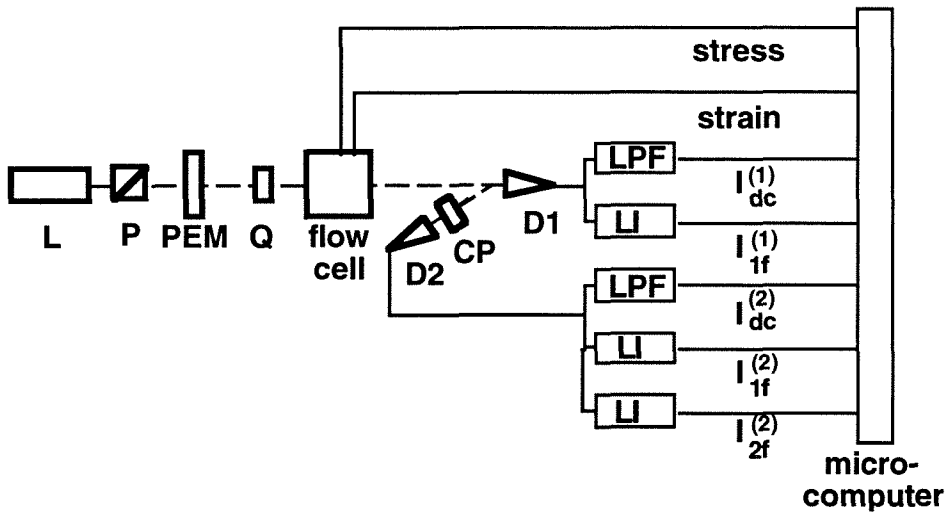

Figure 2.1: Apparatus for simultaneous measurement of birefringence, dichroism, strain and stress (Single axis rheometer). The source includes both a HeNe laser and an infrared diode laser ($\lambda = 4.53\mu$m).The optical train consists of a polarizer (**P**) oriented at 0° (along the flow direction), an electro-optic modulator (**EOM**) oriented at 45°, a quarter wave plate **Q** at 0°, the sample (polymer in a flow cell described below), a beam splitter which transmits nearly 95% of the light to D1 (the dichroism dectector), and reflects the rest through a circular polarizer **CP** consisting of a quarter wave plate oriented at 45° and a polarizer oriented at 90°, to D2 (the birefringence detector.

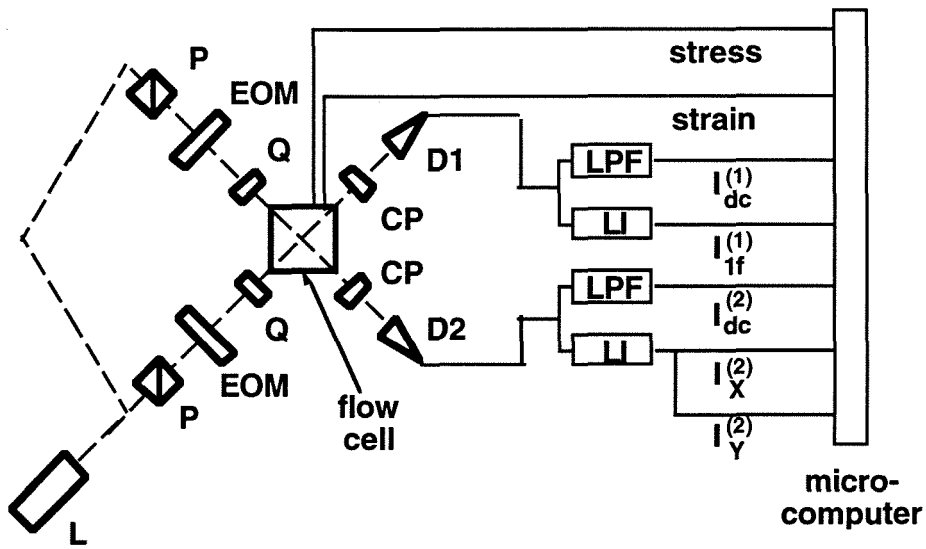

Figure 2.2: Instrument for simultaneous measurement of birefringence along two axes, strain and stress (Two-axis rheometer). The optical train for measuring birefringence is the same as the one described in Figure 2.1. The X-component of the modulated intensity of the 1,3-detector is determined using a single phase lock-in amplifier (Stanford Research SR510). The intensity observed by the optical train aligned along the vorticity axis is analyzed using a Stanford Research SR850 dual-phase lock-in amplifier with its phase adjusted as described in Appendix A.

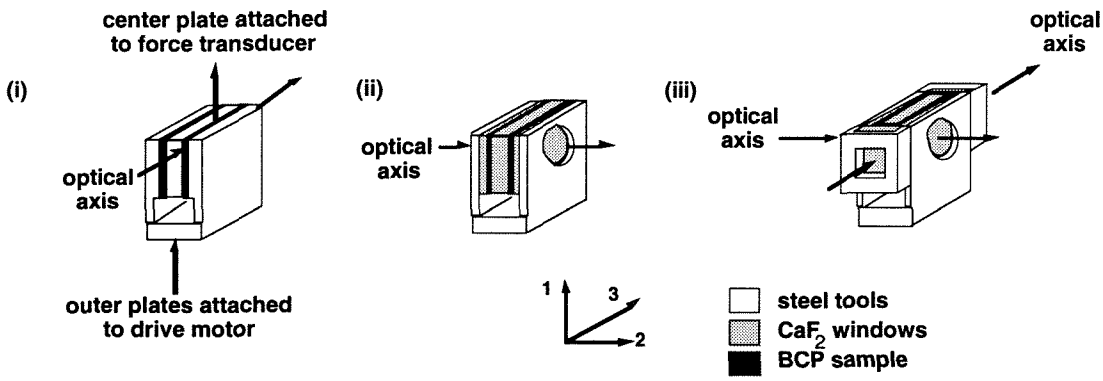

Figure 2.3: Shear sandwich flow cells used for dynamic and step shear experiments. In the single axis instrument, two different flow cells are used, depending on the orientation of the optical axis: the one on the left (i) is used when the optical axis coincides with the vorticity direction, the one in the middle (ii) is used when it coincides with the velocity gradient direction. In the dual axis instrument, the design on the right (iii) is used, so that these two axes can be probed simultaneously.

Chapter 3

Third Normal Stress in Homopolymer Melts

3.1 Introduction

Fluids that exhibit normal stresses display dramatically different flow phenomena from Newtonian fluids [1]. Some of the familiar examples are the tubeless siphon effect, rod-climbing and die swell observed in the flow of concentrated polymer solutions. Further, normal stresses play a critical role in controlling flow stability and dictating the type of secondary flows that may develop. Many examples of both academic and practical interest are known, including elastically-driven instability in Couette flow [2] and secondary flows upon passage through contractions and around objects. Dynamics of bubbles, droplets and particles in polymeric liquids are dramatically influenced by normal stresses, producing qualitatively different droplet shapes and particle distributions than those observed in Newtonian fluids [1].

Quantitative prediction of these phenomena requires knowledge of the constitutive relation that describes the stress as a function of deformation history for a given polymeric liquid [1, 3]. Constitutive equations must accurately describe the normal stress differences in order to correctly capture the variety of flow phenomena that arise from them. To test the validity of constitutive equations and guide the choice of their parameters, it is necessary to measure the normal stress differences.

In a shear flow with velocity along direction "1", velocity gradient along "2" and vorticity along "3", the stress tensor $\underline{\underline{\sigma}}$ may be characterized by the shear stress σ_{12}, the primary normal stress difference $N_1 = \sigma_{11} - \sigma_{22}$, the secondary normal stress difference $N_2 = \sigma_{22} - \sigma_{33}$, and the isotropic pressure p. Mechanical [4] and optical [5] methods to measure σ_{12} and N_1 are well established. However, complete

characterization of $\underline{\underline{\sigma}}$ also requires measurement of N_2 or, alternatively, $N_3 = N_1 + N_2$, and this has been more difficult [6, 7]. For solutions and melts of flexible polymers, N_1 is found to be positive and the limited observations of N_2 show it to be negative with a magnitude that is small compared to N_1 ($\lesssim 25\%$) [6, 7, 8, 9, 10, 11]. Therefore N_1 usually plays the dominant role in producing distinctive phenomena in shear flows. However, when accurate predictions are required or when the flow geometry eliminates the effects of N_1, the secondary normal stress difference plays an important role.

This study investigates the dynamic response of the third normal stress difference, which is the sum of the first and second normal stress differences $N_3 \equiv N_1 + N_2$, in small amplitude oscillatory shear. Over a range of small but finite strains, the frequency dependence of N_3 is expected to be related to that of the shear stress *if* both are governed by the linear viscoelastic memory function of the polymeric liquid. However, the resulting relationship does not predict the magnitude of N_3. Molecular models, such as the non-preaveraged, hydrodynamically-interacting bead-spring and bead-rod models of flexible chains in solution, and the reptation model of entangled melts, offer quantitative predictions of N_3 [1, 3]. Here we focus on nearly monodisperse, entangled polymer melts to see if the behavior of N_3 is universal, and to compare it to the predictions of the reptation model [12].

There is a dearth of experimental observations of the full stress tensor in transient shear, particularly for concentrated solutions and melts. Gao et al. [6] used measurements of the torque and radial distribution of the normal force in a cone and plate device to determine the full stress tensor in a series of concentrated polymer solu-

tions subject to oscillatory shear. Also, Meissner et al. [11] developed an alternative approach based on measurements of the torque and the thrust force distribution in a cone and plate device, and characterized the full stress tensor in a polymer melt during the inception of steady shear flow. Kimura et al. [10] have performed step-strain relaxation experiments using mechanical measurements of the shear stress, together with birefringence measurements in both the 1,2- and 1,3-planes to determine the full stress tensor. Vinogradov and co-workers [13] used birefringence measurements in the 1,2-plane of a polymer melt in oscillatory shear to determine the displacement of N_1. Kornfield et al. [14] measured oscillatory flow birefringence in the 1,3-plane to determine the frequency dependence of N_3, but not its magnitude.

The basis for stress-optical measurements is the observation that homopolymer melts and solutions obey the stress-optic rule over a wide range of flow conditions [5]. This rule states that the deviatoric parts of the stress and refractive index tensors are proportional to each other: to within an isotropic term $\underline{\underline{\sigma}} = \frac{1}{C}\underline{\underline{n}}$, where C is the stress-optic coefficient. In the case of shear flow, this leads to

$$\sigma_{12} = \frac{1}{2C}\Delta n'_{12}\sin(2\chi), \tag{3.1}$$

$$N_1 = \frac{1}{C}\Delta n'_{12}\cos(2\chi), \tag{3.2}$$

$$N_3 = \frac{1}{C}\Delta n'_{13}, \tag{3.3}$$

where $\Delta n'_{12}$, χ, and $\Delta n'_{13}$ are, respectively, the magnitude of the birefringence in the 1,2-plane (Figure 3.1c), the orientation angle of the birefringence in the 1,2-plane with

respect to the flow direction, and the birefringence in the 1,3-plane. The value of C can be calculated using Eq. (1) provided the values of σ_{12}, $\Delta n'_{12}$ and χ are all known. Given C, one can determine N_1 and N_3 from $\Delta n'_{12}$, χ and $\Delta n'_{13}$ using Eqs. (2) and (3).

There is particular interest in determining the complete stress tensor in small amplitude oscillatory shear to verify relationships between the material functions that describe the normal stresses and the shear stress, which have been recognized for decades, but hardly tested [1, 16]. To confirm these relationships it is necessary to measure normal stresses with sufficient sensitivity to observe them in the small strain limit. It is also desirable to perform the measurements rapidly so that a wide dynamic range can be studied. In these respects, previous work has been limited to relatively large strain amplitudes ($\gtrsim 40\%$) and modest dynamic range (1–3 decades).

Our strategy for achieving the required sensitivity is to use the single-axis optical rheometer described in Chapter 3, in both 1,2 and 1,3 geometries to measure the third normal stress difference under oscillatory shear at small strains. This also serves to demonstrate the sensitivity and the dynamic range of our apparatus, and its capacity to perform over a wide-range of temperatures and frequency.

The following section describes the expected behavior of the complete stress tensor in small-amplitude oscillatory shear, and reviews the experimental results available to verify these predictions. Section 3 describes the experimental details specific to the results discussed in this chapter. Section 4 presents the results of stress-optical characterization of three linear polymer melts. The final section discusses these results,

our conclusions, and directions for future work.

3.2 Material Functions for Oscillatory Shear

When a polymeric liquid is subjected to small-amplitude oscillatory shear at frequency ω, the shear stress also oscillates with frequency ω, but out of phase with the strain, and the normal stress differences oscillate with frequency 2ω about a nonzero mean value. The amplitude and phase of the shear stress are characterized using the complex viscosity η^* or, equivalently, the dynamic modulus $G^* \equiv G' + iG'' = i\omega\eta^*$ [4]. The amplitude and phase of the first and second normal stress differences are characterized by the complex normal stress coefficients $\psi_j^* = \psi_j' - i\psi_j''$ for $j = 1, 2$. In addition, the mean values of these normal stress differences are described by displacement coefficients ψ_j^d for $j = 1, 2$ [4]. For sinusoidal shear $\gamma(t) = \gamma_o \sin\omega t$ in the coordinate system of Figure 3.1, the shear stress and normal stress differences are expressed in terms of these eight material functions as

$$\sigma_{12} = \gamma_o[G'\sin\omega t + G''\cos\omega t] \tag{3.4}$$

$$\sigma_{11} - \sigma_{22} = (\gamma_o)^2[\omega^2\psi_1^d + \omega^2\psi_1''\sin 2\omega t + \omega^2\psi_1'\cos 2\omega t], \tag{3.5}$$

$$\sigma_{22} - \sigma_{33} = (\gamma_o)^2[\omega^2\psi_2^d + \omega^2\psi_2''\sin 2\omega t + \omega^2\psi_2'\cos 2\omega t]. \tag{3.6}$$

In the limit of small enough strains or slow enough strain rates, flows perturb the fluid only slightly from equilibrium, it is reasonable to hypothesize that a constitutive

equation depend on a single memory function, and require that it recover the linear behavior as strain (or strain rate) vanishes, and satisfy frame invariance. A simple, single-integral constitutive equation that fulfills these criteria is

$$\underline{\underline{\sigma}} = \int_{-\infty}^{t} M(t-t') \left[(1-\beta)\cdot\underline{\underline{C}}^{-1}(t,t') - \beta\cdot\underline{\underline{C}}(t,t')\right] dt', \tag{3.7}$$

where $M(t)$ is the memory function of linear viscoelasticity, $\underline{\underline{C}}^{-1}$ is the Finger tensor, $\underline{\underline{C}}$ is the Cauchy tensor[3], and β is a parameter between 0 and 1. In general, the two requirements that we impose could be satisfied even if different memory functions are applied to the Finger tensor and Cauchy tensor terms. Therefore the predictions of Eq. (3.7), particularly regarding the dynamic response of the second normal stress difference, can be used to determine whether or not a single memory function is, in fact, sufficient for some polymeric liquids near the linear regime.

Applied to the case of small amplitude oscillatory shear, Eq. (3.7) leads to the following relationships between the material functions:

$$-\omega^2\psi_1'(\omega) = G'(\omega) - \frac{1}{2}G'(2\omega), \tag{3.8}$$

$$\omega^2\psi_1''(\omega) = G''(\omega) - \frac{1}{2}G''(2\omega), \tag{3.9}$$

$$\omega^2\psi_1^d(\omega) = G'(\omega), \tag{3.10}$$

$$\psi_2^*(\omega) = -\beta\cdot\psi_1^*(\omega), \tag{3.11}$$

$$\text{and}\quad \psi_2^d(\omega) = -\beta\cdot\psi_1^d(\omega). \tag{3.12}$$

Indeed, a variety of constitutive equations do lead to Eqs. (3.8–3.12) (Spriggs et al. 1966), although most have $\beta = 0$. If these relations, particularly Eqs. (3.11–3.12), are found to hold for entangled polymers then we can infer that a single memory function governs the complete stress response in the limit of sufficiently small or sufficiently slow deformations.

Very few observations are available to test these relations. Gao et al. [6] measured N_1 and N_2 in a variety of polybutadiene solutions during oscillatory shear. Although their results for N_2 were limited to slighly more than one decade of dynamic range, they did support the validity of Eqs. (3.8–3.12), with $\beta \approx 0.22$ based on $-N_2/N_1$.

Experimental results regarding the applicability of Eqs. (3.8–3.12) to polymer melts have come primarily from two dynamic birefringence studies. Quantitative stress-optical measurement of the displacement component N_1 in oscillatory shear has verified Eq. (3.10) for polyisoprenes and polybutadienes with varying molecular weight and molecular weight distribution [13]. More recent measurement of the frequency dependence of the complex amplitude and displacement of N_3 in a series of entangled poly(ethylene-propylene) melts confirm the form of Eqs. (3.11) and (3.12) [14]. However, quantitative measurements of 1,3-birefringence in oscillatory shear have not been made, so determination of β has not been possible.

A number of molecular models predict nonzero values of β for polymer solutions and melts. In particular, for entangled melts in the plateau and terminal regime, β should have a universal value independent of the chemical structure of the polymer [12]. Two different values have been predicted by the Doi-Edwards (DE) model:

analysis invoking the independent-alignment approximation (IAA) [17] leads to $\beta = 2/7$, whereas analysis that avoids this approximation [7] produces $\beta = 1/7$. Few results are available to test these predictions regarding the value of β. The most appropriate experiments for comparison to the DE model are those of Osaki et al. [7] who performed stress-optical measurements of N_1 and N_3 in an entangled, nearly monodisperse polystyrene solution during relaxation following a step shear strain. They studied the strain dependence of $-N_2/N_1$ for γ_o from 0.6 to 2. For strains below 100% this ratio was nearly independent of strain and time, giving $\beta \approx 0.19$, close to the value predicted without IAA.

To improve our understanding of the complete stress response of entangled polymers to transient shear, it is important to test the validity of Eqs. (3.8–3.12) and, if they hold, to determine the value of β for various narrow distribution polymer melts.

Here we report quantitative stress-optical measurements of N_3 for three entangled melts over four to five decades of reduced frequency. These are compared with the expected relationships of its complex amplitude and displacement to the dynamic modulus. This comparison supports the validity of the relations between the material functions and is used to infer the value of β for poly(ethylene-propylene) and polyisoprene.

3.3 Experimental Section

3.3.1 Single-axis Optical Rheometer

We use the single-axis optical rheometer (described in Chapter 2), to measure only the birefringence, using the optical train shown in Figure 3.2. Rheo-optical measurements were performed both with the optical axis along the neutral direction and with the optical axis along the velocity gradient (Figure 3.1, *right*) using shear sandwich fixtures. The first of these probed the birefringence in the 1,2-plane (Figure 3.1, *left*). In this geometry, the standard shear sandwich tool was used (optical path length = 16 mm). Measurements of 1,2-birefringence were repeated with and without windows placed on the fixture, and with gap widths of 0.5 mm and 1 mm. The area of the shear-sandwich fixture used for this work is 4 cm^2. Birefringence in the 1,3-plane was measured with the optical axis along the velocity gradient. For this geometry, custom shear sandwich fixtures were fabricated with the plates replaced by CaF_2 windows (Figure 3.1c, *right*). The optical path in this case was twice the gap width, *i.e.*, 1 mm or 2 mm.

3.3.2 Data Acquisition and Analysis

The signals from the displacement and force transducers, the low-pass filter and both lock-in amplifiers were recorded by a microcomputer (Macintosh IIci with National Instruments NB-MIO-16XL and NB-DMA8G A/D and DMA boards) at a rate that provided 128 points per cycle of the oscillatory strain at frequency ω. The strain,

stress, $R_{1f} \equiv I_{1f}/I_{dc}$ and $R_{2f} \equiv I_{2f}/I_{dc}$ were calculated from these results. The data acquired over a number of cycles (typically 1–10) were then averaged.

The ratios R_{1f} and R_{2f} are related to the retardance μ and orientation angle χ of the sample by [15]

$$R_{1f} = -2J_1(A)\cos 2\chi \sin \mu, \tag{3.13}$$

$$R_{2f} = 2J_2(A)\sin 2\chi \sin \mu, \tag{3.14}$$

for a sample with zero dichroism, where $J_1(A)$ and $J_2(A)$ are Bessel functions of the first kind evaluated at the amplitude of the modulator and $\mu = \frac{2\pi d}{\lambda}\Delta n'$, with d the optical path length, λ the wavelength of the incident light, and $\Delta n'$ the birefringence in the plane normal to the optical axis. In practice the 'J-values' $J_1(A)$ and $J_2(A)$ are treated as calibration constants, measured using a polarizer as a sample, for which $R_{1f} = 2J_1(A)\sin(2\chi)$ and $R_{2f} = 2J_2(A)\cos(2\chi)$. The values of $2J_1$ and $2J_2$ are the extrema of R_{1f} and R_{2f} as the polarizer is rotated. The ratios R_{1f} and R_{2f} recorded during an experiment are divided by $-2J_1$ and $2J_2$, respectively. From these we calculate $\Delta n' \sin 2\chi$ and $\Delta n' \cos 2\chi$. For a material obeying the stress-optic rule, these quantities equal $2C\sigma_{12}$ and CN_1 for birefringence in the 1,2-plane, and equal 0 and CN_3 for birefringence in the 1,3-plane.

Next, the Fourier transforms of the time-domain signals are calculated. The fundamental component of the strain, stress and $\Delta n'_{12}\sin 2\chi$ are used to calculate the dynamic modulus G^* and $2CG^*_{so}$, where the subscript denotes the stress-optically determined dynamic modulus. The mean value and second harmonic components of $\Delta n'_{13}\cos 2\chi$ are used to determine $C\omega^2\psi_3^d$ and $C\omega^2\psi_3^*$, where these implicitly denote

the stress-optically determined material functions.

3.3.3 Materials and Methods

Two narrow molecular-weight distribution (MWD), entangled polymer melts were used in this study: poly(ethylene-propylene) (PEP) M_w = 87 kg/mol and polyisoprene (PI-143) M_w = 143 kg/mol. For comparison, a polydisperse polyisoprene (PI-170) M_w = 170 kg/mol was also characterized. PEP was provided by Frank Bates; its characterization has been reported previously [18]. The polyisoprenes were synthesized in our laboratory using anionic polymerization. Their molecular weights were determined by size-exclusion chromatography based on calibration using polyisoprene standards. Both the size-exclusion chromatography traces and the dynamic moduli show PI-143 has a slightly broader MWD than PEP, and PI-170 has a substantially broadened MWD, indicative of impurities present during polymerization. The polydispersity indices (M_w/M_n) for PI-143 and PI-170 were estimated from the SEC traces to be 1.09 and 1.75, respectively.

Oscillatory strain of 0.5 to 2% was applied for measurements of dynamic birefringence in the 1,2-plane, with the upper limit of γ_o chosen so that magnitude of μ remained less than $\pi/2$. For the current flow cell (with d = 16 mm) this corresponded to strains from ~0.5% at high frequencies (ca. 100 rad/s) to ~2% at low frequencies (ca. 0.1 rad/s). At these small strains we did not obtain satisfactory results for $\Delta n'_{12} \cos 2\chi$, probably because $|\chi|$ was very close to 45°. Measurements of 1,3-birefringence were made using strain amplitudes ranging from 5% at high frequency

to 15% at low frequency.

Experiments were performed at 22, 45 and 80°C for PEP, at 22 and 45°C for PI-143, and at 22, 45, 80 and 110°C for PI-170. Characterization of the polyisoprenes was performed in a nitrogen-purged environment. At each temperature the frequency ranged from 100 rad/s down to between 0.1 and 0.01 rad/s. The material functions measured at different temperatures were superimposed by shifting along the frequency axis alone [19]. The frequency shift factors with respect to a reference temperature of 22°C are given in the table 3.1. The shift factors observed for PEP are in good agreement with previous studies [19]; those for PI agree reasonably well with those for hevea rubber [4], but differ somewhat from those reported by Gotro and Graessley [19].

3.4 Results

The frequency dependence of the dynamic moduli of PEP and PI-143 is characteristic of narrow distribution, entangled polymers (Figure 3.3a, b). For narrow distribution entangled polymers the product of the plateau modulus and the recoverable compliance, $G_N^o J_e^o \approx 2$, indicating a sharp terminal relaxation [19]. For the PEP sample $G_N^o J_e^o = 2.1$ and for the PI-143 sample $G_N^o J_e^o \approx 3$. The magnitude of the peak in the loss modulus G_m'' is 2.57×10^6 dyn/cm^2 for PEP and 9.64×10^5 dyn/cm^2 for PI-143. These values are in good agreement with previous results on narrow distribution PEPs and PIs [19]. The dynamic modulus of PI-170 reveals a much broader distribution of relaxation times, characteristic of greater polydispersity relative to PEP and PI-143.

The average value of $\frac{|2CG^*_{so}|}{2|G^*|}$ at each temperature was taken as the stress optical coefficient (C in the table 3.1). The value of C for PI at 22°C agrees with that reported by Vinogradov et al. [13] at room temperature. The dynamic moduli calculated from the birefringence (G^*_{so}) using these values of the SOC are in excellent agreement with the mechanically measured dynamic moduli, confirming the applicability of the stress-optic rule (Figure 3.3). For PI we have sufficient results to compare the temperature dependence of C to one linear in reciprocal temperature as suggested by the Kuhn-Grün theory [5, 20]. Indeed, our limited data on PI are described by $C \times 10^{10}$ $(\mathrm{cm}^2/\mathrm{dyn}) = 0.605 + \frac{389.2}{T}$, where T is absolute temperature (K).

The optically-determined complex amplitude of the third normal stress difference (Figure 3.4) varies more strongly with frequency than does the dynamic modulus [14]. In particular, its real part $\omega^2\psi'_3$ changes sign on the low frequency side of the cross-over point, and its imaginary part $\omega^2\psi''_3$ drops off more sharply below the cross-over than does G''. According to Eqs. (3.8), (3.9) and (3.11), $\omega^2\psi^*_3 = (1-\beta)\omega^2\psi^*_{1,cal}$, where $\omega^2\psi^*_{1,cal}$ denotes the complex amplitude of N_1 calculated from the measured dynamic moduli using the right-hand sides of Eqs. (3.8) and (3.9). Therefore the average value of $\frac{|\omega^2\psi^*_3|}{|\omega^2\psi^*_{1,cal}|}$ for each sample is taken as the value of $(1-\beta)$. We find $(1-\beta) = 0.69\pm0.07$ for PEP, 0.77 ± 0.08 for PI-143, and 0.75 ± 0.07 for PI-170. The optically measured values of $\omega^2\psi^*_3$ are compared to $\omega^2\psi^*_{3,cal} = (1-\beta)\omega^2\psi^*_{1,cal}$ in Figure 3.4. The agreement is very good for all three polymers at all temperatures.

On the basis of Eqs. (3.10) and (3.12), the displacement component of N_3 is expected to be $\omega^2\psi^d_3 = (1-\beta)G'$. The two are compared in Figure 3.5, showing

reasonable agreement for all polymers and temperatures. The discrepancy between the optically measured values and the ones calculated from the storage modulus may be due to baseline drift in the optical measurement, which effects the determination of the displacement component.

3.5 Discussion and Conclusion

We have developed an apparatus that has sufficient sensitivity to measure the third normal stress difference for polymer melts over a wide range of reduced frequency at small strains ($\leq$15%). This represents a substantial improvement over the previous methods in terms of both sensitivity and dynamic range.

Results have been presented for experiments at temperatures from 22 to 100°C, and confirm that time-temperature superposition holds for all five of the material functions reported. We have obtained results covering 4 to 5.5 decades of reduced frequency. The stress-optic coefficients for PEP and PI are found to decrease monotonically with increasing temperature. Further, the values of $C(T)$ for PI vary linearly with reciprocal temperature in accord with the theory of Kuhn and Grün [5, 20].

The results for the stress optically measured complex amplitude of N_3, $\omega^2\psi_3^*$, agree quantitatively with the relationships to the dynamic moduli given in Eqs. (3.8–3.12). Establishing these relationships is valuable technologically and scientifically. In processing applications where on-line viscoelastic measurements are desired, these relationships provide the basis for characterization using dynamic 1,3-birefringence measurements, which can be made with a device that is simpler and potentially less

expensive than a dynamic mechanical rheometer. Further, $\omega^2\psi_3^*$ provides a sharper signature of the terminal relaxation and polydispersity of the sample than do the dynamic moduli. This method would be applicable to amorphous, transparent polymer melts and solutions that obey the stress-optic rule. The optically measured $\omega^2\psi_3^*$ can be used to estimate the dynamic moduli based on Eqs. (3.8), (3.9) and (3.11) with $(1-\beta) = 0.74 \pm 0.07$ for entangled, linear polymers.

The scientific significance of the success of these interrelations is that it indicates that a single memory function governs the dynamic response of all components of the stress tensor when deformations are sufficiently small or slow. This narrows the range of admissable constitutive equations for entangled solutions and melts. In addition, the established behavior of the dynamic 1,3-birefringence of amorphous polymer melts can be used as a point of departure for comparison with stress-optically complex systems, such as liquid crystalline polymers and ordered block copolymers. Valuable information regarding these more complex fluids can be gained by noticing the particular way the dynamic birefringence deviates from that anticipated based on Eqs. (3.8–3.12) and the measured dynamic moduli[21]

The challenge of determining β in Eq. (3.7) remains. The values that we infer for β are 0.31, 0.25 and 0.23 ± 0.07 for PEP, PI-143 and PI-170, respectively. These values are reasonably close to one another, and to the previous results for entangled polymers in steady shear [22] They are all somewhat higher than that found by [7] ($\beta = 0.19$), which may suggest a slight increase in the ratio $-N_2/N_1$ as strain is decreased from the lowest strain they used (60%) to the highest we used (15%). Based on the

present results, β for various polymers is constant to within the uncertainty of the measurements, with $\beta = 0.26 \pm 0.07$. Our results are closer to the reptation result *with* IAA (0.28) than that without IAA (0.14), however the latter is not far outside the range of uncertainty in our values. Further, it is not possible for us to determine whether the variation is significant among the values we obtained for PEP (0.31) and PI (0.24) and that found by Osaki et al. [7] ($\beta = 0.19$). To obtain stronger evidence regarding the existence of a universal value of β for all entangled polymers, one must more precisely determine its value and do so for a greater variety of materials.

Bibliography

[1] Bird, R. B.; Armstrong, R. C.; Hassager, O., "Dynamics of Polymeric Liquids, v. 1: Fluid Mechanics," Wiley & Sons (1987).

[2] Muller, S. J.; Larson, R. G; Shaqfeh, E. S. G., *Rheol Acta.*, **1989**, 28, 499; Larson, R. G.; Shaqfeh, E. S. G.; Muller, S. J., *J. Fluid Mech.*, **1990**, 218, 573.

[3] Larson, R. G., "Constitutive Equations for Polymer Melts and Solutions," Butterworths, **1988**.

[4] Ferry, J. D., "Viscoelastic Properties of Polymers," 3rd ed. Wiley, New York **1980**.

[5] Janeschitz-Kriegl, H., "Polymer Melt Rheology and Flow Birefringence," Springer, New York **1983**.

[6] Gao, H. W.; Ramachandran, S.; Christiansen, E. B., *J. Rheol.* , **1981**, 25, 213.

[7] Osaki, K.; Kimura, S.; Kurata, M., *J. Poly Sci:Poly Phys Ed.*, **1981**, 19, 517.

[8] Kuo, Y.; Tanner, R. I., *Rheol. Acta*, **1974**, 13, 443.

[9] Alvarez, G. A.; Lodge, A. S.; Cantow, H-J.; *Rheol. Acta*, **1985**, 24, 368.

[10] Kimura, S.; Osaki, K.; Kurata, M., *J. Poly. Sci:Poly Phys Ed.*, **1981**,19, 151.

[11] Meissner, J.; Garbella, R. W.; Hostettler, J., *J. Rheol.*, **1989**, 33, 843.

[12] Doi, M. and S. F. Edwards, "The Theory of Polymer Dynamics," Clarendon Press, Oxford **1988**.

[13] Vinogradov, G. V.; Isayev, A. I.; Mustafaev, D. A.; Podolsky, Y. Y., *J. App-Poly Sci.*, **1978**, 22, 665.

[14] Kornfield, J. A.; Fuller, G. G.; Pearson, D. S., *Rheol. Acta.*, **1990**, 29, 105.

[15] Johnson, S. J.; Frattini, P. L.; Fuller, G. G., *J. Coll. Int. Sci.*, **1985**,104, 440.

[16] Spriggs, T. W.; Huppler, J,D.; Bird, R. B., *Trans. Soc. Rheo.*, **1966**, 10, 191.

[17] Doi, M.;Edwards, S. F., *J. Chem. Soc. Faraday Trans. II*, **1979**, 75, 38.

[18] Rosedale, J. H.; Bates, F. S., *Macromolecules*, **1990**, 23, 2329.

[19] Gotro, J. T.; Graessley, W. W., *Macromolecules*, **1984**, 17, 2767.

[20] Kuhn, W.; Grün, F., *J. Poly. Sci.*, **1946**, 1, 193.

[21] Kannan, R. M.; Kornfield, J. A.; Schwenk, N.; Boeffel C., *Macromolecules*, **1993**, 26, 2050.

[22] Lee, C-S.; Magda, J. J.; de Vries, K. L.; Mays, J. W., *Macromolecules*, **1992**, 25, 4744.

Table 3.1: Shift factors and stress-optic coefficients of poly(ethylene-propylene) and polyisoprene.

	PEP		PI	
T (°C)	a_T	$C \times 10^{10}$ (cm^2/dyn)	a_T	$C \times 10^{10}$ (cm^2/dyn)
22	1	1.8 7	1	1.9 3
45	0.194	1.7 3	0.125	1.8 2
80	0.0245	1.4 2	0.009	1.7 1
100			0.0034	1.6 5

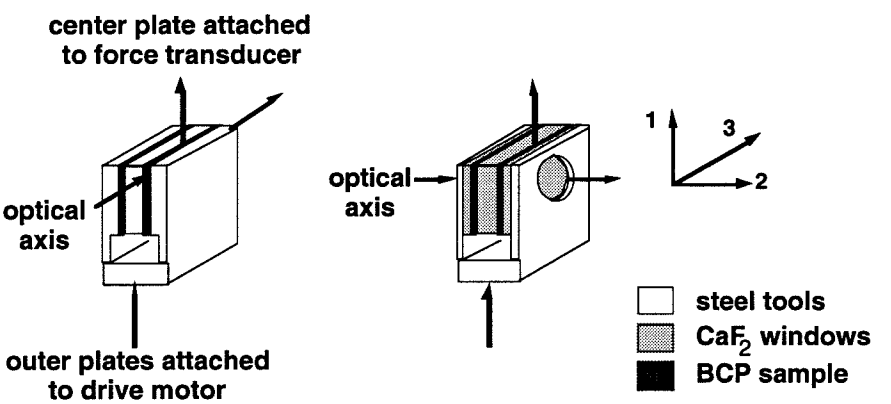

Figure 3.1: Schematic diagram of the flow geometries used to measure birefringence in the 1,2-plane *(left)* and 1,3-plane *(right)*. The shear sandwich flow device is mounted with the outer plates fastened to the motor that drives the shear strain. The center plate is attached to the force transducer.

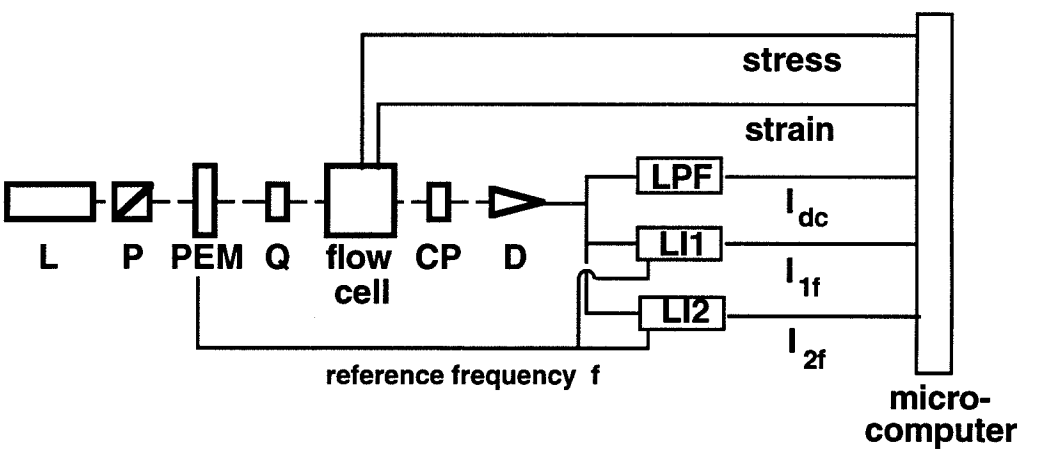

Figure 3.2: Schematic diagram of the apparatus for simultaneous mechanical and optical measurements. Components of the optical train: laser L, linear polarizer P, photoelastic modulator PEM, quarter wave plate Q, shear flow cell of the RSA-II, circular polarizer CP, and detector D. Signal analysis components: low-pass filter LPF, and lock-in amplifiers LI1 and LI2.

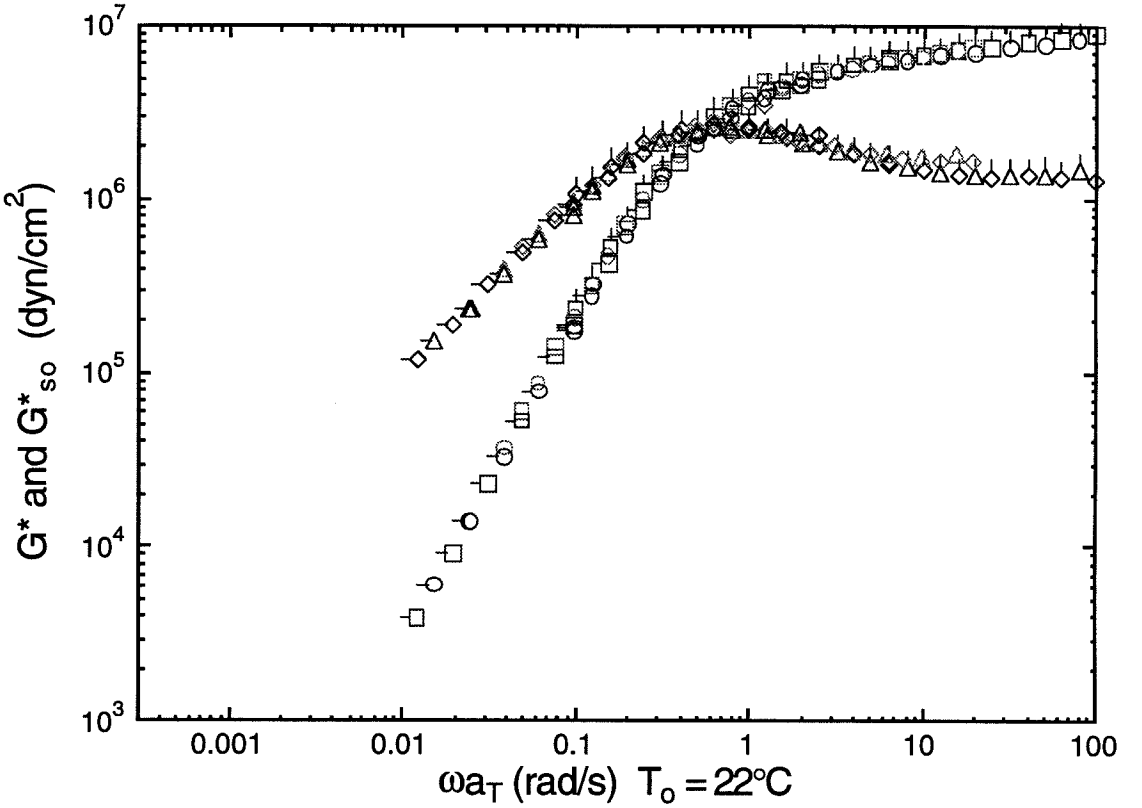

Figure 3.3a: Dynamic moduli determined mechanically (G*) and stress-optically (G^*_{so}) for PEP. G' ∘, G'' ◇, G'_{so} □, G''_{so} Δ. Data at 22°C designated by vertical arm, 45°C by no arm, 80°C by left arm and 100°C by right arm.

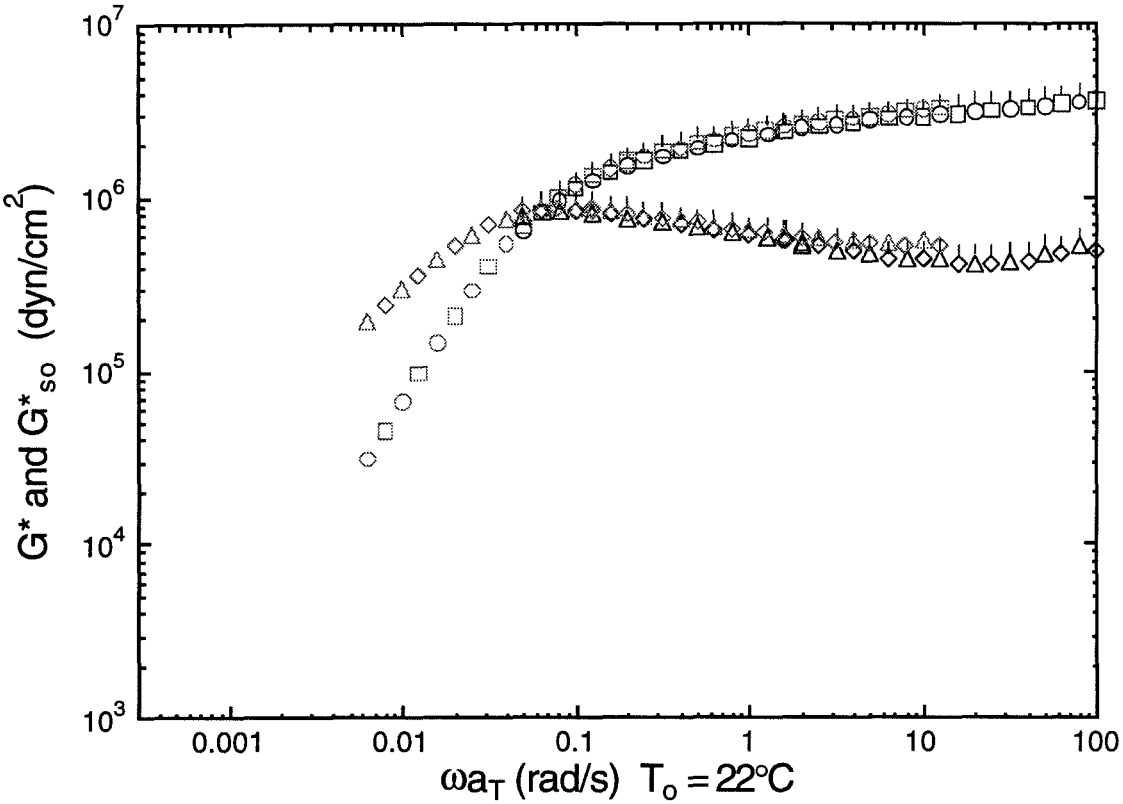

Figure 3.3b: Dynamic moduli determined mechanically (G*) and stress-optically (G^*_{so}) for PI-143. G' ○, G'' ◇, G'_{so} □, G''_{so} Δ.

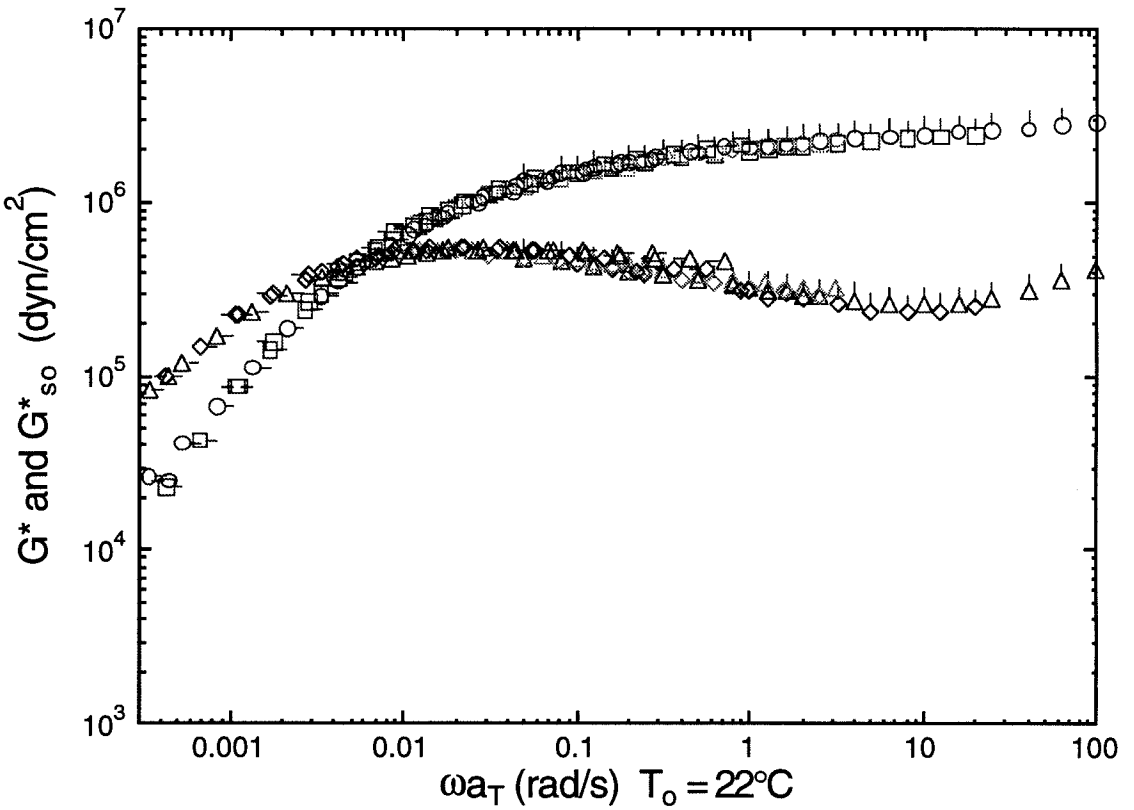

Figure 3.3c: Dynamic moduli determined mechanically (G^*) and stress-optically (G^*_{so}) for PI-170. G' ∘, G'' ◇, G'_{so} □, G''_{so} △.

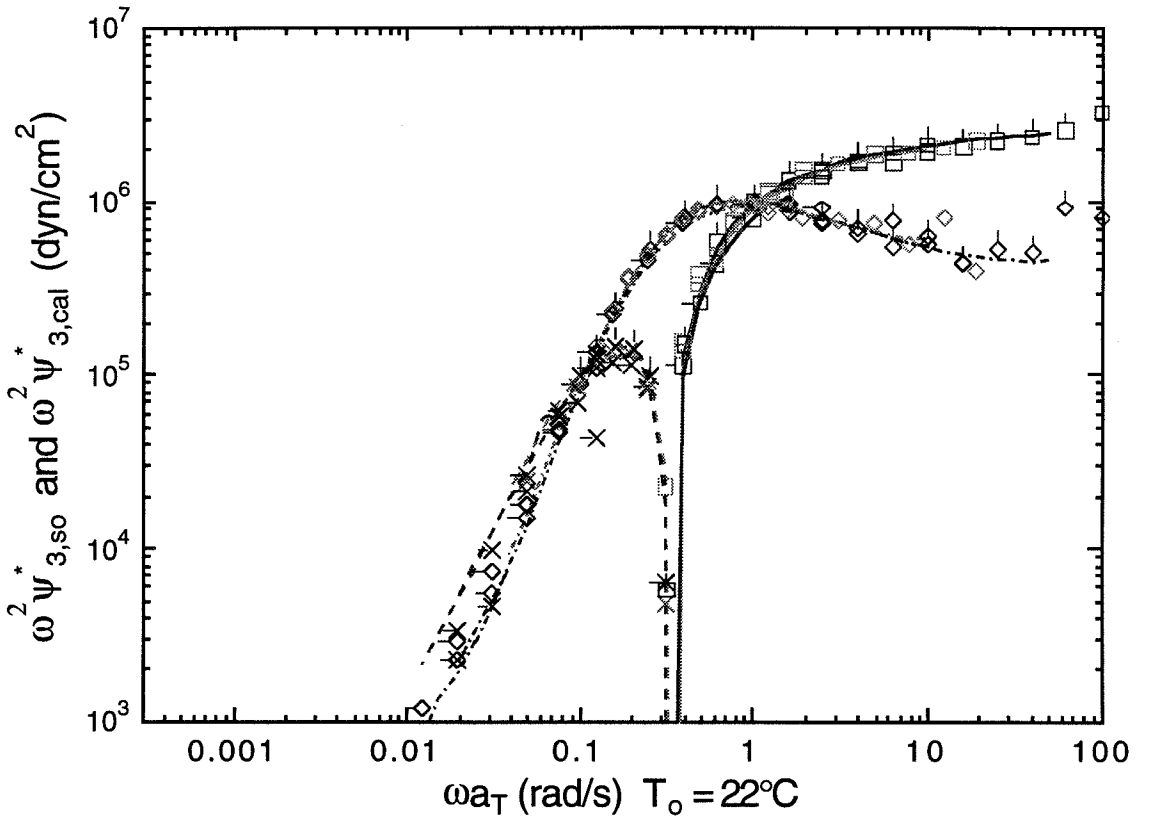

Figure 3.4a: Complex amplitude of the third normal stress difference coefficient for PEP. Stress-optical measurements: $-\omega^2\psi'_3$ $\square$, $\omega^2\psi'_3$ $\times$, and $\omega^2\psi''_3$ $\diamond$. For comparison with Eqs. (3.8), (3.9) and (3.11): $(1-\beta)\cdot[G'(\omega)-\frac{1}{2}G'(2\omega)]$ *solid curve*, $-(1-\beta)\cdot[G'(\omega)-\frac{1}{2}G'(2\omega)]$ *dashed curve*, $(1-\beta)\cdot[G''(\omega)-\frac{1}{2}G''(2\omega)]$ *dot-dash curve*. Temperatures distinguished as in Figure 3.3a.

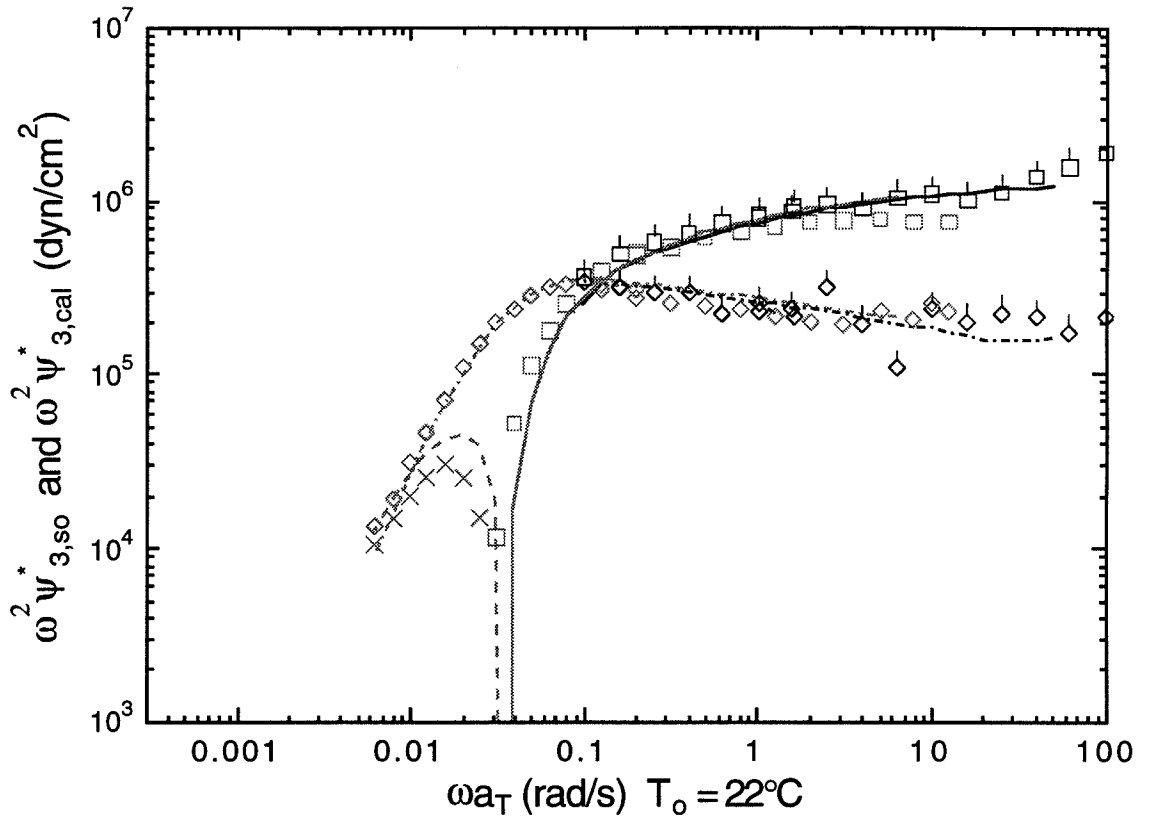

Figure 3.4b: Complex amplitude of the third normal stress difference coefficient for PI-143. Stress-optical measurements: $-\omega^2\psi'_3$ □, $\omega^2\psi'_3$ ×, and $\omega^2\psi''_3$ ◇. For comparison with Eqs. (3.8), (3.9) and (3.11): $(1-\beta)\cdot[G'(\omega)-\frac{1}{2}G'(2\omega)]$ *solid curve*, $-(1-\beta)\cdot[G'(\omega)-\frac{1}{2}G'(2\omega)]$ *dashed curve*, $(1-\beta)\cdot[G''(\omega)-\frac{1}{2}G''(2\omega)]$ *dot-dash curve*. Temperatures distinguished as in Figure 3.3a.

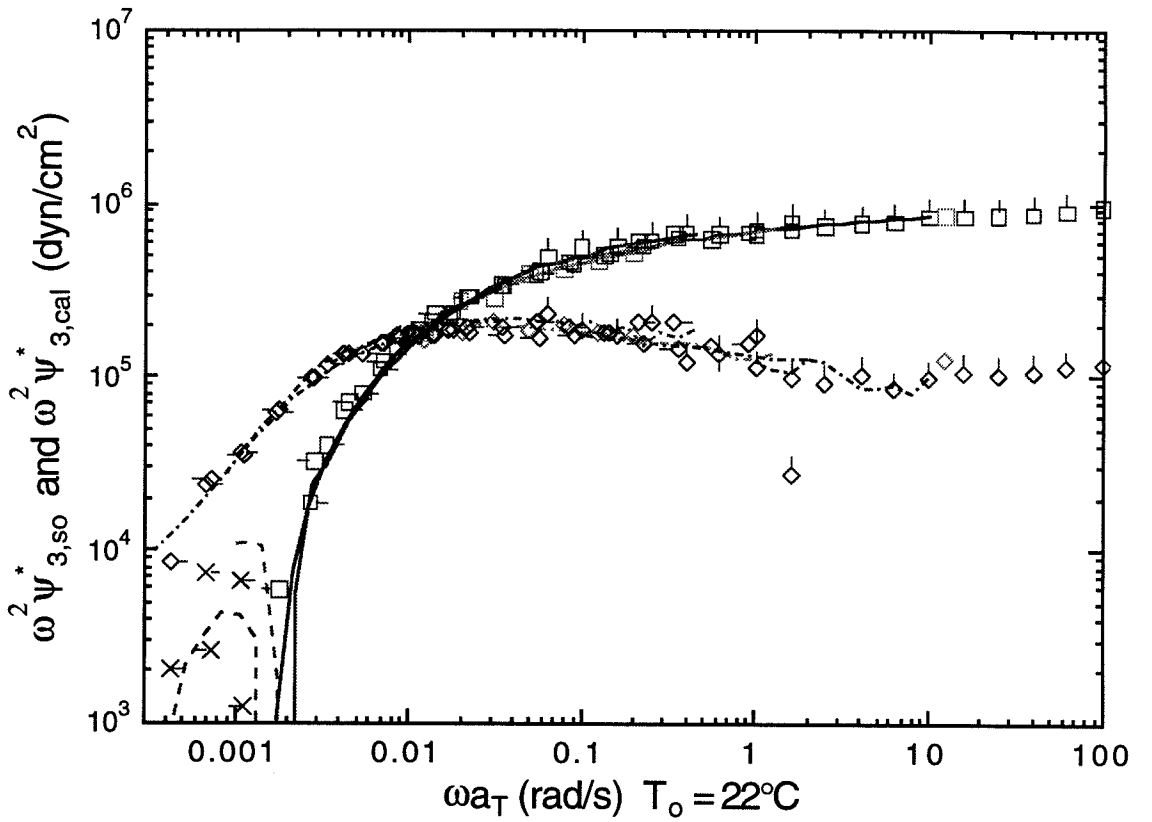

Figure 3.4c: Complex amplitude of the third normal stress difference coefficient for PI-170. Stress-optical measurements: $-\omega^2\psi'_3$ $\square$, $\omega^2\psi'_3$ $\times$, and $\omega^2\psi''_3$ $\diamond$. For comparison with Eqs. (3.8), (3.9) and (3.11): $(1-\beta)\cdot[G'(\omega)-\frac{1}{2}G'(2\omega)]$ *solid curve*, $-(1-\beta)\cdot[G'(\omega)-\frac{1}{2}G'(2\omega)]$ *dashed curve*, $(1-\beta)\cdot[G''(\omega)-\frac{1}{2}G''(2\omega)]$ *dot-dash curve*. Temperatures distinguished as in Figure 3.3a.

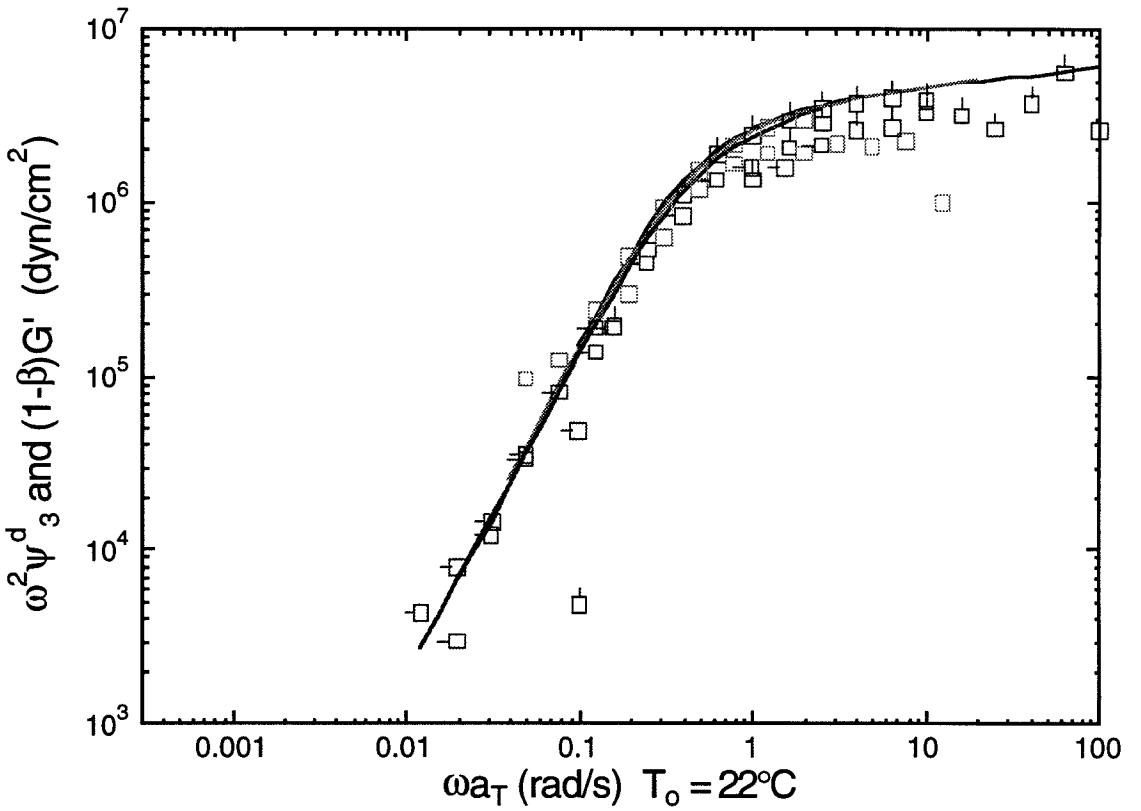

Figure 3.5a: Displacement coefficient of the third normal stress difference for PEP. Stress-optically measured $\omega^2\psi_3^d$ □. For comparison with Eqs. (3.10) and (3.12): $(1-\beta)\cdot G'(\omega)$ *solid curve.* Temperatures distinguished as in Figure 3.3a.

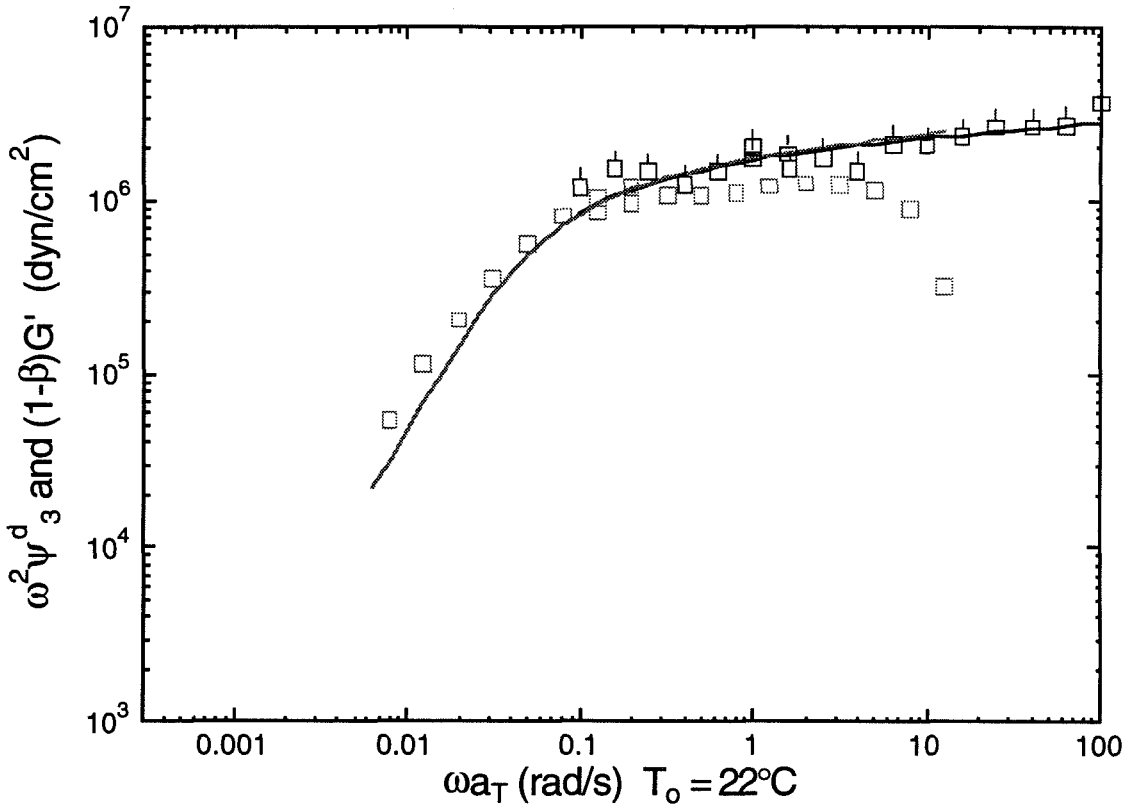

Figure 3.5b: Displacement coefficient of the third normal stress difference for PI-143. Stress-optically measured $\omega^2\psi_3^d$ □. For comparison with Eqs. (3.10) and (3.12): $(1-\beta)\cdot G'(\omega)$ *solid curve.* Temperatures distinguished as in Figure 3.3a.

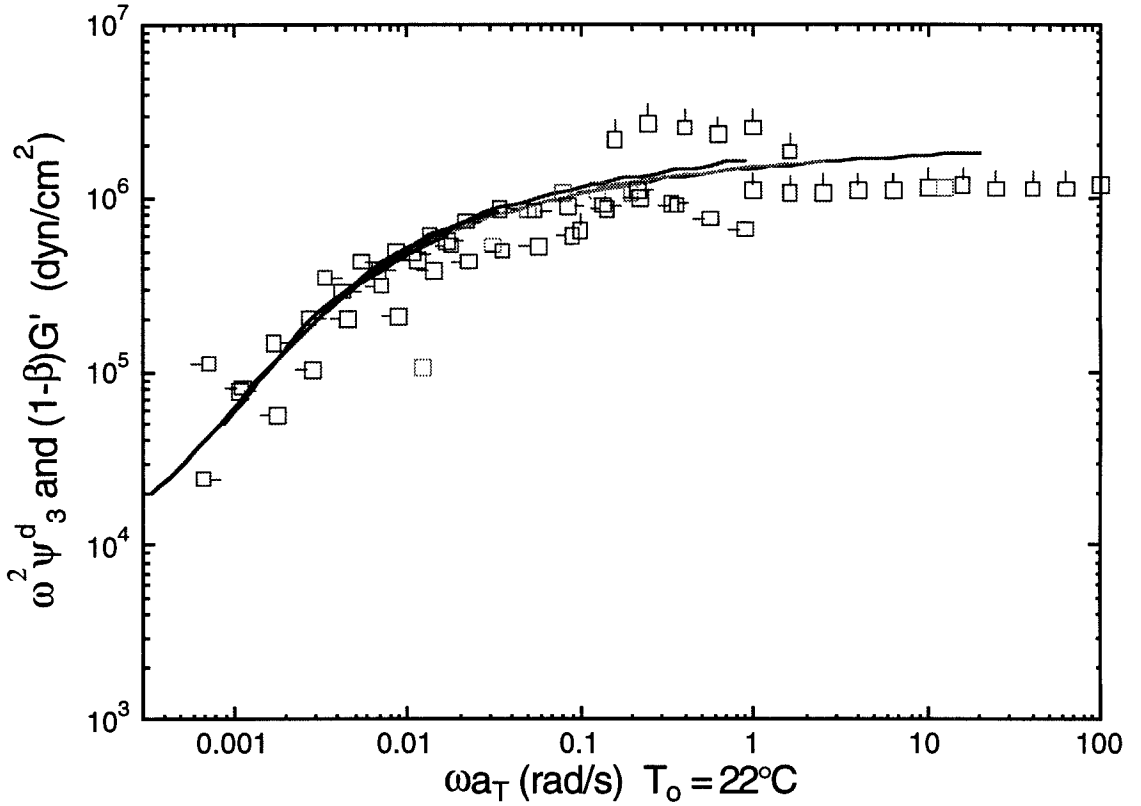

Figure 3.5c: Displacement coefficient of the third normal stress difference for PI-170. Stress-optically measured $\omega^2\psi_3^d$ □. For comparison with Eqs. (10) and (12): $(1-\beta)\cdot G'(\omega)$ *solid curve.* Temperatures distinguished as in Figure 3.3a.

Chapter 4

Molecular and Microstructural Dynamics in Complex Polymer Melts

4.1 Introduction

In the previous chapter, we illustrated the application of stress-optical rule to measure the third normal stress differences in homopolymer melts in a sensitive manner. In this chapter, we will illustrate how the failure of the stress-optical rule, when characterized in a 'precise' manner can reveal molecular and/or microstructural dynamics in miscible polymer blends, side-group liquid-crystalline polymers and block copolymers.

4.1.1 Interpreting the Complex Stress-optical Behavior

The basis of the stress-optic rule in flexible chain polymeric liquids is the simple Hookean elasticity exhibited by a Gaussian coil that is not severely perturbed from equilibrium. It generally requires that all contributions to the birefringence be due to distortion of chain configuration and further requires that all chain segments be optically uniform, *i.e.* that the anisotropic polarizability is the same for all segments [1]. When the chain segments are not optically uniform, as is the case in miscible blends [2, 3], block copolymers [4, 5], and conjugated polymers [6], the stress-optic rule fails. In addition, the stress-optic rule relies on having the stress in the fluid be completely entropic; local distortions that result in enthalpic contributions must be fully relaxed. Thus, the rationale for the stress-optic rule is only valid on timescales beyond the glass-to-rubber transition [7, 8, 9].

Thus, the stress-optic rule requires that both stress and birefringence be dominated by the distortion of chain configuration. In many complex fluids there are

multiple contributions to the birefringence and stress. In general, polymer blends possess phase-separated structure, the distortion of which leads to interfacial contributions to the stress [10] and form contributions to the birefringence[11]. Molecular and microstructural responses to flow contribute differently to birefringence and stress in blends, leading to failure of the stress-optic rule.

Ordered block copolymers (BCPs) and liquid-crystalline polymers (LCPs) are generally birefringent at rest, so the stress-optic rule clearly fails; further, the contributions of the microphase structure and director field to the birefringence and stress do not follow the stress optic rule even in samples that are macroscopically isotropic. Nevertheless, examining the particular way that the stress-optic rule fails provides valuable information regarding the flow behavior of the fluid microstructure. For example, distortion of the equilibrium microphase structure in a BCP contributes differently to the stress [12, 13, 14] and the birefringence; the relative magnitude of the contributions to birefringence and stress provides a signature of the dynamics of the ordered structure.

In a side-group LCP, the flexible backbone may dominate the stress while distortion of the orientation distribution of the mesogens dominates the birefringence. In this case, departure from the stress-optic rule reveals a regime in which the mesogenic side-groups are being subjected to competing forces: forces acting through the spacer group that tethers it to the backbone, and forces imposed by interactions with the surrounding mesogens. The stress-optic rule would hold so long as the orientation of the mesogens is correlated with that of the backbone (i.e., forces through the spacer

dominate); failure of the stress-optic rule implies that competing forces exerted by the surroundings dominate and drive the mesogens to orient differently than backbone orientation would dictate.

As these examples show, measurements of both birefringence and stress provide complementary information on the dynamics of fluids that do not obey the stress-optic rule. This concept has been applied previously to lyotropic liquid crystals to observe pretransitional effects [15], to disordered block copolymer solutions to monitor the relaxation of distinct blocks [4], and to solutions of conducting polymers to monitor the effect of flow on the mean conjugation length [6]. We use the failure of the stress-optic rule to probe the micro-rheology of a variety of complex, flexible chain melts. In particular, we illustrate three types of selectivity that can be achieved: 1) isolating the relaxation of distinct polymeric species, here each component in a miscible blend, 2) discriminating between polymeric and microstructural contributions to the stress, here the conformational and lamellar distortions of an ordered diblock copolymer, and 3) distinguishing the dynamics of topologically different parts of a macromolecule, here the pendant mesogenic groups and backbone of a side-group liquid-crystalline polymer.

4.2 Stress-optical Material Functions

When a sample is subjected to oscillatory shear $\gamma(t) = \gamma_o \sin \omega t$, if γ_o is sufficiently small, the shear stress σ_{12} varies sinusoidal with the same frequency as the applied strain, and with amplitude proportional to γ_o. When this is the case we can define

storage and loss moduli, $G'(\omega)$ and $G''(\omega)$, of the material by

$$\sigma_{12} = \gamma_o[G'\sin\omega t + G''\cos\omega t]. \tag{4.1}$$

We restrict ourselves here to such small strain amplitude that no change in viscoelastic properties is observed even in the block copolymer and liquid-crystalline systems, and even after completing experiments over a wide range of frequency.

In a shear flow, the refractive index tensor $\mathbf{n}$ has the same symmetry as the stress tensor:

$$\mathbf{n} = \begin{bmatrix} n_{11} & n_{12} & 0 \\ n_{12} & n_{22} & 0 \\ 0 & 0 & n_{33} \end{bmatrix}. \tag{4.2}$$

Using the experimental arrangements described in Chapter 2, we observe two particular projections of $\mathbf{n}$. The projection on the 1,2-plane, $\mathbf{n}_{[12]}$, is observed when the optical beam propagates along the vorticity axis. The magnitude of the birefringence in the 1,2-plane, $\Delta n'_{12}$, is equal to the difference between the principle eigenvalues of $\mathbf{n}_{[12]}$. The elements of this tensor are related to the experimentally observed $\Delta n'_{12}$ and orientation angle χ of the principle axis of $\mathbf{n}_{[12]}$ with respect to the flow direction by

$$n_{12} = \frac{1}{2}\Delta n'_{12}\sin(2\chi), \tag{4.3}$$

and

$$n_{11} - n_{22} = \Delta n'_{12}\cos(2\chi). \tag{4.4}$$

The projection of $\mathbf{n}$ on the 1,3-plane, $\mathbf{n}_{[13]}$, is probed when the optical axis is along

the velocity gradient. The principal axes of $\mathbf{n}_{[13]}$ coincide with axes 1 and 3 (*i.e.*,, $\chi = 0$), so its anisotropy is completely described by the magnitude of the birefringence $\Delta n'_{13} = n_{11} - n_{33}$.

Here we show examples that use either n_{12} or $n_{11} - n_{33}$ and their relationship to the dynamic moduli of a given polymer. These examples are selected to illustrate the type of information the present methods provide regarding a wide variety of complex polymer melts. More complex rheological problems require the full capabilities of this instrument. For example, we use σ_{12}, n_{12}, $n_{11} - n_{22}$ and $n_{11} - n_{33}$ together to observe the dynamics and evolution of alignment in lamellar block copolymers during oscillatory shear [16]. We will discuss them in chapter 7.

The behavior of n_{12} during small-amplitude dynamic shear is similar to that of σ_{12}. At sufficiently small strain, we define a complex birefringence coefficient $B^* = B' + iB''$ for n_{12} by

$$n_{12} = \gamma_o[B'\sin\omega t + B''\cos\omega t]. \tag{4.5}$$

To characterize the relative magnitude of the birefringence compared to stress, we define a stress-optic ratio based on the magnitude of the complex birefringence coefficient and the dynamic modulus:

$$SOR = \frac{|B^*|}{|G^*|}\,. \tag{4.6}$$

For homopolymer melts, under the relatively mild flow conditions of interest here, the stress-optical rule would hold and SOR would be independent of shear frequency

and equal to the stress-optic coefficient, C, of the homopolymer.

4.3 Relaxation of Each Species in a Miscible Blend

Even in the relatively simple case of a single phase blend, the stress-optic rule fails unless the relaxation dynamics or stress-optic coefficients of both species are perfectly matched. The stress and refractive-index tensors can be viewed as differently weighted averages of the second moment tensors of the orientation distribution of the end-to-end vectors of the Gaussian submolecules along the two types of chains [17, 3]. In the case of miscible blends, this leads to failure of the stress optic rule in a way that reveals the relaxation dynamics of each species [18].

Here we focus on blends in which both species are well entangled. As in binary blends of entangled homopolymers [19, 20, 21], polydispersity affects the dynamics of each species in miscible blends when the two species are very differently entangled [22]. These effects can be understood by extending theories developed for bidisperse homopolymers to the case of differently entangled blends [23, 24, 25, 26]. The distinctive features of the viscoelasticity of miscible blends arise from the effect of blending on the dynamics of the two species, say A and B. In the plateau and terminal regimes these dynamics may be characterized by the entanglement molecular weights, $M_{e,A}(\phi)$ and $M_{e,B}(\phi)$, and monomeric friction coefficients, $\zeta_A(\phi, T)$ and $\zeta_B(\phi, T)$ [11].

Existing models of the viscoelasticity of miscible blends predict that the dynamics of the two components should both shift the same way with temperature [27, 28], leading to applicability of the time-temperature superposition principle for miscible

blends. However, it has been found that time-temperature superposition is not generally applicable to miscible blends [29, 22]. To predict the viscoelastic properties of blends as a function of blend composition and temperature, it is necessary to develop a better understanding of the effects of intramolecular structure and intermolecular interaction on the dynamics of each species in a blend.

To determine $M_{e,i}$ and ζ_i, it is necessary to observe the contribution of each species to the blend's macroscopic material functions, e.g., to its dynamic modulus $G^*(\omega)$. A blend in which the two components are equally entangled is desired, so that the effect of blending on the relaxation of each component is only to change its $M_{e,i}$ and ζ_i—not to change the shape of its relaxation spectrum by constraint release as well. However, such a blend offers no hope of inferring the relaxation of each species from mechanical measurements [22], since the two relaxations overlap completely. Here we illustrate how quantitative characterization of the precise way the stress-optic rule fails in the blend can be used to determine the contribution of each species to the macroscopic dynamic modulus. The detailed analysis of the data is beyond the scope of this thesis and have been described elsewhere [30].

If the stress-optic coefficients of the individual components are unchanged upon blending, then the dynamic birefringence and stress can be analyzed together to infer the contribution of each species to the macroscopic stress-relaxation dynamics [4]. The basis for this is the connection between the second moment tensor of the segmental orientation of each species to its contribution to both stress and birefringence. Let σ_A and σ_B denote the contributions of species A and B to the shear stress σ_{12}. The

contribution of each species to n_{12} is $C_i\sigma_i$ for $i = A$ or B, neglecting the effects of polydispersity and orientational coupling. Thus, from the measured values of σ_{12} and n_{12}, we can infer the contributions of the individual species:

$$\sigma_A = \frac{C_B\sigma_{12} - n_{12}}{C_B - C_A}, \tag{4.7}$$

and

$$\sigma_B = \frac{C_A\sigma_{12} - n_{12}}{C_A - C_B}. \tag{4.8}$$

In a blend of nearly equally entangled components, σ_A and σ_B are equal to the contributions of the individual species to the stress. In dynamic shear, they may be analyzed to obtain the contribution of each species to the dynamic modulus, and to determine $a_A(\phi)$, $\zeta_A(\phi, T)$, $a_B(\phi)$ and $\zeta_B(\phi, T)$.

We consider blends of 1,4-polyisoprene (PI) and 1,2-polybutadiene, also known as polyvinylethylene (PVE). The glass transition temperatures of these polymers are widely separated ($T_{g,PI} \approx -60°$C and $T_{g,PVE} \approx 0°$C). Their miscibility is well established, but their interaction is very weak [33, 34]. Details regarding the synthesis and characterization of the materials used here are given elsewhere [35, 30]. The dynamic moduli of the homopolymers show a relaxation spectrum characteristic of narrow distribution, linear homopolymers (Figure 4.1). The stress optic ratio is found to be independent of frequency for PI and PVE, except near the dynamic glass transition (i.e., at high frequency in Figure 4.1b), as can be seen by comparing the dynamic modulus to the dynamic birefringence using $G^*_{so} \equiv B^*/C_i(T)$, where $C_i(T)$ is the stress

optic coefficient of homopolymer i at temperature T (Figure 4.1). The stress optic coefficient of PI is an order of magnitude larger than that of PVE, and of opposite sign. This large disparity in the contribution of the two species to the birefringence for a given contribution the stress introduces a form of species-specific labeling: since the dynamic birefringence is disproportionately sensitive to the PIP component, it can be analyzed with the dynamic modulus to cleanly separate the PIP and PVE relaxations—even when they overlap completely.

For the reasons discussed above, we prepare blends of polymers that are the same multiple of their respective entanglement molecular weights ($M_i \approx 30M^o_{e,i}$, where the subscript i denotes the species (A or B), and the superscript o indicates the pure state). Both would be equally entangled in the blend if blending did not change their entanglement molecular weights. Further, if the two species had similar friction coefficients in the blend, $\zeta_A(\phi, T) \approx \zeta_B(\phi, T)$, then both would have nearly the same terminal relaxation time. Indeed, the dynamic modulus of a 50/50 blend is like that of a nearly monodisperse homopolymer (Figure 4.2). Only by expanding the frequency scale, and using a linear modulus scale can we see that time-temperature superposition fails (Figure 4.2, inset), in accord with earlier studies on this blend [22]. The relaxations of the two species overlap so strongly that they cannot be distinguished using mechanical measurements.

While the effects of blending on the shape of the dynamic modulus are subtle, the effects on the stress-optic ratio are unmistakable. In contrast to the frequency-independent stress optic ratios of the two homopolymers, the stress optic ratio of

the blend depends on frequency (Figure 4.3). At high frequency, the SOR has a plateau that nearly equals the weighted average of the two homopolymer stress optic coefficients. As frequency decreases, the stress-optic ratio of the blend increases, and then emerges in a low frequency plateau. The way the stress optic rule fails reveals that the PVE component has a terminal relaxation time that is shorter than the PI component: as the PVE relaxes, it reduces the negative contribution to the stress optic ratio of the blend. At frequencies that lie in the terminal regime for both PVE and PI, SOR emerges into another plateau, but with the contribution of PVE relative to PI reduced.

Based on the analysis described above, we can extract the contribution of each component to the dynamic modulus of this blend [30]. The plateau moduli associated with each species in the 50/50 blend are nearly equal, which corresponds to a modest increase in M_e of PVE and a modest decrease in M_e of PIP upon blending. The small effect of blending on M_e of each species may simply be a consequence of the small difference between the pure component $M_{e,i}^o$ (less than 40%). Blending has a strong effect on the species-specific friction coefficients (Table 4.1). The dynamics of PVE are dramatically faster in the 50/50 blend than in pure PVE. On the other hand, the friction coefficient of PIP is only weakly affected by blending.

The temperature dependence of the two species also differ, giving rise to the failure of time-temperature superposition. In particular, ζ_{PVE} is somewhat more sensitive to temperature than ζ_{PIP}. This is in qualitative accord with a recent deuteron NMR study of local segmental dynamics in a 50/50 PIP/PVE blend, which also found

that blending had a much stronger effect on segmental mobility of PVE than PIP and that the individual species in the blend retained both distinct mobilities but different temperature dependencies [35]. Details on the analysis of the data and results for other blend compositions are beyond the scope of this thesis, and are presented elsewhere [30].

In this section we have illustrated that the methods presented here allowed us to obtain species-specific contributions with sufficient precision to examine even small changes in their magnitude and frequency dependence. Such precision would be very difficult to obtain by performing dynamic birefringence measurements on one instrument and dynamic modulus measurements on another. This approach is well suited to blends in which the components have widely separated stress-optic coefficients, particularly where these are of opposite sign (e.g., PS/PVME and PS/PXE blends). In such cases characterizing the failure of the stress-optic rule provides a relatively facile means to quantitatively determine the effect of blending on the dynamics of each species. In turn, this will provide an improved foundation for predicting blend properties as functions of pure component properties, blend ratio and temperature.

4.4 Dynamics of a Lamellar Block Copolymer

Recently, Larson and coworkers [37] have shown that a variety of layered liquids, including various smectic liquid crystals and lamellar block copolymers, have qualitatively similar dynamic moduli. In particular, at sufficiently low frequency these materials exhibit behavior intermediate between a solid and a liquid. The storage and

loss moduli tend to relax parallel to each other, rather than entering either an elastic plateau or a terminal relaxation. Depending on the system, both the storage and loss moduli may follow power-law behavior with $G' \sim G'' \sim \omega^{\alpha}$. Exponents $\alpha \approx 0.5$ to 0.7 have been reported for lamellar block copolymer melts [36]. Theoretical analysis of the viscoelasticity of unaligned, layered liquids leads to $G' \sim G'' \sim \omega^{\frac{1}{2}}$ [12], in an intermediate regime of frequency in which the distortion of the layers dominates the stress. At sufficiently high frequency, molecular contributions dominate, and at low enough frequency, defects in the material cutoff the low frequency end of the spectrum of layer relaxation modes.

Here we examine the stress-optical behavior of a lamellar block copolymer melt, seeking evidence regarding the cross-over between these three regimes of behavior. The system is a nearly symmetric diblock copolymer with one block of an exactly alternating ethylene-propylene copolymer (PEP) and the other block of ethyl-ethylene (or poly-1-butene) (PEE). The particular diblock (PEP-PEE-SS1) has a molar mass M_w =60 kg/mol and an order disorder transition (ODT) at 156°C.

When the material is cooled from the disordered state to the ordered state it adopts a lamellar morphology locally, but in the absence of an aligning field or surface effect the overall distribution of local orientation is isotropic. The dynamic modulus and birefringence of such an ordered, but unaligned state are shown in Figure 4.4. At high frequencies, the dynamic moduli appear characteristic of entangled polymer melts: as has been previously observed, above a critical frequency, the dynamic moduli are insensitive to the ordering transition [36]. Below the frequency at which the storage

and loss moduli cross ω_x, if the system were disordered it would enter the terminal regime, with $G' \sim \omega^2$ and $G'' \sim \omega$. Relative to this behavior, the ordered block copolymer shows an enhancement of the dynamic modulus, particularly the storage modulus, that is characteristic of layered liquids [37]. Over an intermediate range of frequencies the storage and loss moduli show power law behavior, scaling roughly as $\omega^{0.7}$.

Comparison of the dynamic modulus and the dynamic birefringence shows that the two can be superposed at high frequency, suggesting that the material obeys the stress-optic rule in this regime. This indicates that the shear stress and birefringence n_{12} are both dominated by the distortion of chain conformation. With decreasing frequency, the stress-optic rule is observed to fail, but in a very distinctive way: the elastic-like component of the birefringence G'_{so} is larger than expected based on the stress-optic rule, yet the loss-like component G''_{so} still follows G'' (Figure 4.4). Furthermore, the ratio of the birefringence to stress grows as frequency decreases in a way that suggests power-law behavior with $SOR \sim \omega^{-\frac{1}{2}}$ (Figure 4.5). Recently, Fredrickson and Milner [38] have shown that this stress-optical behavior can be understood by extending the approach of Kawasaki and Onuki [12] to analyze the dynamic birefringence of a layered liquid: they find that the deviations from the stress-optic rule are primarily associated with the elastic-like component of the dynamic birefringence, and that $SOR \sim \omega^{-\frac{1}{2}}$. Both of these predictions are in good agreement with the experimental observations (Figures 4.4 and 4.5). Therefore, it appears that $\omega'_{c,so}$ indicates cross-over from a regime controlled by molecular distortion to a regime controlled

by lamellar distortion. At the lowest frequencies in our experimental range (below $\omega''_{c,so}$), we see that all semblance of the stress-optic rule fails, as G''_{so} begins to deviate from G''. This value for $\omega''_{c,so}$ corresponds to ω_d reported by Koppi et al. [39], which they attributed to defect motions. Therefore, $\omega''_{c,so}$ may indicate a regime where the dynamics at the scale of defects (grains) dominate the macroscopic viscoelasticity.

In summary, the stress-optical behavior of this unaligned lamellar liquid shows the clear signature of a regime where viscoelasticity is controlled by molecular contributions ($\omega > \omega'_{c,so}$), and a regime where it is controlled by the layered structure of the liquid ($\omega''_{c,so} < \omega < \omega'_{c,so}$). In addition, at the lowest experimental frequencies, we begin to see indications of the existence of a distinct regime of behavior at frequencies below $\omega''_{c,so}$, which might be due to the domain structure of the unaligned lamellar phase. Therefore, by applying deformation at a certain frequency one can couple to the desired length scale in the fluid microstructure. This plays a critical role in the flow-alignment behavior of block copolymers and will be discussed in detail in chapter 7.

4.5 Pretransitional Effects in Side-Group Liquid-Crystalline Polymers

To combine the switchable optical properties of small-molecule liquid-crystals with the stability of a glassy matrix, polymers have been synthesized with mesogenic groups pendant to each repeat unit of the flexible backbone through a flexible spacer [40].

These are referred to as side-group liquid-crystalline polymers (SG-LCPs). Relatively few studies have been made of the melt rheology of SG-LCPs. One of the interesting aspects in the rheology of SG-LCPs is the contribution of the mesogens to the macroscopic properties. In relation to the nematic phase, the majority of studies have concluded that the flow behavior is dominated by the flexible backbone [41, 42, 43]. This is rather surprising, given the profound effect of liquid crystallinity on the rheology of small molecule liquid-crystals [44], thermotropic main chain liquid-crystals [45] and lyotropic rod-like LCPs [46]. Experimentally, the isotropic-nematic transition is an ideal situation to study the effect of liquid-crystallinity on the properties of SG-LCPs.

As a liquid crystal in the isotropic phase approaches the nematic phase with increasing concentration or decreasing temperature, the orientation of the mesogens becomes increasingly susceptible to applied fields. In small molecule liquid crystals, the pretransitional effect is readily observed in applied electric or magnetic fields. In polymers, the response to electric and magnetic fields can become prohibitively slow (e.g., thermotropic polymers of $M > 1 \times 10^5$ g/mol). Nevertheless, the effect may be manifested in the stress-optic ratio, since the degree of molecular alignment induced by a particular level of stress diverges as the system moves to the isotropic-nematic transition.

We examine the stress-optical behavior of a thermotropic side-group liquid-crystalline polymer melt near the isotropic-nematic transition. This example illustrates how a simultaneous, quantitative measurements of stress, birefringence and/or

dichroism reveals dynamics at different length scales.

The polymer has a methacrylate backbone with phenylbenzoate mesogens attached through a hexa-methylene spacer (PM6M). Ideally, one would characterize the stress-optical behavior using measurements in the 1,2-plane to provide a direct comparison of n_{12} with the observed component of the stress σ_{12}. However, in the present materials there are two factors that interfere: 1) light scattering by fluctuations in orientational order of the mesogens increases as $T \rightarrow T_{ni}$ and 2) the birefringence becomes sufficiently large that the required optical path length for 1,2-birefringence measurements ($\sim$ 1 cm) leads to a retardation that exceeds $\pi/2$, making determination of the birefringence difficult since $\sin \mu$ is not single valued. Therefore, we examine the birefringence in the 1,3-plane and look for departure from a stress-optical relationship that is found to hold in amorphous polymer melts. In particular, the complex amplitude coefficient of $n_{11} - n_{33}$ is found to be proportional to $G^*(\omega) - \frac{1}{2}G^*(2\omega)$ for entangled, amorphous homopolymers [47]. Therefore, we use the ratio of these two quantities to characterize the departure from the usual stress-optical behavior:

$$SOR_{13} \equiv \frac{\omega^2 |\psi^*_{3,so}(\omega)|}{|G^*(\omega) - \frac{1}{2}G^*(2\omega)|}. \tag{4.9}$$

In the isotropic phase at temperatures well above T_{ni}, the dynamic birefringence in the 1,3-plane is found to obey the usual relatioship, i.e., SOR_{13} is independent of shear frequency.

We study a PM6M that has molar mass $M_w \approx 1.1 \times 10^6$ g/mol and polydispersity $M_w/M_n \approx 1.5$, designated PM6M-11. The dynamic modulus of PM6M-11 in the

isotropic phase is characteristic of a weakly entangled homopolymer with modest polydispersity, showing no unusual frequency dependence and obeying time-temperature superposition even as $T \rightarrow T_{ni}$ (Figure 4.6a). On the other hand, the magnitude of SOR_{13} grows dramatically and becomes frequency dependent as the system approaches the isotropic-nematic transition (Figure 4.6b). As the temperature drops to within 10°C of $T_{ni} = 116$°C, the magnitude of SOR_{13} rises anomalously with decreasing temperature. This is a manifestation of the pretransitional effect, characteristic of liquid crystals in general. Further, as the temperature approaches within approximately 1°C of T_{ni}, the SOR_{13} becomes frequency dependent. This behavior is not yet understood.

In interpreting the frequency dependence of SOR_{13}, two critical questions arise. First, is the frequency dependence a consequence of polydispersity, which is believed to lead to the shear rate dependent stress-optic ratio of lyotropic, rod-like polymer liquid crystals near the isotropic-to-nematic transition? Second, is the observed frequency dependence really indicative of failure of the stress-optic rule, or is it instead due to failure of the usual relationship between the third normal stress and the shear stress? In relation to the first question, we simply indicate that the dynamic birefringence in the pretransitional regime is dominated by the ordering tendency of the mesogens. Since all mesogens are identical, there is no analog of the polydispersity that gives rise to shear rate dependence of the stress optical ratio in lyotropic liquid crystals [15]. Therefore, we conclude that polydispersity is not the cause for the peculiar frequency dependence of SOR_{13}.

To address the second question, we study a sample that is labeled on the backbone by replacing pendant hydrogens with deuterium ($M_w \approx 3 \times 10^6$ g/mol, $M_w/M_n \approx 5$); this material is designated here as PMd6M-30. Without a direct measurement of the third normal stress difference $N_3 \equiv \sigma_{11} - \sigma_{33}$ it is difficult to test the constitutive relation that leads to proportionality between the complex amplitude of N_3 and the denominator of SOR_{13} (Eq. 4.9). The birefringence in this system is dominated by the orientation of the side-groups, owing to their high polarizability. So we cannot use the 1,3-birefringence as an indicator of N_3. However, it is likely that the stress is dominated by the polymeric backbone, since we are in the isotropic phase and applying shear frequencies that are slow compared to local relaxations (including reorientation of side-groups with respect to the backbone). Indeed, the observation that the dynamic modulus in the isotropic phase is unaffected by proximity to T_{ni} indicates that the backbone continues to dominate the stress. If we suppose this is the case, then we may examine the possibility of the failure of the constitutive relation referred to above by monitoring the dynamic orientation of the backbone projected on the 1,3-plane. To observe the orientational behavior of the backbone, we use infrared dichroism applied to a sample that has been selectively labeled with deuterium on the backbone (PMd6M-30).

During oscillatory shear, the dichroism in the 1,3-plane $\Delta n''_{13}$ has a displacement component and a complex amplitude, analogous to the behavior of N_3:

$$\Delta n''_{13} = (\gamma_o)^2[\omega^2\psi^d_{3,D} + \omega^2\psi'_{3,D}\sin\omega t + \omega^2\psi''_{3,D}\cos\omega t], \tag{4.10}$$

where $\psi^d_{3,D}$ and $\psi^*_{3,D} = \psi'_{3,D} - i\psi''_{3,D}$ are the displacement coefficient and complex amplitude of the 1,3-dichroism. If indeed these were proportional to the displacement and complex amplitude of N_3 and if the latter were related to G^* as is observed for other isotropic polymer melts, then we would find

$$-\omega^2\psi^*_{3,D} = c[G^*(\omega) - \frac{1}{2}G^*(2\omega)] \tag{4.11}$$

and

$$\omega^2\psi^d_{3,D} = cG'(\omega), \tag{4.12}$$

where c is a constant [21]. We compare the experimental values of $\omega^2\psi^*_{3,D}$ to its expected relationship to the dynamic moduli using $\omega^2\psi^*_{3,cal} \equiv c[G^*(\omega) - \frac{1}{2}G^*(2\omega)]$ in Figure 4.7a. The isotropic-nematic transition temperature of PMd6M-30 is $T_{ni} =$ 116°C. Even at a temperature within 1°C of T_{ni}, the frequency dependence of the observed displacement and complex amplitude of the 1,3-dichroism is in good accord with that anticipated on the basis of the constitutive relation previously established for amorphous melts, indicating that the dynamics of the polymeric backbone is similar to that of an amorphous polymer. Therefore it is unlikely that failure of this relation is responsible for the anomalous behavior of SOR_{13}.

Some clues to the origin of the anomalous stress-optical behavior can be obtained from a comparison of the frequency dependence of the 1,3-birefringence and the 1,3-dichroism associated with the backbone. Whereas the 1,3-dichroism obeys Eq. 4.11-4.12, there exists no constant of proportionality that can superpose the corresponding

material functions for the 1,3-birefringence. The closest correspondence that can be achieved is one that superposes the displacement coefficient of the birefringence with the storage modulus and superposes $\omega^2\psi^*_{3,so}$ with $G^*(\omega) - \frac{1}{2}G^*(2\omega)$ at low frequency. Above a critical frequency, the backbone and mesogens show different dynamic responses. Thus, the partial decoupling of the dynamics of the mesogens and the backbone is sufficient that the chain can retain behavior characteristic of an amorphous, isotropic melt, even when in close proximity to the isotropic-nematic transition produces anomalous behavior of mesogen orientation compared to the stress.

The precise origin of the distinctive frequency dependence of the orientation of the mesogens relative to the backbone is not known, but the fact that the deviation is pronounced at high frequency suggests that the dynamic shear must be sufficiently rapid to couple to orientation fluctuations in order to excite the unusual response. Indeed, as $T \rightarrow T_{ni}$, the frequency above which deviation from the stress-optic rule is observed moves to lower frequency: at 120°C deviations are observed above 20 rad/s, at 118°C deviations are observed above 0.5 rad/s (Figure 4.7b), and at 117.5°C the stress-optic rule fails throughout the accessible frequency range ($\omega > 0.01$ rad/s). Such a strong temperature dependence of the frequency above which the stress-optic rule fails cannot be explained by the time-temperature shift, which is quite small over this temperature range of only 2.5°C.

4.6 Conclusion

As the examples of miscible blends, ordered block copolymers and side-group liquid-crystalline polymers illustrate, quantitative comparison of birefringence, dichroism, and stress can provide rich information regarding the molecular and microstructural dynamics that underlie the flow behavior of complex polymer melts. Such quantitative comparisons can be quite difficult when optical and mechanical measurements are performed on separate instruments, as is done in most rheo-optical studies. Difficulties arise when the sample is changing with time (e.g., during a chemical reaction or flow-induced change), or is particularly sensitive to temperature (e.g., near a phase transition), or behaves nonlinearly with strain (e.g., normal stress differences or their optical analogues). Therefore, we have developed instruments to perform optical and mechanical measurements simultaneously. These are particularly well suited to study the dynamics of polymer melts over a wide range of frequency and temperature.

The key advantage of combining optical methods with simultaneous mechanical measurements is that it enables us to establish unambiguous relationships between microstructure and the macroscopic stress and strain history. These relationships are becoming increasingly important as we process progressively more advanced materials, whose properties require stringent control of molecular alignment and microstructure.

Bibliography

[1] Kuhn, W.; Grün, F., *J. Poly. Sci.*, **1946**, 1, 193.

[2] Zhao, Y.; Jasse, B; Monnerie, L., *Poly. Comm.*, **1990**, 31 (10), 395.

[3] Zhao, Y.; Jasse, B; Monnerie, L., *Polymer*, **1989**, 30 (9), 1643.

[4] Osaki, K.; Takatori, E.; Ueda,M.; Kurata, M.; Kotaka, T., *Macromolecules*, **1989**, 22 (5), 2457.

[5] Lodge, T. P.; Lodge, S. A., *Rheol. Acta*, **1992**, 31 (1), 32.

[6] Pearson, D. S.; Chance, R. R.; Kiss, A. D.; Morgan, K. M.; Peiffer, D. G., *Syn. Metal*, **1989**, 28 (3), 689.

[7] Read, B. E., *Polymer*, **1962**, 3, 143.

[8] Read, B. E., *Polymer Eng. Sci.*, **1983**, 23 (3), 835.

[9] Inoue, T.; Okamoto,H.; Osaki, K., *Macromolecules*, **1991**, 24 (20), 5670.

[10] Gramespacher, H.; Meissner, J., *J. Rheol.*, **1992**, 36 (6),1127.

[11] Doi, M.; Edwards, S. F., *The Theory of Polymer Dynamics* (Clarendon Press, Oxford, **1986**.

[12] Kawasaki, K.; Onuki, A., *Phys. Rev. A*, **1990**, 42, 3664.

[13] Amundson, K.; and Helfand, E., *Macromolecules* **1993**, 26 (6), 1324.

[14] Wang Z.-G., *J. Chem. Phys.*, **1994**, 100 (3), 2298.

[15] Mead, D. W.; Larson, R. G., *Macromolecules* **1990**, 23 (9), 2524.

[16] Kannan, R. M.; Kornfield, J. A., *Macromolecules*, **1994**, 27, 1177.

[17] Bouton, C.; Arrondel, V.; Rey, V.; Sergot, P.; Manguin, J. L.; Monnerie, L., *Polymer*, **1989**, 30 (8), 1414.

[18] Saito, H.; Miyashita, H.; Inoue, T., *Macromolecules*, **1992**, 25, 1824.

[19] Struglinski, M. J.; Graessley, W. W., *Macromolecules* **1985**, 18 (12), 2630.

[20] Kornfield, J. A.; Fuller, G. G.; Pearson, D. S., *Macromolecules*, **1989**, 22 (3),1334.

[21] Kornfield, J. A.; Fuller, G. G.; Pearson, D. S., *Macromolecules*, **1991**, 24 (19), 5429.

[22] Roovers, J.; Toporowski, P. M., *Macromolecules*, **1992**, 25 (13), 3454.

[23] Rubinstein, M.; Helfand, E.; Pearson, D. S., *Macromolecules*, **1987**, 20, 822.

[24] Doi, M.; Graessley,W. W.; Helfand,E.; Pearson, D. S., *Macromolecules*, **1987**, 20 (8),1900.

[25] de Cloizeaux, J., *Makromol. Chem.-Macro. Symp.*, **1991**, 45, 153.

[26] Watanabe, H.; Tirrell, M., *Macromolecules*, **1989**, 22, 927.

[27] Roland, C. M., *J. Polym. Sci., Polym. Phys. Ed.*, **1988**, 26 (4), 839.

[28] Tsenoglou, C., "Viscoelasticity and Self-Diffusion in Miscible Heteropolymer Blends," New Trends in Physics and Physical Chemistry of Polymers, Plenum Press, **1992**, 375.

[29] Colby, R. H., *Polymer*, **1989**, 30 (7), 1275.

[30] Arendt, B. H.; Kannan, R. M.; Zewail, M.; Kornfield, J. A.; Smith, S., "Dynamics of Each Species in Miscible Polymer Blends of Polyisoprene and Polyvinylethylene," *Rheol. Acta*, accepted in March 1994.

[31] Janeschitz-Kriegl, H., *Polymer Melt Rheology and Flow Birefringence*, Springer-Verlag, New York, **1983**.

[32] Doi, M.; Pearson, D. S.; Kornfield, J. A.; Fuller, G. G., *Macromolecules*, **1989**, 22 (3), 1488.

[33] Trask, C. A.; Roland, C. M., *Macromolecules*, **1989**, 22, 256.

[34] Tomlin, D. W.; Roland, C. M., *Macromolecules*, **1992**, 25 (11), 2994.

[35] Chung, G.-C.; Kornfield, J. A.; Smith, S. D., *Macromolecules*, **1994**, 27, 964.

[36] Rosedale, J. H.; Bates, F. S., *Macromolecules*, **1990**, 23, 2329.

[37] Larson, R. G.; Winey, K. I.; Patel, S. S.; Watanabe, H.; Bruinsma, R., *Rheol. Acta*, **1993**, 32 (3), 245.

[38] Fredrickson, G. H.; Milner, S. T., "Viscoelasticity and Microstructural Evolution of Block-Copolymer Lamellar Phases Under Shear", ACS Abstracts, **1993**, 206 (Poly.), 411.

[39] Koppi, K. A.; Tirrell,M.; Bates, F. S.; Almdal, K.; Colby, R. H., *J. Physique II*, **1992**, 2 (11), 1941.

[40] McArdle, C. B., ed., *Side-Chain Liquid Crystal Polymers* Blackie, London, **1989**.

[41] Zentel, R.; Wu, J., *Makromol. Chem.*, **1986**, *187*, 1727.

[42] Fabre, P.; Veyssie, M., *Mol. Cryst. Liq. Cryst. Letters*, **1987**, *4*, 99.

[43] Colby, R.H.; Gillmore, J.R.; Galli, G.; Laus, M.; Ober, C.K.; Hall, E., *Liq. Cryst.*, **1993**,13 (2), 233.

[44] Porter, R. S.; Johnson, J. F. in *Rheology*, Eirich, F. R., ed.; Academic Press: New York, **1967**, Vol. 4, Chapter 5.

[45] Wissbrun, K. F.; Griffin, A. C. *J. Polym. Sci., Polym. Phys. Ed.*, **1982**, *20*, 1835.

[46] Baird, D. G. in *Liquid Crystalline Order in Polymers*, Blumstein, A., ed.; Academic Press: New York, 1978.

[47] Kannan, R. M.; Kornfield, J. A., *Rheol. Acta*, **1992**, 31 (6), 535.

Table 4.1: Friction Coefficients of Each Species in a 50/50 PIP/PVE Blend.

T (°C)	Monomeric Friction Coefficient ζ_i (g/s)			
	pure PVE	50/50 blend		pure PIP
		PVE	PIP	
22	3.5×10^{-4}	8.9×10^{-6}	2.4×10^{-6}	1.0×10^{-6}
45	4.1×10^{-6}	7.2×10^{-7}	2.7×10^{-7}	2.4×10^{-7}
80	8.3×10^{-8}	5.9×10^{-8}	3.1×10^{-8}	5.1×10^{-8}

These values were obtained using the cross-over frequency of the appropriate dynamic moduli to estimate the terminal relaxation time according to $\tau_d \approx 2/\omega_x$, and relating τ_d to the monomeric friction coefficient as indicated by the reptation model (Doi & Edwards 1986): $\tau_d = (\zeta N M^2 b^2)/(\pi^2 k_b T M_e m_o)$, where N is the degree of polymerization, ζ is the monomeric friction coefficient, M is the molar mass, b is the monomeric segment length determined from the radius of gyration ($R_g^2 = Nb^2/6$), k_bT is the thermal energy, M_e is the entanglement molecular weight, and m_o is the monomer molar mass. Literature values for b were used: 6.6 Å for PIP and 6.0 Å for PVE.

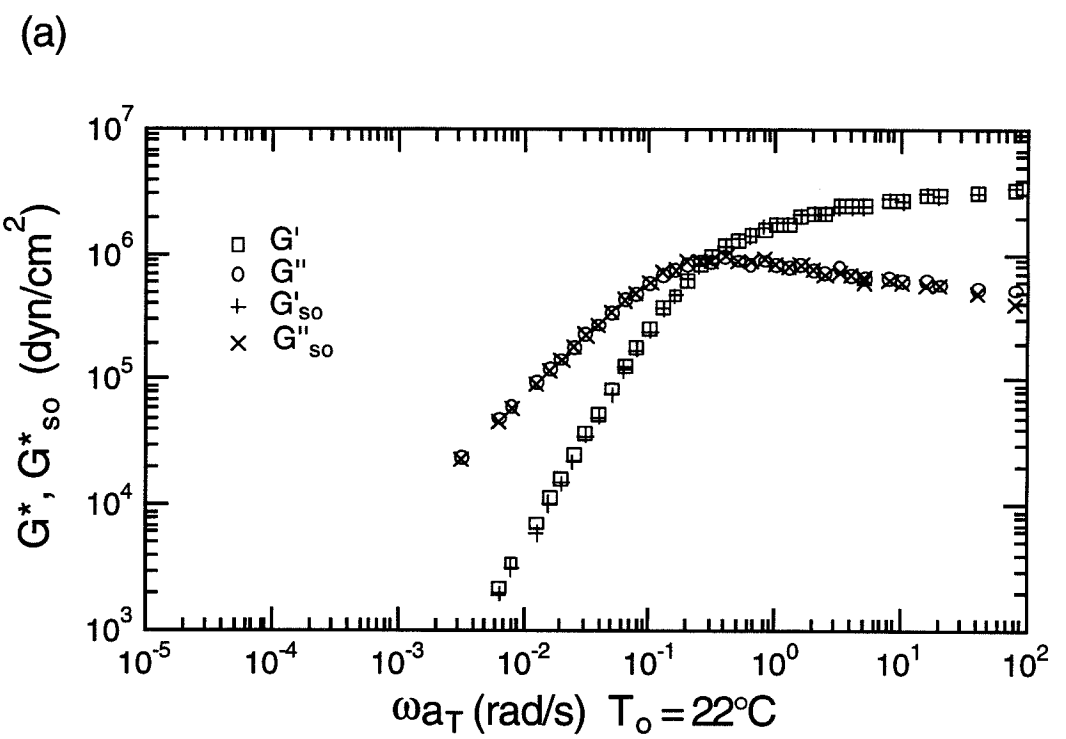

Figure 4.1a: Dynamic modulus and birefringence of polyisoprene (PIP) of $M_w = 300k$.

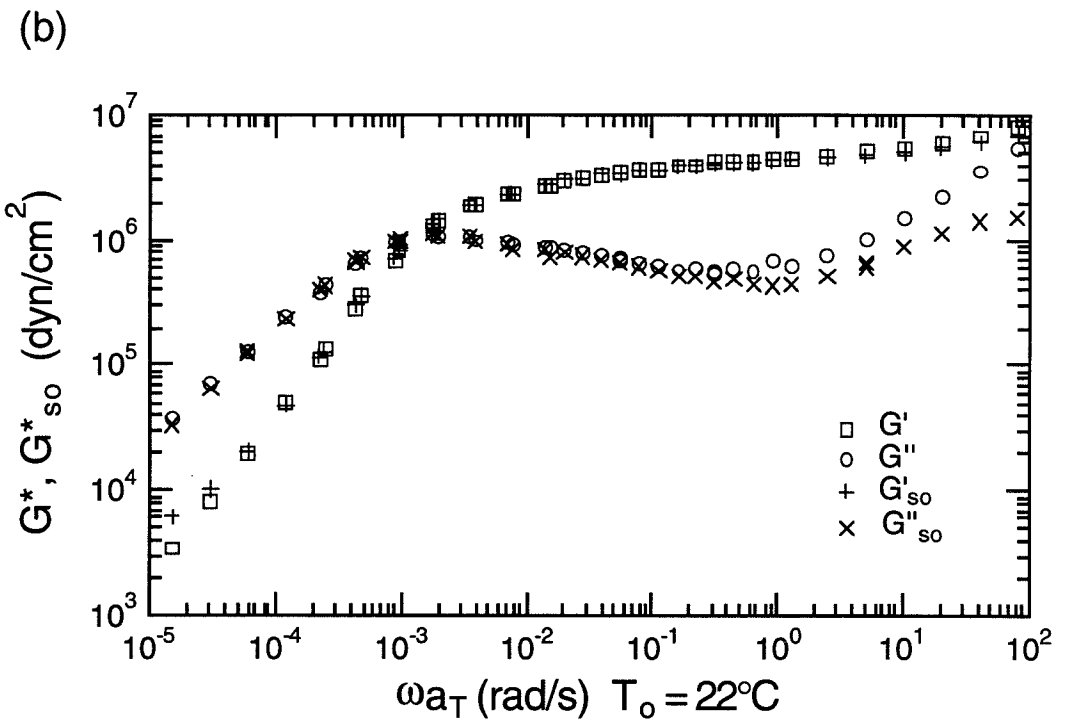

Figure 4.1b: Dynamic modulus and birefringence of polyvinylethylene (PVE) of $M_w = 130k$.

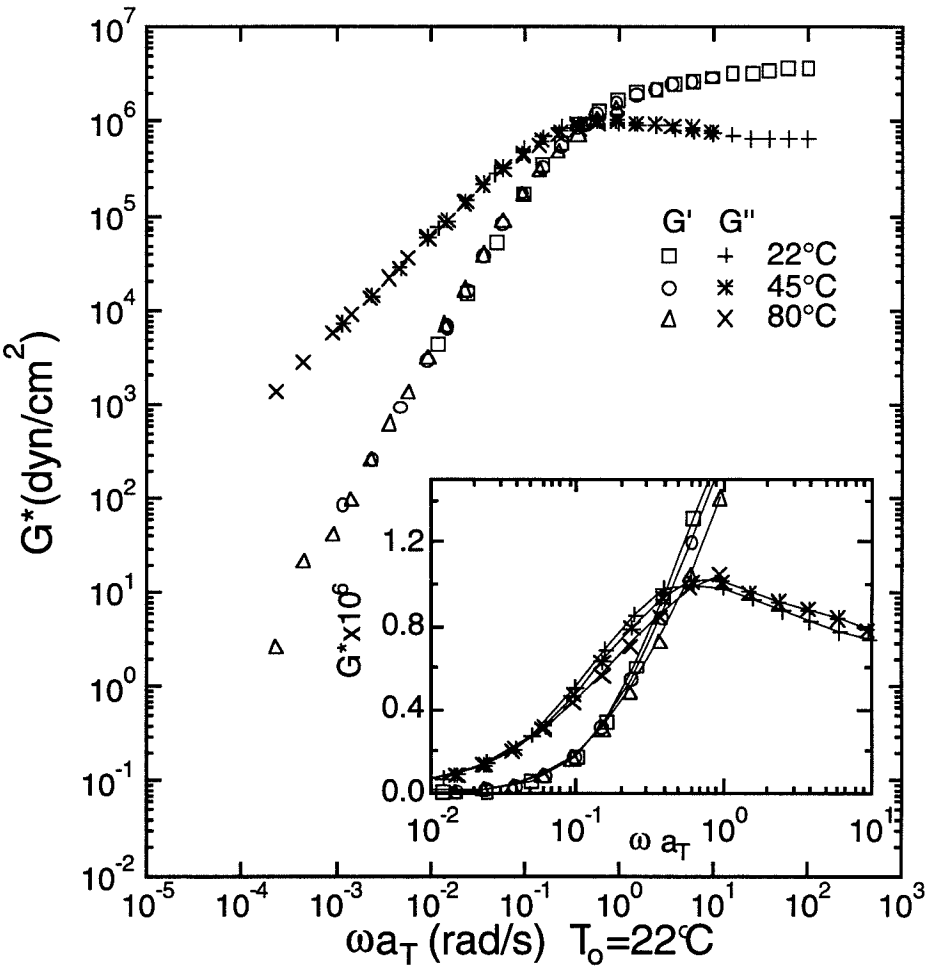

Figure 4.2: Dynamic modulus of a 50/50 w/w PIP/PVE blend, with PIP of $M_w = 180k$ and PVE of of $M_w = 100k$. The shift coefficients a_T are chosen such that the low-frequency tail of the data taken at different temperatures superimpose.

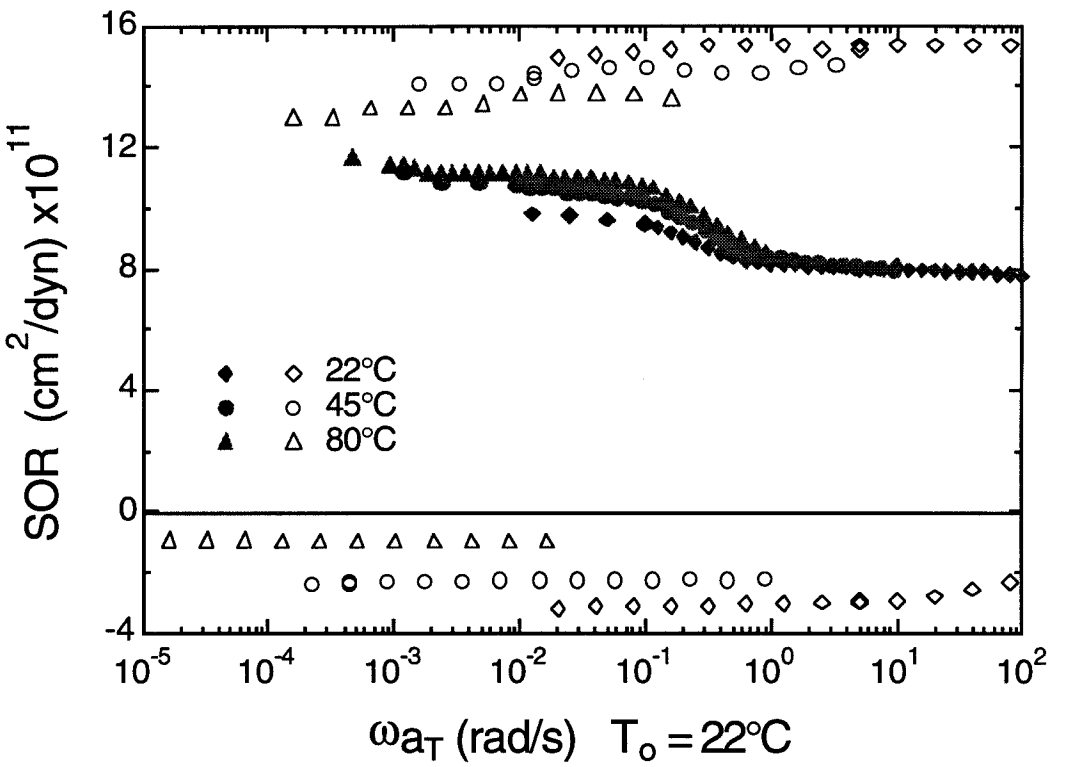

Figure 4.3: Failure of the stress optic rule for a 50/50 w/w PIP/PVE blend.

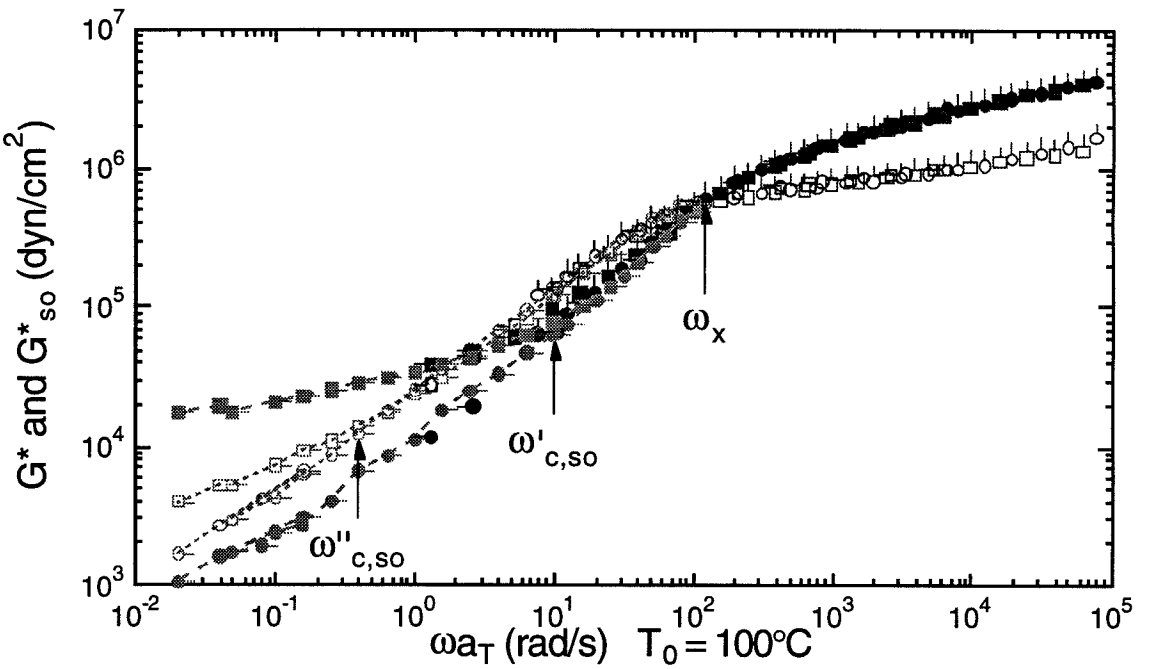

Figure 4.4: Dynamic modulus, G^*, and dynamic birefringence G^*_{so} of ordered, but unaligned PEP-PEE-SS1 (master curves with respect to a reference temperature of 100°C).

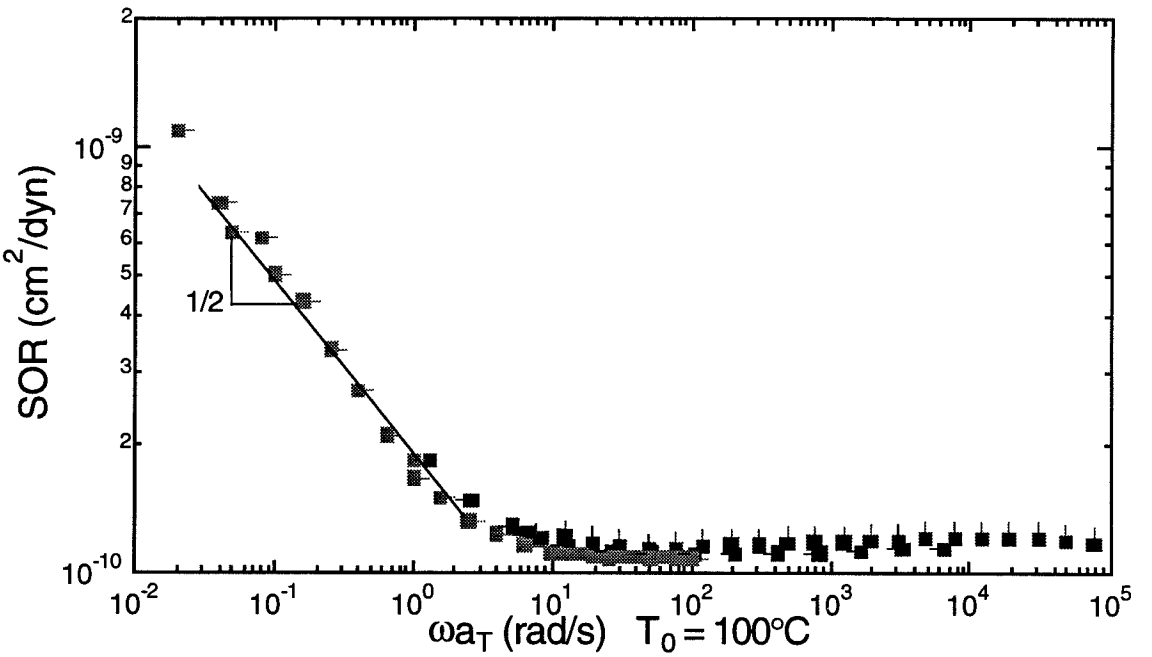

Figure 4.5: Amplitude-based stress-optic ratio of ordered, but unaligned PEP-PEE-SS1.

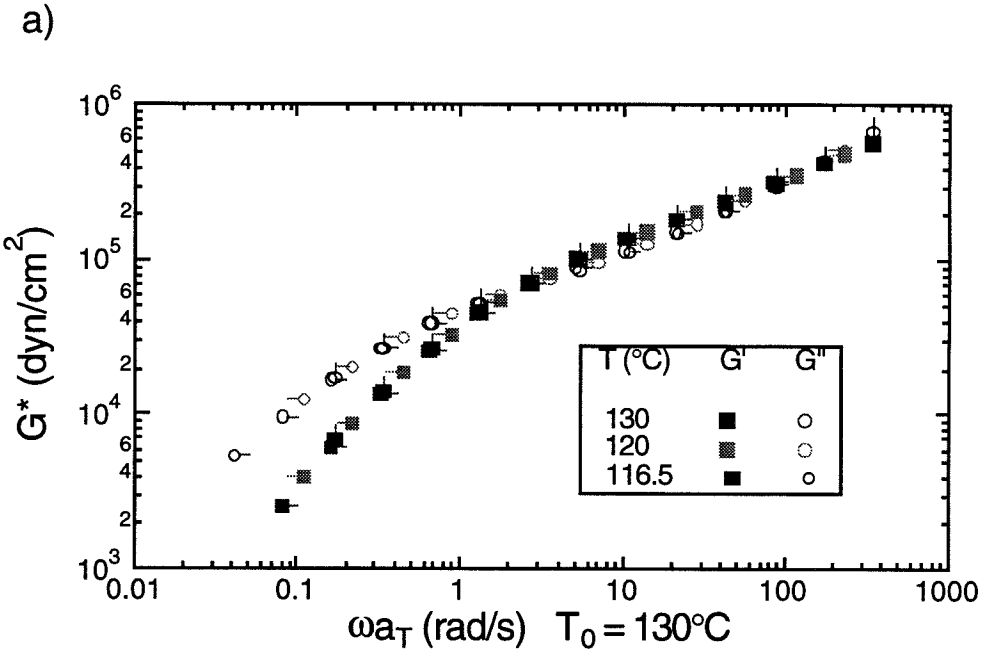

Figure 4.6a: Dynamic Modulus of the SG-LCP PM6M-11 (master curves with respect to a reference temperature of 130°C).

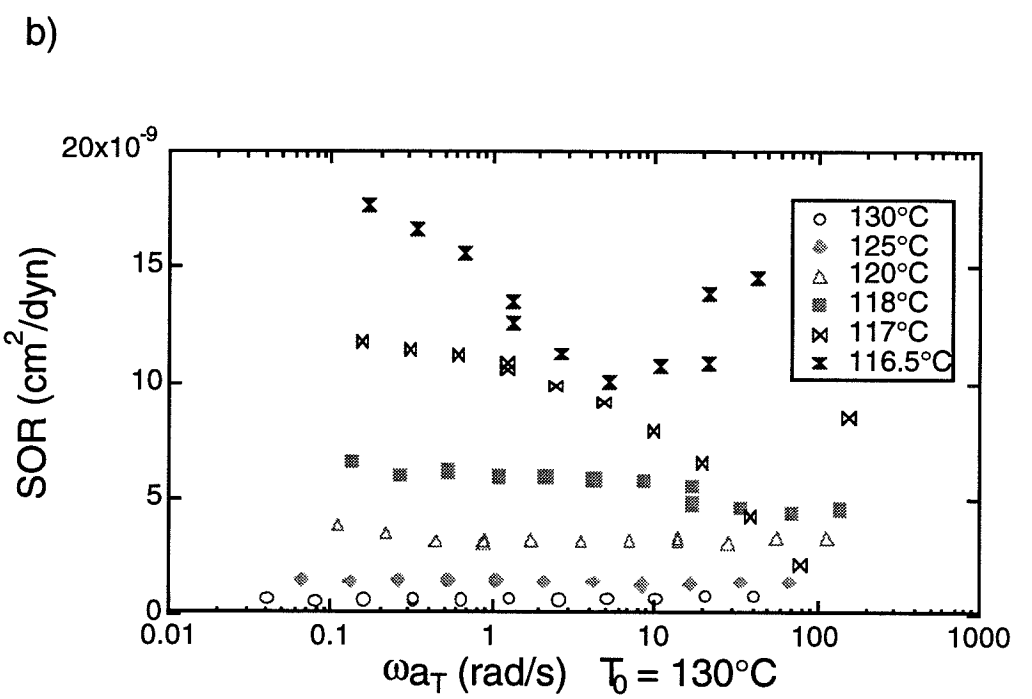

Figure 4.6b: Stress-optic behavior of PM6M-11 in the isotropic phase near T_{ni}.

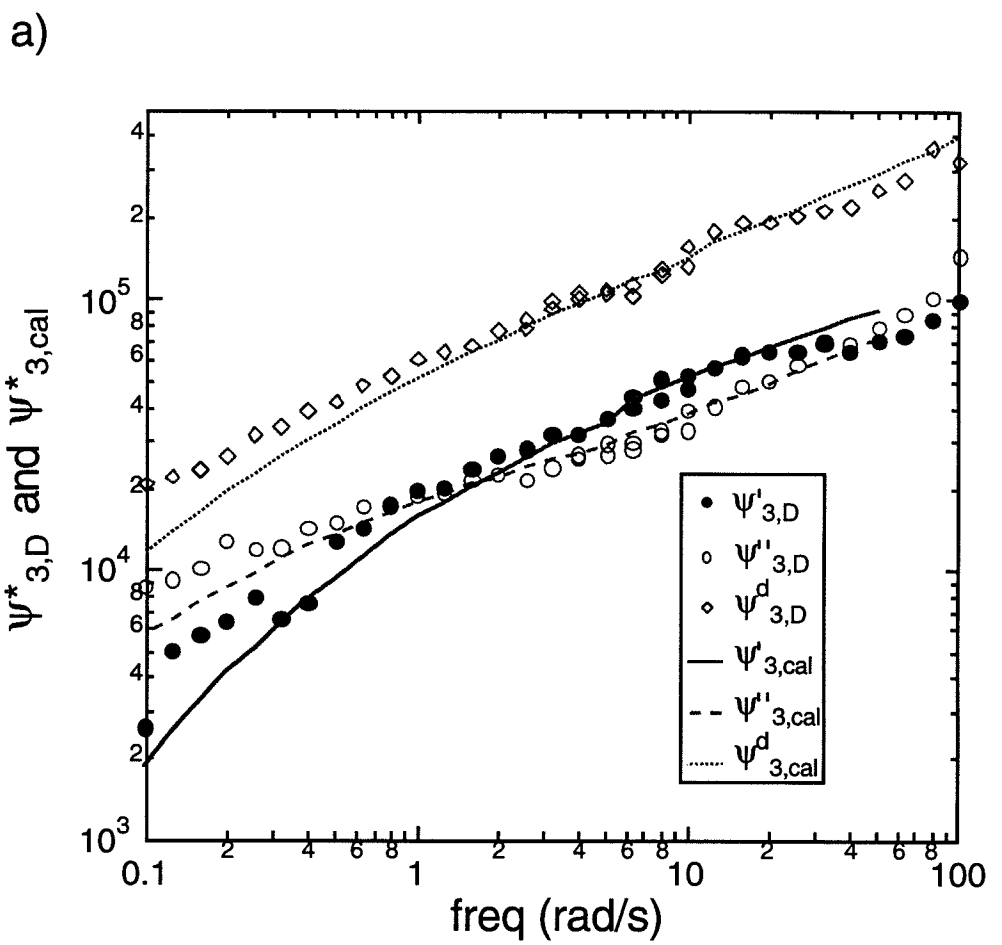

Figure 4.7a: Comparison of the dynamic IR dichroism of a backbone-labeled PMd6M-30 observed at $T = T_{ni} - 1°C$, with the calculated values from the constitutive relationship.

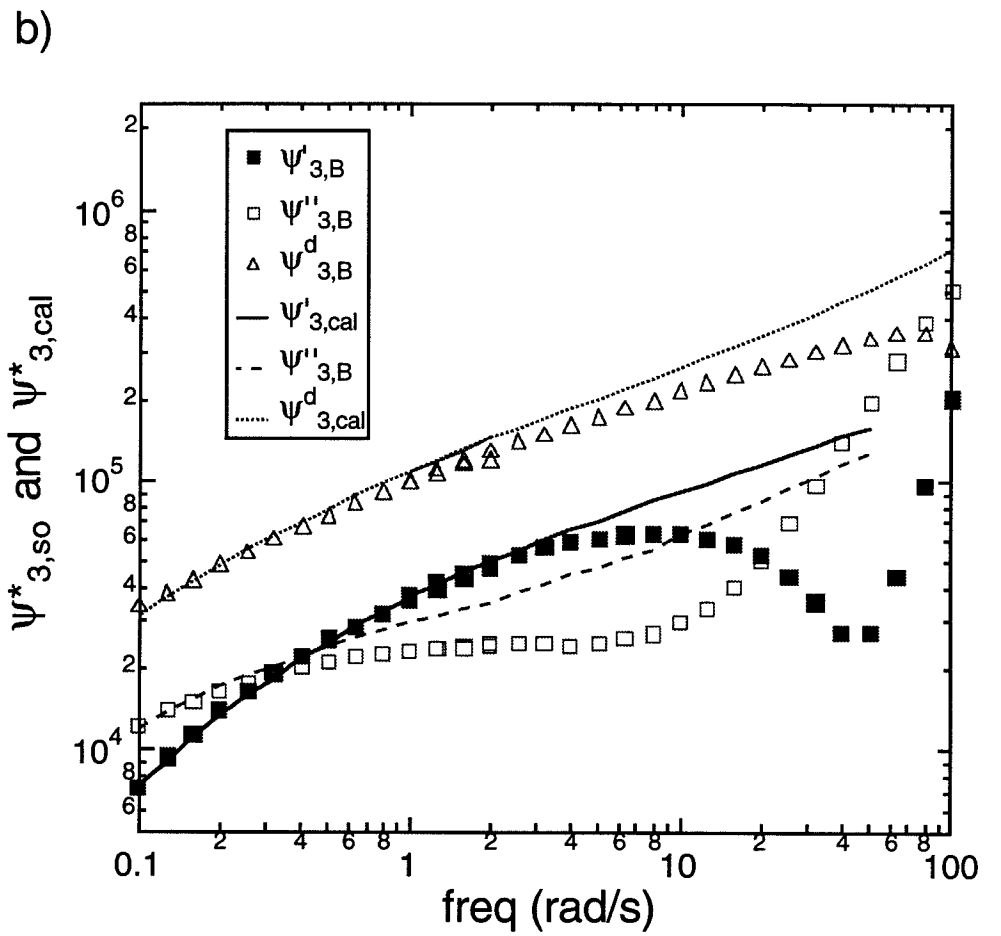

Figure 4.7b: Comparison of the dynamic birefringence of PM6M-11 observed at $T = T_{ni} - 1°C$, with the values calculated from the constitutive relationship.

Chapter 5

Rheology of Side-Group Liquid-Crystalline Polymers: Effect of Isotropic-Nematic Transition and Evidence of Flow Alignment

5.1 Introduction

Side-group liquid crystalline polymers (SG-LCP) consist of a flexible polymeric backbone with mesogenic units attached to it as side groups (Figure 5.1). The combination of anisotropic phase structure, capacity to freeze liquid-crystalline order into the glassy state and ability to manipulate the orientation of their optical axis using applied fields makes SG-LCPs attractive for a variety of potential commercial applications, including optical data storage media, nonlinear optical materials and stress sensors [1]. To realize these applications, it is imperative to understand the rheology of these materials and the effect of flow history on molecular alignment, which controls their optical and mechanical properties. Although considerable work has been done on main-chain and rigid-rod polymer liquid crystals, relatively little research has been devoted to the rheological behavior of SG-LCPs.

The few studies of SG-LCP melt rheology that have been reported [2, 3, 4] conclude that the flexible backbone dominates the rheology of nematic SG-LCPs, suppressing any significant manifestation of their liquid crystalline character. This is rather surprising, given the profound effect of liquid crystalline order on the rheology of small-molecule LCs [5], thermotropic main-chain LCPs [6], and lyotropic rod-like LCPs [7, 8]. The fluid dynamics of SG-LCP melts are expected to be more complex than initial studies suggest, because they depend not only on the polymeric nature of the backbone, but also on the liquid crystalline nature of the mesogen and the coupling between the backbone and mesogen dynamics. Therefore, it is important to determine the role of liquid crystallinity in SG-LCP rheology, and the origin of the

qualitative distinctions between SG-LCPs and other types of liquid crystals.

Further, like ordered block-copolymer (BCPs) melts, SG-LCPs belong to a class of polymeric liquids that have intrinsically anisotropic microstructure and properties. This general characteristic is believed to be responsible for the flow-induced alignment observed in BCPs [9]. On this basis, one would expect flow alignment to occur in SG-LCPs as well. Earlier studies suggested that the liquid crystalline character does not affect the viscoelastic properties of SG-LCPs [2, 3, 4]. Therefore, it has been inferred that they cannot be aligned using flow [2]. Our results show this conclusion to be premature, and suggest that there are numerous analogies between the rheology of SG-LCPs and BCPs.

After briefly reviewing the previous experimental and theoretical results that motivate us to examine the rheological and stress-optical behavior of SG-LCP melts, we describe the particular polymer we have chosen as a model system and the instrument and methods we use. Then we present results of dynamic stress and birefringence measurements, followed by our conclusions regarding the effects of the isotropic-nematic transition (INT) and flow history in the nematic phase on the viscoelastic and optical properties of this SG-LCP melt.

5.2 Background

The isotropic-to-nematic transition generally produces a decrease in the viscosity of a liquid crystal. This is true for low molecular weight thermotropic LCs [5], thermotropic main-chain LCPs [6], and lyotropic rigid-rod LCPs [7, 8]. This general trend

can be understood by considering the relatively simple case of solutions of rigid-rod polymers. The physical picture captured by the Doi theory of lyotropic rigid-rod LCPs is that the motion of a particular rod in an isotropic phase is severely hindered by the "cage" of neighboring, isotropically oriented rods; in the nematic phase, the tendency of the rods to align with one another produces a dilation of this "cage" and increases the rotational diffusivity [10]. At the isotropic-nematic transition, this accelerates relaxation dynamics and consequently reduces the viscosity. The general applicability of this qualitative picture is consistent with the observation that the viscosity decreases upon transition from the isotropic to the nematic state for both thermotropic and lyotropic systems, for polymeric and low molecular weight liquid crystals.

Therefore, the presence of liquid crystalline order is expected to play a significant role in determining the viscoelastic properties of SG-LCP melts as well. Indeed, this is evident in the decrease in the modulus at the isotropic to nematic transition of SG-LCP networks [11]. Surprisingly, however, corresponding effects have not been found in the previous studies of SG-LCP melts. Low shear-rate viscosity measurements by Fabre and Veyssie [2] on SG-LCPs showed the viscosity to be a continuous function of temperature, with no drop at the isotropic-nematic transition. This led them to believe that the dynamic viscoelastic behavior in the nematic state is dominated by the polymeric backbone. Similarly, Zentel and Wu [3] studied various SG-LCPs with polymethacrylate, polyacrylate and polychloroacrylate main-chain and phenyl benzoate side-groups with different spacer lengths and terminal groups and found that

the low-shear viscosity increases monotonically with decreasing temperature even at T_{ni}. From this, they concluded that ordering does *not* affect the viscoelastic properties, and, therefore, inferred that shear cannot be effective in inducing order in the sample. A recent study of the dynamic moduli of SG-LCP melts also revealed no effect of the isotropic-nematic phase transition on the relaxation dynamics of the melt [4]. However, there is evidence that, in LCPs with mesogens both in the main-chain and side-chains, liquid crystallinity *does* effect the dynamics. Pakula and Zentel [12], found that the isotropic-nematic transition of such a polymer is accompanied by a significant decrease in the dynamic moduli in oscillatory shear at a fixed frequency. The origin of these apparently contradictory results is not yet understood.

Other manifestations of liquid crystalline nature are the pretransitional phenomena that are predicted by the Landau-de Gennes theory of thermotropic LCs [13, 14], and the Doi theory for lyotropic rigid-rod LCs [10]. These phenomena arise because the closer the system is to the isotropic-nematic transition, where it will spontaneously align, the smaller the driving force required to produce a given degree of molecular orientation. This is characterized by an increase in the ratio of birefringence to the strength of an applied field. In low molecular weight liquid crystals, this effect is readily observed in their response to magnetic or electric fields [15, 16]; in SG-LCPs, pretransitional phenomena are more pronounced in response to stress fields [17, 18, 19]. This distinction may arise because accessible magnetic or electric torques can rapidly align the mesogens of a small molecule liquid crystal due to their low viscosity. These torques realign mesogens only very slowly in the much more

viscous side-group liquid-crystalline polymers. However, high values of stress are easily achieved; therefore, rheo-optical methods provide appropriate means to study pretransitional effects in LCPs. The ratio of birefringence to stress (the stress-optic ratio) has been found to increase strongly with approach to the isotropic-nematic transition of lyotropic rod-like LCPs [20] and of SG-LCP elastomers [18]. Here we characterize the behavior of the stress-optic ratio as a function of temperature and shear frequency in the isotropic phase of the present SG-LCP.

To clarify the manifestation of the liquid-crystalline nature of nematic SG-LCPs in their rheological properties, we apply dynamic viscoelastic measurements that have proven to be sensitive to phase transitions and alignment in other ordering systems, particularly block copolymers [21]. For example, in block copolymer melts the viscoelastic response at high enough frequencies arises only from local, intramolecular response and thus is essentially unchanged when the polymer melt passes through the order-disorder transition (ODT). At low frequencies, slower microstructural dynamics contribute to the viscoelastic behavior, and these can suffer a discontinuous jump at phase transitions, such as the sharp increase in the dynamic moduli of block copolymer melts at the ODT. One of the questions we address is the possibility of similar behavior in SG-LCP melts, with the distinction that the low-frequency moduli would decrease upon 'ordering', *i.e.*, passing from the isotropic to the nematic state.

Technologically, understanding the microrheology of SG-LCPs may lead to effective means to control molecular alignment using flow. The proposed applications of SG-LCPs [1] require a uniformly oriented initial state onto which information can be

written by locally heating to the isotropic state. Upon subsequent cooling into the liquid crystalline state in the absence of an aligning field, that local region becomes riddled with orientational defects and has no preferred orientation. This provides the optical contrast used for reading information. To commercialize such applications, one must produce uniformly aligned SG-LCPs. The established methods of aligning SG-LCPs are extensions of the procedures applied to small-molecule LCs. All of these involve prolonged annealing in the presence of an aligning force provided by a very strong electric field, magnetic field, or surface effect. Processing with high field strengths and long annealing times leads to high processing costs. Surface effects are limited to thin films ($\lesssim 10\mu$). Thus, advances in controlling molecular orientation to prepare monodomain materials could significantly influence the range of viable applications.

The presence of the flexible chain backbone may provide alternative means of alignment using macroscopic deformation. Recent results on SG-LCP networks suggest that a small extension of the elastomer (roughly 10%) provides a more powerful means of inducing alignment than the strongest available electric or magnetic field [18, 19]. In addition, shear flow has been found to be very effective in macroscopically ordering diblock and triblock copolymer melts [9]. If this phenomenon is general to fluids that possess intrinsically anisotropic structure, it can be expected to occur in SG-LCPs as well. Together, these observations motivate experiments to determine the effect of flow on the alignment of SG-LCPs. Should mechanical forces be successful in orienting SG-LCP melts, it will prove to be an attractive alternative to the

established methods, because it is relatively inexpensive and applicable to arbitrarily thick samples.

5.3 Experimental Section

5.3.1 Materials

The side-group liquid-crystalline polymer chosen for this research consists of a methacrylate backbone, a six methylene spacer and a phenyl benzoate mesogenic group (Figure 5.1) [22]. The terminal group on the mesogen is a methoxy moiety, which results in a material with a nematic phase over a broad temperature range Synthesis of the monomers was performed in a three step reaction. After a Williams etherification of p-HBA (hydroxybenzoic acid) with 6-chloro-hexanol, an esterification with 4-methoxyphenol was performed using the DCCI-method (dicyclocarbodiimide) [24]. Finally the resulting functional alcohol is reacted with methacrylic acid. Deuterated methacrylic acid was synthesized by Dr. Naarmann at BASF. The monomer was purified using medium pressure liquid chromatography (Kieselgel HD-SIL 60Å, 16-24μm, t-butyl-methyl-ether/cyclohexane = 1:3).

The polymer was obtained by a free radical polymerization in 2-butanol with 0.5 mol% azoisobutyronitrile (AIBN) as an initiator at 60°C [25]. Molecular weight was determined by GPC using a standard of the same side-group liquid-crystalline polymer obtained from narrow molecular weight fractions with light scattering calibration [26]. Thermal characterization was done using DSC and DTA (Mettler DSC

30). Decomposition of the material started above 590K (320°C), indicating that the material was thermally stable under the conditions of the rheo-optical experiments. This was confirmed by repeating thermal characterization of samples after the rheological experiments were completed. We study two samples with vastly different molecular weights. The high molecular weight sample (PMd6M-30) used here has a bimodal molecular weight distribution, dominated by a high molecular weight fraction (76% vol.) of $M_w \approx 3.2 \times 10^6$ g/mol ($M_w/M_n = 1.3$), with the remainder of lower molecular weight, $M_w \approx 2.5 \times 10^5$ g/mol ($M_w/M_n = 1.8$) (phase transitions: g 317K (44°C) n 390K (117°C) i, where g=glassy, n=nematic and i=isotropic) [23]. The low molecular sample (PM6M-1) has a weight average molecular weight $M_w \approx 1.15 \times 10^5$ g/mol ($M_w/M_n = 1.42$) (phase transitions: g 317K (44°C) n 383K (110°C) i, where g=glassy, n=nematic and i=isotropic).

5.3.2 Apparatus

Optical and mechanical characterization was performed using the single-axis optical rheometer described in chapter 2. Birefringence measurements were made in the 1-3 geometry where the optical axis was along the shear gradient direction (Figure 2.3, case ii) [27, 28].

The second harmonic component of $\Delta n'_{13}$ is used to determine the complex amplitude coefficient of the birefringence, $(\Delta n'_{13})^* = (\Delta n'_{13})' - i(\Delta n'_{13})''$ [30, 31].

5.3.3 Methods

All of our oscillatory shear experiments were performed using the parallel plate device shown in Figure 2.3, with a gap width of 0.65 mm and plates of 2 cm^2 area. Two types of oscillatory shear protocols were used: 1) frequency sweep experiments, where a small strain amplitude is used (<8%) to probe dynamic response as a function of frequency, and 2) prolonged, large-amplitude (roughly 40%) oscillatory shear at a fixed frequency. Frequency sweep experiments were performed at temperatures from 75 to 130°C. During the frequency sweep experiments in the isotropic phase, in which the sample is transparent, the shear stress and the birefringence in the 1,3-plane are simultaneously recorded.

For reference, the stress-optical behavior of SG-LCPs may be contrasted to that of amorphous, linear polymer melts in oscillatory shear. In amorphous polymer melts, the stress-optical rule holds over a wide range of flow conditions, so the complex amplitude of the 1,3-birefringence, $(\Delta n'_{13})^*$, equals $C\Psi_3^*$, where C is the stress-optic coefficient and Ψ_3^* is the complex amplitude of the third normal stress difference [30, 31]. For linear, amorphous melts in small amplitude oscillatory shear, $|\omega^2\Psi_3^*|$, is observed to equal $\kappa|G^*(\omega) - \frac{1}{2}G^*(2\omega)|$, where ω is the shear frequency and κ is the ratio of the third to the first normal stress differences ($\kappa = 0.74 \pm 0.07$) [27]. Therefore, we contrast the behavior of SG-LCPs in the isotropic phase to amorphous polymer melts by considering a stress-optic ratio based on 1,3-birefringence (SOR_{13}) defined as

$$SOR_{13} \equiv \frac{|\omega^2(\Delta n'_{13})^*|}{|G^*(\omega) - \frac{1}{2}G^*(2\omega)|}.$$

If this coefficient is independent of frequency at a given temperature, it suggests that the isotropic phase obeys the stress-optic rule. In that case, the temperature dependence of SOR_{13} may be contrasted to amorphous polymer melts. If SOR_{13} depends on frequency, it suggests that the SG-LCP does not obey the stress-optic rule.

In the nematic state, frequency sweeps are used only to determine the effective dynamic moduli. Frequency sweeps are repeated before and after subjecting the nematic phase to prolonged large-amplitude shear. Results are presented for the effects of prolonged shearing at 110°C for 800 cycles at a frequency of 1 rad/s and strain amplitude of 34%. To establish a reproducible initial condition for each large-amplitude shear experiment, the sample was held at a temperature well above T_{ni} (130°C) for 30 min to eliminate any effects of the flow history. The sample was then cooled to 110°C and allowed to reach thermal equilibrium (30 min). This procedure resulted in a reproducible initial state based on the transient shear stress observed during prolonged shear.

5.4 Results

The dynamic moduli G^* of the high molecular weight SG-LCP (PMd6M-30) were measured at 75, 80, 95, 110, 114, 115, 116, 117, 117.5, 118, 120, 125, and 130°C. Results at only a few temperatures are shown in Figure 5.2a-c for clarity. Upon cooling through T_{ni}, the low-frequency dynamic moduli decrease abruptly. The particular way that time-temperature superposition fails at T_{ni} is best illustrated through a Cole-

Cole plot (Figure 5.2c), which removes any ambiguity introduced by the procedure of time-temperature superposition. It shows that there are two distinct curves, one for the isotropic phase and one for the nematic phase; therefore, time-temperature superposition is appropriate within each phase. Above sufficiently high values of G' and G'', corresponding to frequencies above a critical frequency, the two curves appear to converge, suggesting that time-temperature superposition holds at high enough frequencies for both the isotropic and nematic phases. In Figures 5.2a-b it appears that the storage moduli of both phases superpose above $\omega_c' \approx 20$ rad/s and the loss moduli superpose above $\omega_c'' \approx 2$ rad/s.

The shift factors used for the master curves shown in Figures 5.2a-b are shown in Figure 5.2d. Like previous studies, we find that in the isotropic phase the shift factors show an Arrhenius temperature dependence. The apparent activation energy for flow is $E_a \approx 33$ kcal/mol. This is somewhat higher than the value reported by Zentel and Wu for a SG-LCP of the same chemical structure ($E_a = 25$ kcal/mol) [3]. In the nematic phase we observe WLF behavior with $\log a_T = \frac{-4.36(T-T_o)}{82+T-T_o}$ for a reference temperature $T_o = 383$K. Non-Arrhenius behavior of SG-LCP melt viscoelasticity in the nematic phase has not been reported previously. There appears to be a surprisingly large change in a_T from 117.5° to 115°C.

To investigate the effect of molecular weight on the viscoelastic properties of SG-LCPs near the isotropic-nematic transition, we studied the mechanical properties of PM6M-1 in the isotropic state at 114°C (at $T_{ni}+4$°C) and at 109°C (at $T_{ni}-1$°C). In this sample, with a substantially lower molecular weight than PMd6M-30, we observe

that there is no perceptible drop in the low frequency dynamic moduli (Figure 5.3a, b) upon INT. The G* data in the isotropic state and the nematic state could be shifted such that they can be superimposed at all frequencies, suggesting that time-temperature superposition is valid through INT. The Cole-Cole plot (Figure 5.3c) confirms that the isotropic and the nematic phases are not characterized by distinct curves as was the case with PMd6M-30.

Within the nematic state, the flow history can influence the flow response. Therefore, we refer to effective dynamic moduli observed in small amplitude shear. Indeed, we have confirmed that the response at small strains is linear in the isotropic and nematic phase at all temperatures used by varying the strain over a five- to ten-fold range (typically 0.5 to 8%). At the highest reduced frequencies the modulus is that characteristic of glassy behavior. Although there is the suggestion of a plateau region, it is not well defined. In monodisperse linear polymers, the plateau modulus can be obtained either by using the height of the plateau in the storage modulus or the value of the storage modulus at the minimum in the loss tangent [32]. Even though PMd6M-30 is polydisperse, we use these methods to obtain a rough estimate of the plateau modulus. Based on this approximate value of G_N^o, the entanglement molecular weight of this SG-LCP in the isotropic phase is roughly $M_e \approx 2 \times 10^5$ g/mol. Experiments on narrow molecular weight fractions will be useful to determine M_e more precisely.

The effect of prolonged, large amplitude oscillatory shear on the nematic phase is dramatic. Initially, after cooling from the transparent, isotropic state into the nematic

state, the sample becomes opaque due to strong light scattering. As long as the sample is left at rest, the sample remains opaque, indicating that the defect texture that produces the scattering coarsens slowly, if at all. After performing frequency sweep experiments with small strain amplitude, there is also no evidence of coarsening. However, during the application of many cycles of large amplitude oscillatory shear, the sample becomes translucent and eventually transparent [33]. In this state, when viewed through crossed polarizers oriented at $\pm 45°$ with respect to the flow direction, the sample appears highly birefringent. Based both on the transparency and high birefringence, this is referred to as a flow aligned state. We observe flow-induced alignment of both PMd6M-30 and PM6M-1. The results show that the effective dynamic moduli of the "aligned" sample are significantly reduced relative to the "unaligned" nematic as quenched from the isotropic state (Figure 5.4). The additional drop in G' and G'' due to flow alignment is confined to frequencies below ω_c' and ω_c'', the critical frequencies evident in the effect of the isotropic-nematic transition on G^*.

In the isotropic state, the birefringence is monitored simultaneously with the stress during dynamic mechanical experiments on PMd6M-30. The results are presented in terms of the stress-optical ratio (SOR_{13}) defined in in the previous section. At sufficiently high temperatures, *e.g.*, 130°C, SOR_{13} is independent of frequency (Figure 5.5), supporting the applicability of the stress-optical rule, as is found for amorphous polymer melts. Indeed, the value of SOR_{13} at 130°C has a magnitude ($\sim 8 \times 10^{-10}$ cm^2/dyn) typical of many other amorphous polymer melts. As the temperature is reduced toward T_{ni}, SOR_{13} increases much more strongly than is observed

for amorphous polymers, rising to $\sim 2 \times 10^{-9}$ cm^2/dyn at 125°C and $\sim 5 \times 10^{-9}$ cm^2/dyn at 120°C. Very close to T_{ni}, SOR_{13} depends on frequency; at the lowest frequencies we apply, SOR_{13} continues to increase as the system approaches the temperature at which it will spontaneously adopt nematic order. Even very near T_{ni}, SOR_{13} is independent of strain amplitude: at 117.5°C, no effect of strain on SOR_{13} is found over a six-fold range of strain.

5.5 Discussion

The isotropic-to-nematic transition produces a significant drop in the storage and loss moduli of Pmd6M-30 (Figure 5.2a-b). Analogous to what has been observed in block copolymers, this effect is manifested below critical frequencies (ω_c' and ω_c'') [21]. Following the interpretation of similar behavior in block-copolymers, this suggests that fast enough, *i.e.*, sufficiently local, dynamics are not affected by the phase change, whereas sufficiently slow dynamics are sensitive to the change in microstructure.

The basic observation that the isotropic-nematic transition results in an abrupt change in the viscoelastic properties of this SG-LCP (see Figure 5.2) may be contrasted to the results of previous studies. Colby and coworkers [4] found no change in the magnitude or shape of the dynamic moduli of their SG-LCPs at T_{ni}. Direct comparison of our results with previous steady shear viscosity measurements is not possible [34]. Nevertheless, the observation that the viscosity of previously studied SG-LCPs does not change abruptly at T_{ni} [2, 3], is qualitatively different from the sudden drop in viscosity our results would suggest: the observed drop in $|G^*|$ of the

present SG-LCP at T_{ni} tends to indicate that η_o decreases abruptly, since η_o equals the integral of the relaxation modulus. Such a drop in η_o for this SG-LCP must be confirmed by extending measurements to the terminal regime.

The reason that a discontinuous change in the viscoelastic properties is observed in PMd6M-30, but not in previous samples is intriguing. It is unlikely to be the particular monomeric structure, given that a sample having the same chemical structure was among those studied by Zentel and Wu [3]. One of the distinctive features of the present sample is that its molecular weight (main peak at 3.6×10^6 g/mol) is much higher than the materials used in previous studies (1.6×10^4 to 1.3×10^5 g/mol). To address the possibility that molecular weight may play a crucial role in the manifestation of INT on the mechanical properties, we studied SG-LCP samples with a molecular weight comparable to those used in the previous studies (PM6M-1, $M_w \approx 1.15 \times 10^5$ g/mol). Indeed, we do not observe a discontinuity in the viscoelastic properties in PM6M-1 (Figures 5.3a, b). Apparently, PM6M-1 is not entangled, as suggested by the lack of even a hint of a plateau in the storage modulus data (Figure 5.3a). This is supported by the estimate based on the PMd6M-30 data that the entanglement molecular weight is roughly $M_e \approx 2\times10^5$ g/mol. Therefore, it appears that the degree of entanglement plays a crucial role in the mechanical properties and the relaxation spectra of SG-LCPs. We believe that the nematic state may be characterized by a lower degree of entanglement, caused by the increase in lateral fluctuations of the polymer backbone due to nematic ordering. We are studying the effect of phase transition on the viscoelastic properties of nematic SG-LCPs as a function of molecular

weight, to clarify the role of entanglements on the rheology at the isotropic-nematic transition.

Another distinction between our rheological results and earlier studies is in the temperature dependence of the time-temperature shift factor a_T (Figure 5.2d). In the nematic phase we find WLF behavior, expected for a polymer melt over a similar range of temperatures above the glass transition temperature. All previous studies have reported Arrhenius behavior, even at temperatures as close to T_g as in our experiments. In the isotropic phase we do observe Arrhenius behavior with an activation energy comparable to that found in previous studies.

Entanglement behavior of SG-LCPs has not been characterized. Previous samples have been both polydisperse and, apparently, too short to be entangled. PMd6M-30 is also polydisperse, which probably explains the lack of a well defined plateau in the storage modulus; however, the molecular weight is high enough to permit estimation of the plateau modulus. It is roughly an order of magnitude smaller than that of common amorphous polymers, suggesting a correspondingly larger entanglement molecular weight. The estimated value of $M_e \approx 2\times10^5$ g/mol is reasonable in light of the effect of side groups on the entanglement molecular weight of methacrylate backbone polymers [32]. Future characterization of relatively narrow molecular weight fractions of this SG-LCP will enable precise determination of the plateau modulus of the isotropic and nematic phases.

Pretransitional phenomena arising from orientation fluctuations in the isotropic phase near T_{ni} in SG-LCPs have previously been sought in the magnetic and electric

susceptibility of these materials. In high polymer SG-LCPs (degree of polymerization above 100), little evidence of pretransitional effects has been found [17]. This has been attributed to the high viscosity of the materials. Stress-optical measurements on SG-LCP networks have proved successful in detecting the dramatic increase in the ratio of the birefringence to the stress that is expected as $T \rightarrow T_{ni}$ [18]. Here we present the first results of flow birefringence measurements on SG-LCP melts (Figure 5.5). These also show that the stress-optic ratio in the isotropic phase rises dramatically as the material is cooled toward the transition.

Further, our results suggest that very near T_{ni} the stress-optic rule fails: SOR_{13} becomes shear frequency dependent. However, we find that even in this regime, SOR_{13} remains independent of strain amplitude over the range of strain applied. A similar phenomenon has been observed in concentrated solutions of rigid-rod polymers, near the isotropic-nematic transition, where the stress-optic ratio diverges and becomes shear rate dependent [20]. In the case of rigid-rods, the shear-rate dependence could be attributed to polydispersity in the sample. This interpretation cannot be applied to SG-LCPs, as the tendency of the mesogens to align locally controls the pretransitional behavior, and the mesogens are all identical. It may be significant that when SOR_{13} becomes frequency dependent, it has a minimum in the vicinity of ω_c' and ω_c''. Concerning the behavior at $\omega < \omega_c$, the decrease of SOR_{13} with increasing frequency might be understood in terms of probing progressively more local dynamics until the molecular responses to the deformation are on a small enough scale that they are no longer sensitive to long-range order in the surroundings (*i.e.*,

$\omega \approx \omega_c$). However, this explanation leads one to expect that SOR_{13} would become independent of frequency for $\omega > \omega_c$, failing to explain the increase in SOR_{13} with ω in the high frequency regime.

In the nematic phase, we report evidence that oscillatory shear induces a preferred macroscopic alignment in this SG-LCP. This behavior is reminiscent of the flow-induced alignment of block copolymers in cylindrical or lamellar phases. Analogous to block copolymers, the effective dynamic moduli decrease as a result of flow alignment. This is consistent with the idea that one of the mechanisms of flow alignment involves the tendency of fluids that possess intrinsically anisotropic viscoelastic properties to adopt an orientation that reduces their resistance to flow [9]. In addition, like block copolymers, the critical frequencies below which the dynamic moduli are sensitive to microstructural alignment coincide with ω_c' and ω_c'' below which G' and G'' are affected by the phase transition. Again, this is consistent with the view that sufficiently rapid dynamics are insensitive to the long-range order in these fluids.

5.6 Conclusions

We have shown that side-group liquid-crystalline polymer melts *can* undergo flow alignment, contrary to the conclusions of previous studies. Molecular weight and the degree of entanglement play a key role in the manifestation of isotropic-nematic transition on the viscoelastic properties. In an entangled SG-LCP, we find that: (i) there is a discontinuous jump in the low frequency dynamic moduli at the isotropic-nematic transition, (ii) there exist critical frequencies below which the viscoelastic

properties are sensitive to the isotropic-nematic phase transition and to alignment of the nematic. The low molecular weights (*i.e., unentangled samples*) used in the previous studies appears to be the reason for the absence of any signature of INT on the mechanical properties. We have shown that, in all the SG-LCP samples we studied: (i) macroscopic alignment of the nematic can be induced by shearing, and (ii) flow-induced alignment is accompanied by a decrease in the dynamic moduli. Our rheo-optical results show that SG-LCPs exhibit pre-transitional effects in their stress optical behavior, analogous to those observed in lyotropic rigid-rod LCPs.

To clarify the dynamics and the mechanism of the flow alignment process, we use the rheo-optical methods we have developed to study the sample during and after the alignment process. Through simultaneous measurements of strain, stress and infrared dichroism, we will correlate the responses of the side groups and the backbone with the macroscopic changes that occur. This will be the subject of the next chapter.

Bibliography

[1] McArdle, C.B., ed. *Side Chain Liquid Crystal Polymers:* Chapman and Hall: New York, 1989.

[2] Fabre, P.; Veyssie, M. *Mol. Cryst. Liq. Cryst. Letters* **1987**, *4*, 99.

[3] Zentel, R.; Wu, J. *Makromol. Chem.* **1986**, *187*, 1727.

[4] Colby, R.H.; Gillmore, J.R.; Galli, G.; Laus, M.; Ober, C.K.; Hall, E., *Liq. Cryst.*, **1993**,13 (2), 233.

[5] Porter, R. S.; Johnson, J. F. in *Rheology*, Eirich, F. R., ed.; Academic Press: New York,1967; Vol. 4, Chapter 5.

[6] Wissbrun, K. F.; Griffin, A. C. *J. Polym. Sci., Polym. Phys. Ed.* **1982**, *20*, 1835.

[7] Baird, D. G. in *Liquid Crystalline Order in Polymers*, Blumstein, A., ed.; Academic Press: New York, 1978.

[8] Papkov, S. P.; Kulichikhin, V. G.; Kalmykova, V. D.; Malkin, A. Y. *J. Polym. Sci., Polym. Phys. Ed.* **1974**, *12*, 1753.

[9] Hadziioannou, G.; Mathis, A.; Skoulious, A. *Colloid & Poly. Sci.* **1979**, *257*, 15,22,136,344.

[10] Doi, M.; Edwards, S. F. *The Theory of Polymer Dynamics*; Clarendon Press: Oxford, 1988.

[11] Gleim, W.; Finkelmann, H. *Makromol. Chem.* **1987**, *188*, 1489.

[12] Pakula, T.; Zentel, R. *Makromol. Chem.* **1991**, *192*, 2401.

[13] de Gennes, P.-G. *Mol. Cryst. Liq. Cryst.* **1971**, *12*, 193.

[14] de Gennes, P.-G. *The Physics of Liquid Crystals*; Clarendon Press: Oxford, 1974.

[15] Eich, M.; Ullrich, K.; Wendorff, J. H. *Prog. Coll. Polym. Sci.* **1984**, *69*, 94.

[16] Stinson, T. W.; Lister, J. D. *Phys. Rev. Lett.* **1970**, *25*, 503.

[17] Fuhrmann, K.; Dries, T.; Fischer, E. W.; Ballauff, M. *J. Polym. Sci., Polym. Phys. Ed.* **1992**, *30*, 1199.

[18] Schätzle, J.; Kaufhold, W.; Finkelmann, H. *Makromol. Chem.* **1989**, *190*, 3209.

[19] Hammerschmidt, K.; Finkelmann, H. *Makromol. Chem.* **1989**, *190*, 1089.

[20] Mead, D.W.; Larson, R.G. *Macromolecules* **1990**, *23*, 2524.

[21] Rosedale, J.; Bates, F.S. *Macromolecules* **1990**, *23*, 2329.

[22] Portugall, M.; Ringsdorf, H.; Zentel, R. *Makromol. Chem.* **1982**, *183*, 2311.

[23] We found no evidence of a smectic phase in results of DSC, polarization microscopy or deuteron NMR spectroscopy. However, annealed SG-LCPs of the same structure but lower molecular weight and narrow molecular weight distribution have been shown to possess a weak smectic (SmA1) phase as evidenced

in SANS measurements with $T_{sn} \approx 73°C$. See Noirez, L.; Keller, P.; Cotton, J. P. *J. Phys. I France* **1992**, *2*, 915 and references therein. Even if such a phase is present in this sample, it would not effect the interpretations of our results, because the flow alignment experiments are performed close to T_{ni} and well above 73°C.

[24] Neises, B.; Steglich; W. *Angew. Chem.* **1978**, *90*, 556.

[25] Dames, B., Ph. D. Thesis, Mainz (1990).

[26] Ohm, H., Ph. D. Thesis, Mainz (1985).

[27] Kannan, R.M.; Kornfield, J.A., on "The Third-Normal Stress Difference in Entangled Melts: Quantitative Stress-Optical Measurements in Oscillatory Shear," *Rheological Acta*, in press.

[28] Johnson, S.J.; Frattini, P.L.; Fuller, G.G. *J. Coll. Int. Sci.* **1985**, *104*, 440.

[29] Janeschitz-Kriegl, H. *Polymer Melt Rheology and Flow Birefringence*; Springer: New York, 1983.

[30] Kornfield, J. A.; Fuller G. G.; Pearson D. S. *Rheol. Acta* **1990**, *29*, 105.

[31] Kornfield, J. A.; Fuller, G. G.; Pearson, D. S. *Macromolecules* **1991**, *24*, 5429.

[32] Wu, S.; *J. Polym. Sci., Polym. Phys. Ed.* **1989**, *27*, 723.

[33] Kannan, R.M.; Kornfield, J.A.; Schwenk, N.; Boeffel, C. to be submitted to *Adv. Materials.*

[34] It was not possible to capture the terminal regime in the frequency range of our instrument (10^{-2} to 10^{2} rad/s) at the temperatures employed. For the isotropic phase future experiments may overcome this limitation by using higher temperatures; for the nematic phase, we are limited to $T < T_{ni}$. In addition, previous studies [2, 3] do not indicate whether or not the limiting value of the zero-shear viscosity η_o was reached.

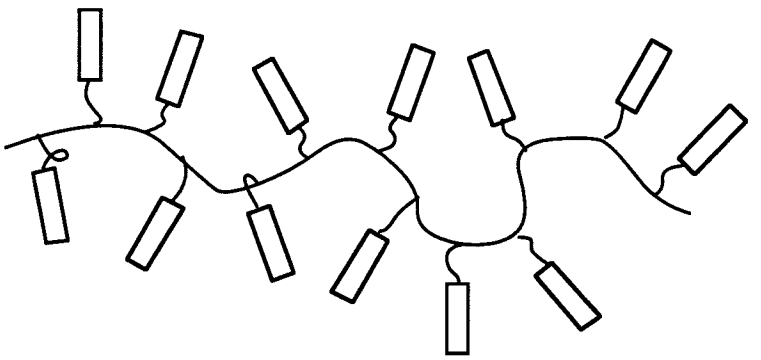

Figure 5.1a: Schematic diagram of a side-group liquid-crystalline polymer

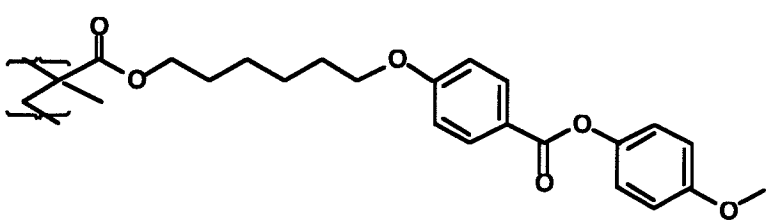

Figure 5.1b: The SG-LCP used in this study consists of a methacrylate backbone, a hexamethylene spacer, and a phenyl benzoate mesogen with a methoxy terminal group.

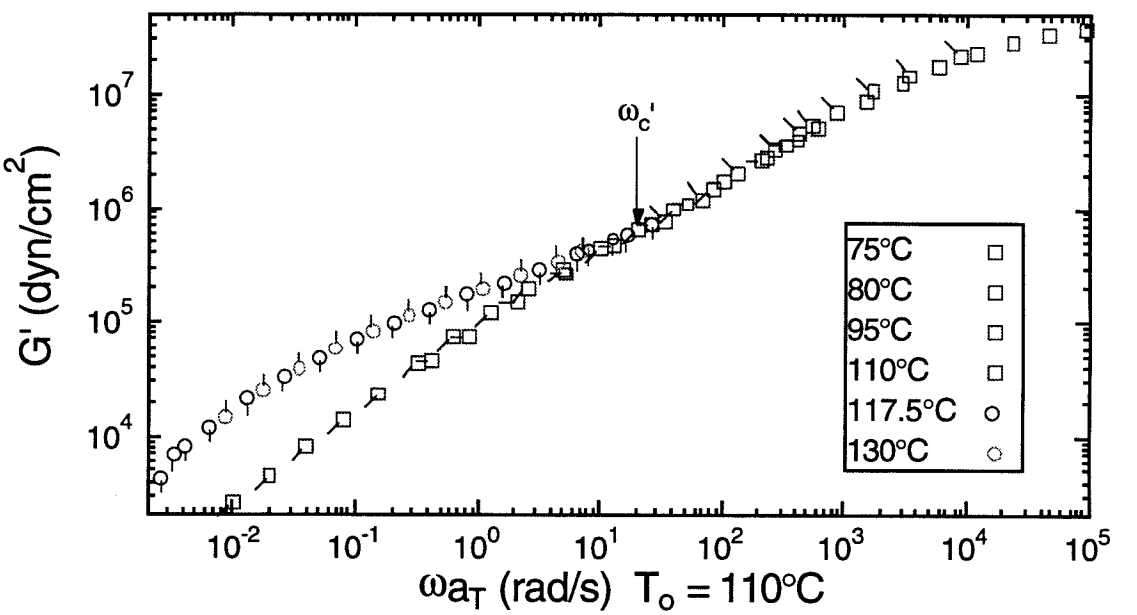

Figure 5.2a: Storage modulus master curve (G') of isotropic and unaligned nematic states of PMd6M-30.

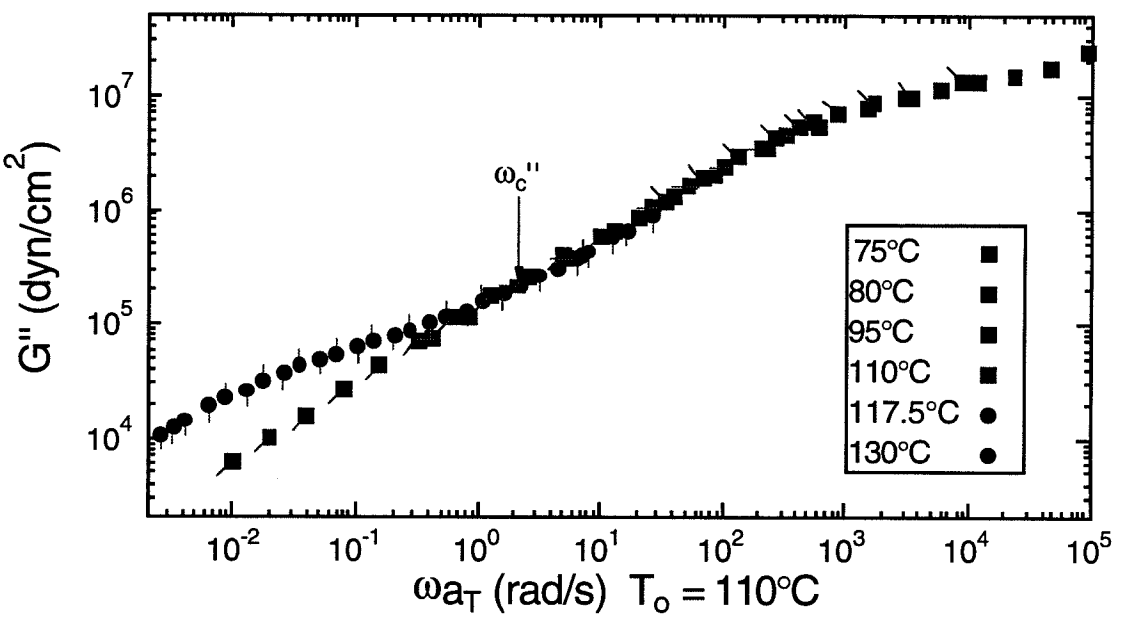

Figure 5.2b: Loss modulus master curve (G'') of isotropic and unaligned nematic states of PMd6M-30.

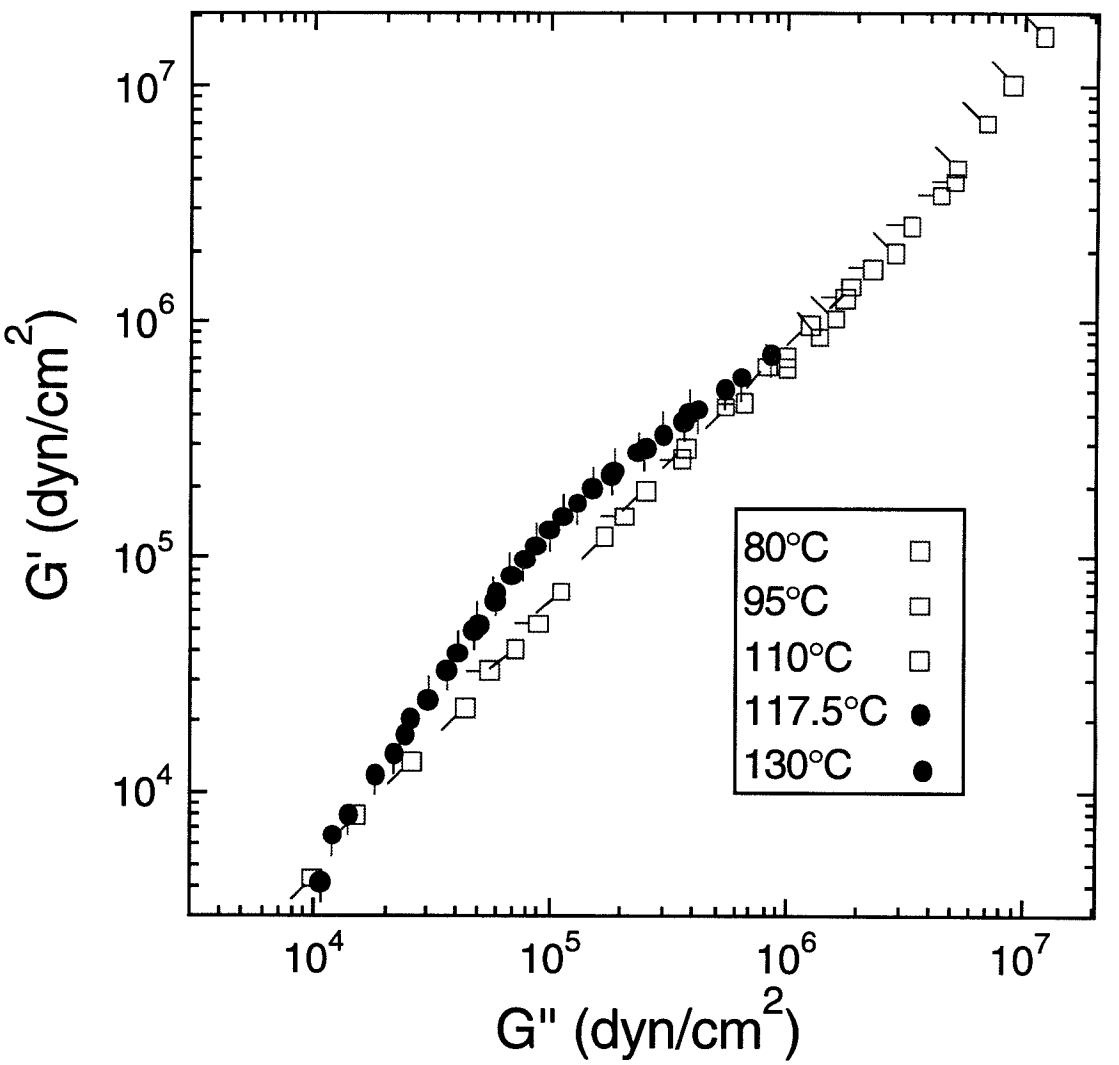

Figure 5.2c: Cole-Cole plot of the storage modulus versus the loss modulus of PMd6M-30.

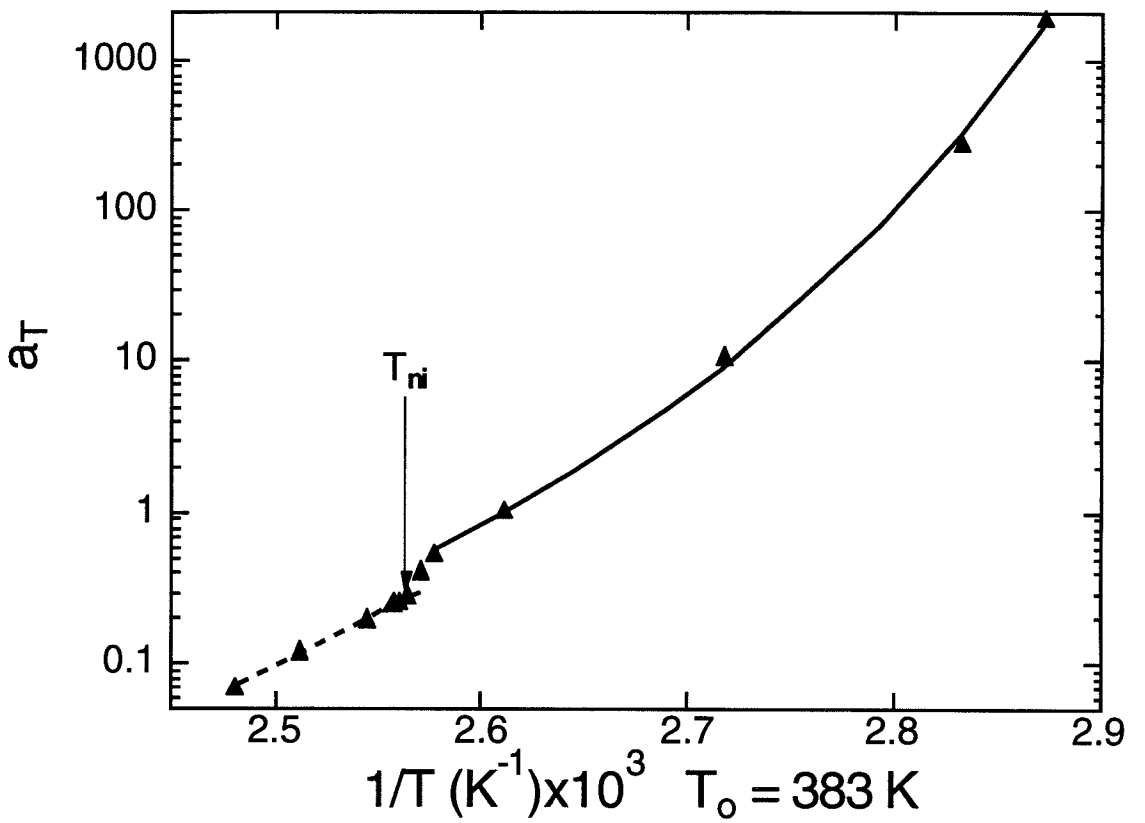

Figure 5.2d: Time-temperature shift factors (a_T) with respect to T_o = 110°C: points show the experimental values, dashed line shows Arrhenius behavior with E_a = 32.6 kcal/mol, and solid curve shows WLF behavior as described in the text.

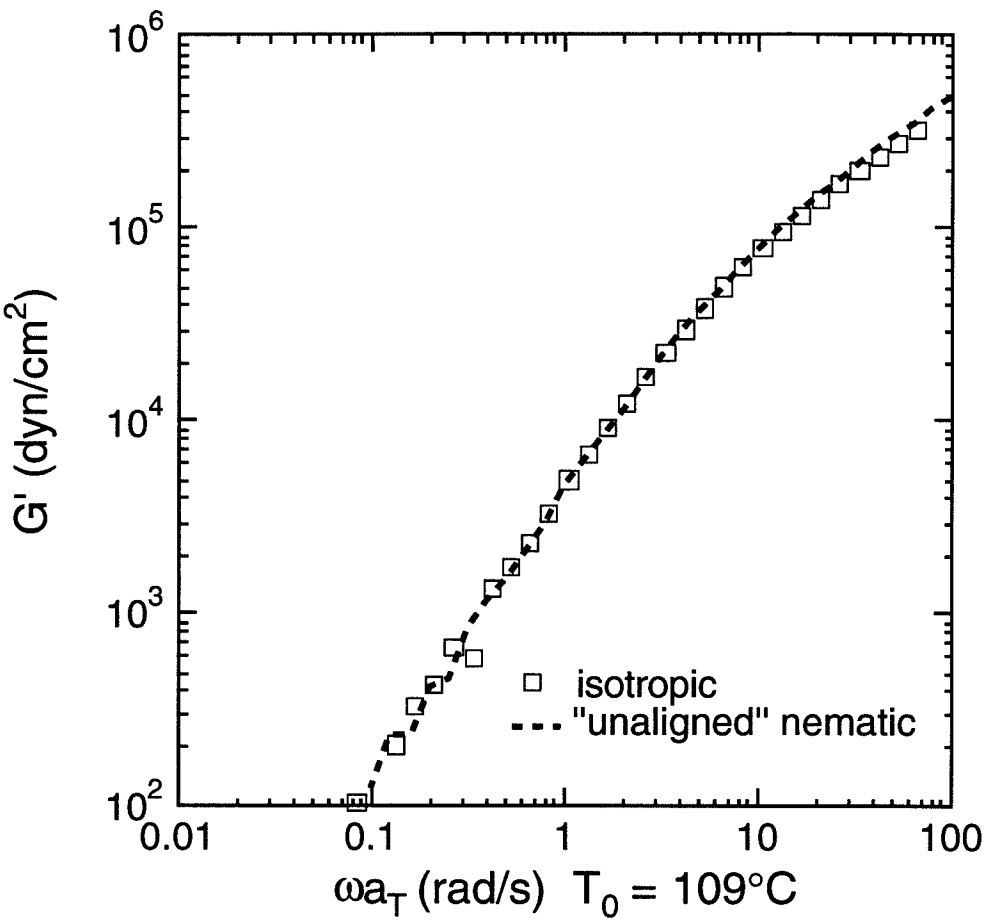

Figure 5.3a: Storage modulus master curve (G') of isotropic and unaligned nematic states of PM6M-1.

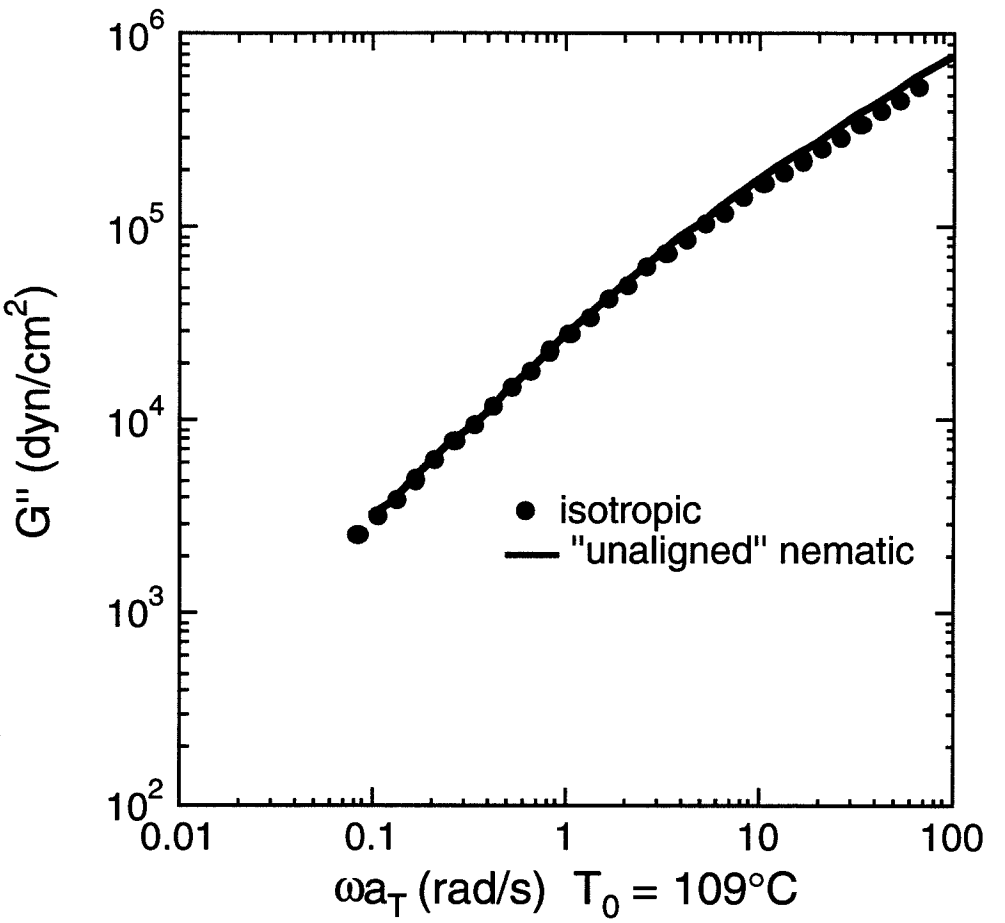

Figure 5.3b: Loss modulus master curve (G'') of isotropic and unaligned nematic states of PM6M-1.

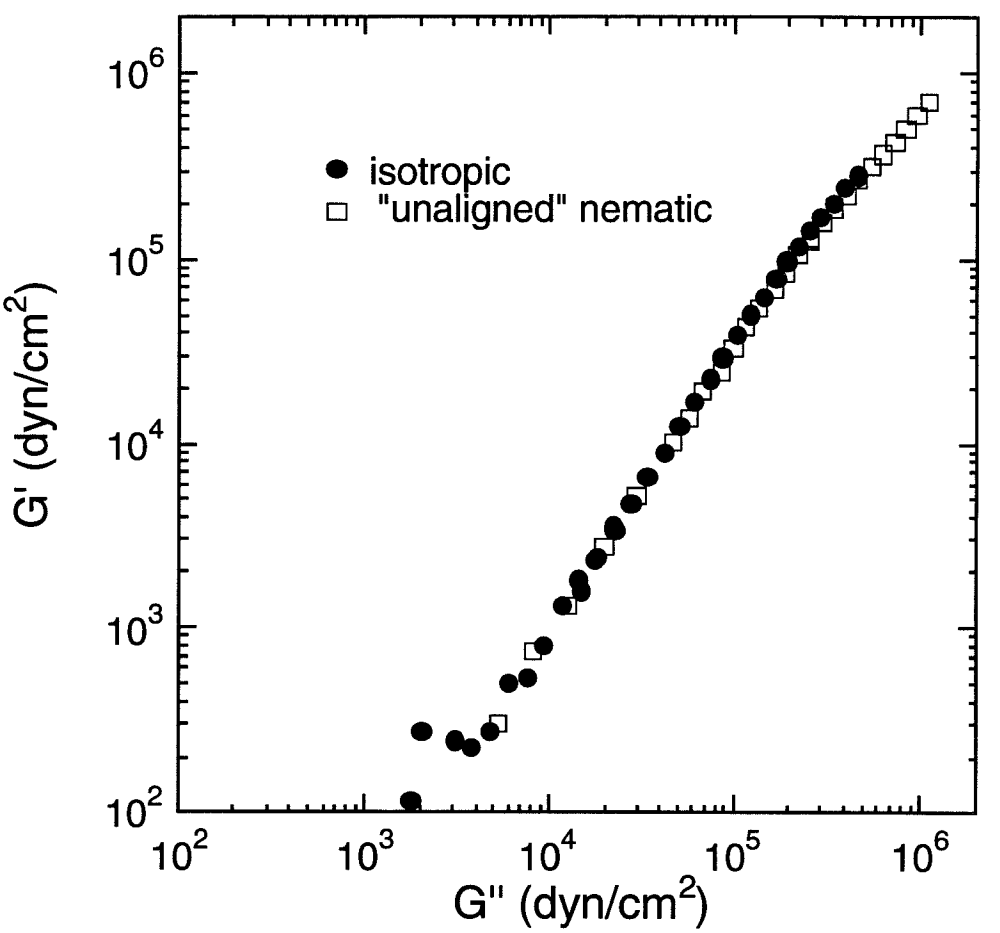

Figure 5.3c: Cole-Cole plot of the storage modulus versus the loss modulus of PM6M-1.

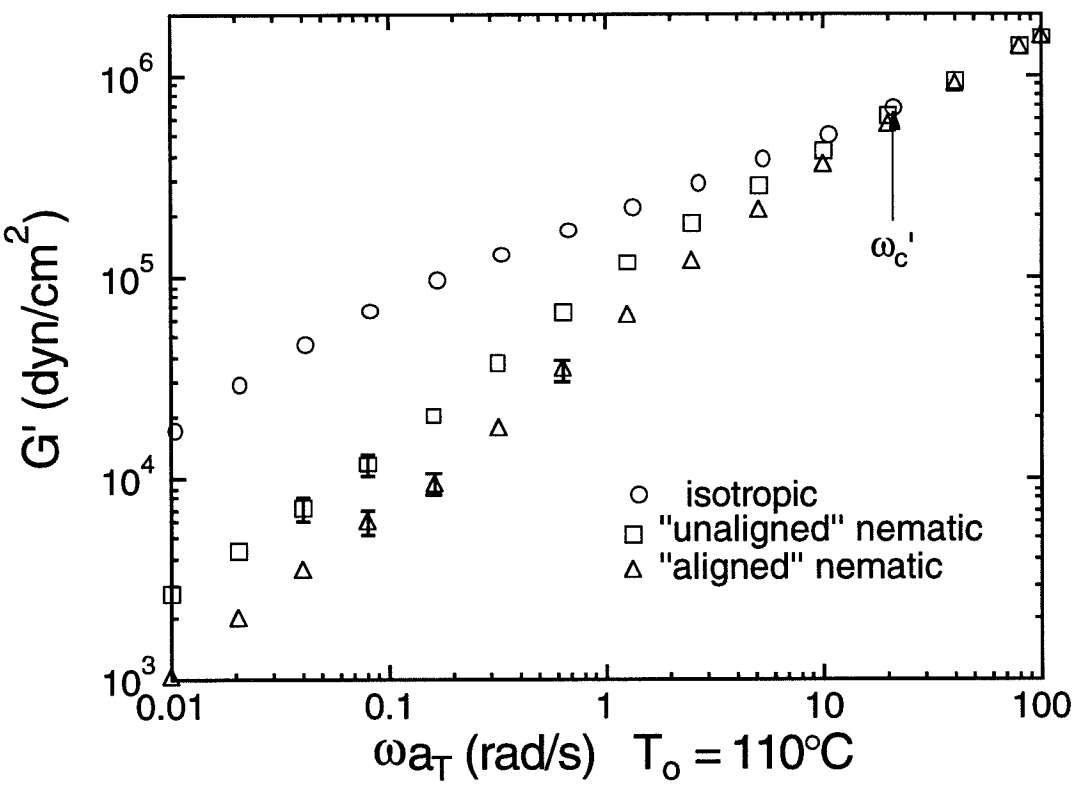

Figure 5.4a: Effect of flow alignment on the storage modulus of PMd6M-30. The modulus of the isotropic phase, and of the nematic phase at 110°C before and after large amplitude shearing. The average of the values obtained in two separate series of experiments is shown by each symbol; where the difference between these values is greater than the symbol size, a vertical bar spans between them.

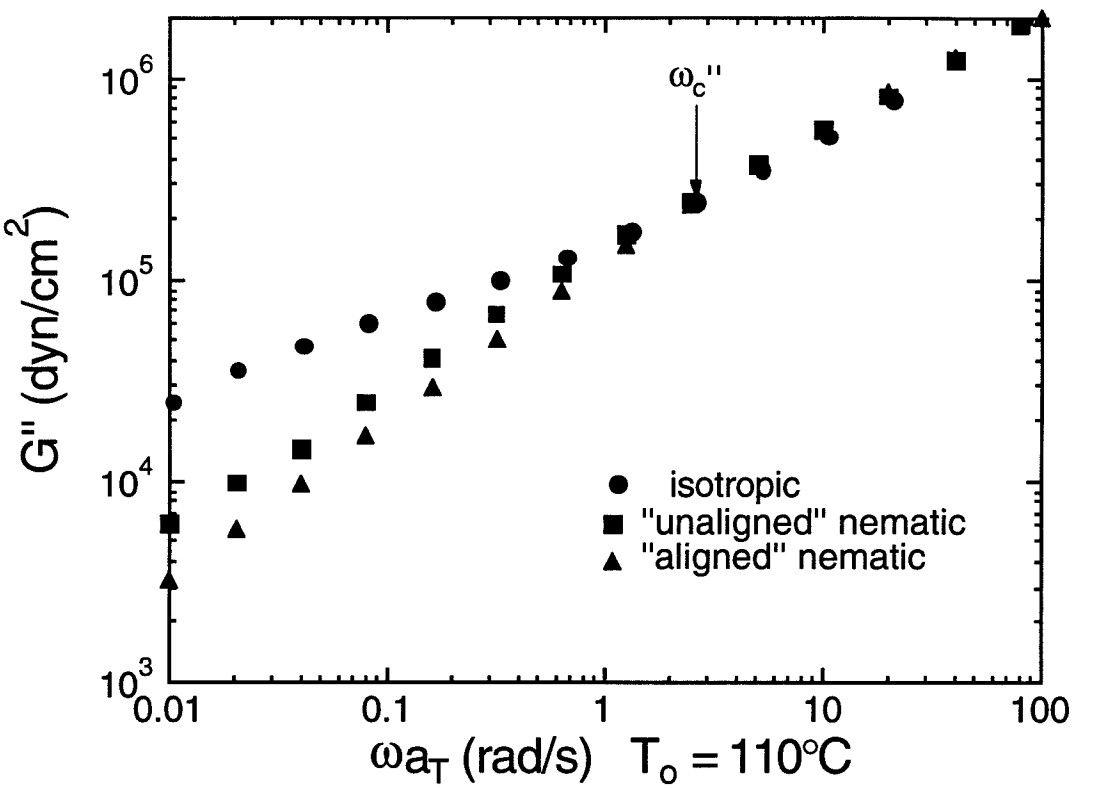

Figure 5.4b: Effect of flow alignment on the loss modulus of PMd6M-30. The modulus of the isotropic phase, and of the nematic phase at 110°C before and after large amplitude shearing. The average of the values obtained in two separate series of experiments is shown by each symbol; where the difference between these values is greater than the symbol size, a vertical bar spans between them.

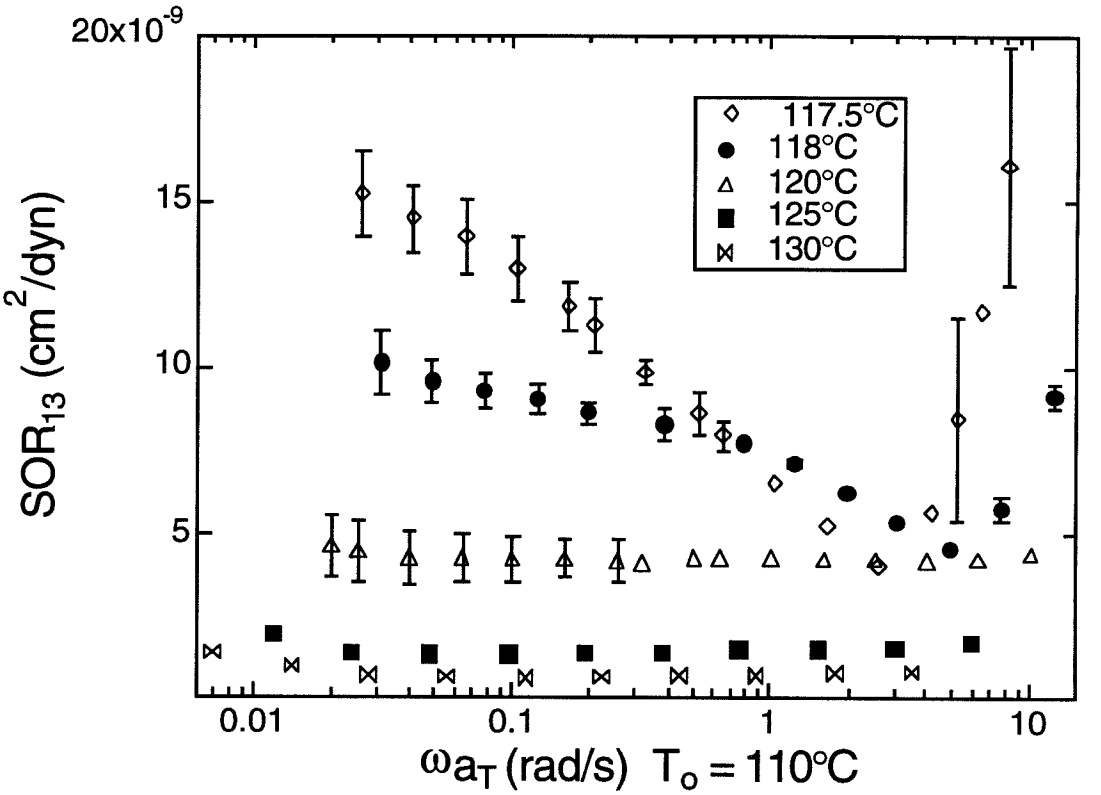

Figure 5.5: Stress-optic ratio in the isotropic phase near the isotropic-nematic transition for PMd6M-30. The results of two sets of measurements are shown. The average of the two values at each temperature and frequency is shown by a symbol; where the difference between the individual values is greater than the symbol size, a vertical bar spans between them.

Chapter 6

Dynamics of Flow-Induced Alignment in SG-LCPs

6.1 Introduction

We showed in the previous chapter that oscillatory shear is effective in inducing macroscopic alignment in nematic SG-LCP melts [1, 2]. The shear-induced alignment is evidenced by an increase in transmittance and a drop in the low frequency dynamic moduli. In addition, the sample becomes highly birefringent. Upon cessation of shear, some relaxation of the alignment is manifested by a decrease in the transmittance. The dynamics of the alignment process appears to be relatively complex and qualitatively different from that in analogous systems such as main chain LCPs [2]. Previous results suggest that it arises from a combination of the dynamics of the backbone, director field and the coupling between the two arising due to the spacer. The nature of the alignment process during large amplitude oscillatory shearing of SG-LCPs is the subject of thischapter. We focus on two aspects that are central to understanding the alignment process : (1) The origin of the drop in the modulus upon flow-induced alignment [1], and (2) The origin of the strain hardening behavior [2], and how it may relate to the mechanism of flow-induced alignment. In relation to the mechanism of flow-induced alignment of SG-LCPs, previous studies of SG-LCPs, and of liquid crystals in general, suggest two possibilities. One arises from the coupling between backbone and the mesogen orientation, and the other from the anisotropic flow properties of liquid crystals.

The relative orientation of the polymer backbone and the mesogen depends on the competition between the tendency toward anisotropic ordering (due to the mesogens) and conformational disordering (due to the backbone). The balance between the en-

thalpic and entropic contributions is very sensitive to the flexibility of the backbone, the spacer and the chemical constitution of the mesogen [3]. NMR studies on magnetically aligned SG-LCP samples (methacrylate backbone, phenyl benzoate mesogen, hexa-methylene spacer) analogous to the present SG-LCP show that, on a molecular scale, the relative orientation of the backbone and the mesogen is perpendicular on average, with the backbone maintaining a nearly random configuration in the nematic state [4, 5]. The same relative orientation is observed even in nearly identical SG-LCP networks under extensional deformation [7]. In our work, we use a sample with the same chemical constitution, but higher molecular weight. Therefore, we expect that perpendicular orientation will be preferred on a local scale. During shear alignment, the backbone conformation will be biased along the extensional axis ($\gamma_0 \leq 100\%$). In analogy to SG-LCP networks [8, 6, 7], this may drive the director field to align perpendicular to the extensional axis of the shear flow. This suggests a mechanism of flow-induced alignment that originates with the distortion of the backbone and propagates out to the director due to the correlation between the mesogen and backbone orientation.

An alternate mechanism for flow-induced alignment may be that shear macroscopically aligns the director along the direction that minimizes the resistance to flow. Indeed, liquid crystalline solutions exhibit anisotropic viscosity coefficients referred to as Miesowicz viscosities [9]. The ratio of the anisotropic viscosity coefficients can vary from 4 for small molecule LCs [10] to about 100 for lyotropic rod-like LCP solutions [11]. Such an anisotropy in viscoelastic properties could also be the origin

for the drop in the modulus of SG-LCPs upon shear-induced alignment. We examine this notion by measuring the mechanical properties of the SG-LCP samples where the director is aligned along a chosen direction by annealing in a strong magnetic field. These results also provide clues regarding the role of defects in determining the mechanical properties, since these are minimized in aligned samples. To our knowledge, these are the first measurements of the dynamic mechanical properties of aligned SG-LCP melts.

Another possible explanation for the drop in the dynamic moduli during large-amplitude shearing [2] may be melt fracture. Melt fracture may also be responsible for the slow recovery of the linear dynamic modulus after the cessation of large amplitude shearing [1]. Under large amplitude oscillatory shear, decrease in the shear stress is observed even in homopolymer melts [12, 13, 14]. This has been attributed to shear instabilities. In addition to producing a significant drop in the stress, "melt fracture" can be manifested by stress oscillation becoming non-sinusoidal at longer times. After prolonged shear, the sample appears severely cracked and crumbled [14]. Melt fracture has been shown to occur in homopolymers at strain levels comparable to those used in our study [14]. In a lamellar diblock copolymer, the decrease in stress amplitude during alignment at large amplitude oscillatory shear, and its subsequent recovery to the initial values have been attributed to melt fracture [15]. In light of these findings, we investigate the possibility that melt fracture may be occurring even in the present SG-LCP sample causing the drop in the modulus upon alignment observed during large amplitude shearing.

The following sections outline our experiments aimed at addressing the questions raised above. We will present the first results on the mechanical properties of magnetically aligned SG-LCPs, and measurements of the dynamic moduli and transmittance during and after the alignment process. We will discuss the implications of our results regarding the mechanism of shear-induced alignment in SG-LCP melts.

6.2 Experimental Section

6.2.1 Materials

We use two samples for investigating the alignment process. The first sample, designated as PMd6M-30, is deuterium labeled in the backbone and is used for measurements of IR transmittance and IR dichroism during alignment. It has a molecular weight of $M_w \approx 3.0 \times 10^6$ g/mol with $M_w/M_n = 5.0$. The second sample, designated as PM6M-11, is used for both shear and magnetic field-induced alignment experiments. It has a molecular weight of $M_w \approx 1.14 \times 10^6$ g/mol with $M_w/M_n = 1.54$. This sample is deuterium labeled in the backbone and will be referred to as PMd6M-30. The synthesis and the characterization of the sample were described in the previous chapter [1, 16].

6.2.2 Apparatus

The shear alignment and the mechanical characterization of the sample were performed using a Rheometrics Solids Analyzer (RSA II). All the rheological experiments

were conducted under oscillatory shear, in the shear sandwich geometry (Figure 2.3). The sample dimensions were 15.95 mm $\times$ 12.6 mm $\times$ 0.35 mm, offering a optical path length of 0.7 mm. Polished CaF_2 windows were used to permit transmittance measurements. For transmittance measurements, we use a visible (HeNe) laser source ($\lambda = 633$ nm) and IR diode laser ($\lambda = 633$ nm), and collect the transmitted light using a lens and monitor the intensity using a photodetector. The use of CaF_2 windows also allowed us to view the sample through crossed polarizers during the alignment process, using a long distance microscope (magnification 25X).

The details of the apparatus used for measuring the infrared (IR) dichroism during the alignment process is described in Chapter 2 [17].

6.2.3 Methods

To erase any effect of previous history the sample is heated well into the isotropic state (130°C) and equilibrated at that temperature for 20 minutes. The sample is then cooled to the desired temperature with a 20 minute equilibration time. Two types of oscillatory shear protocols were used: (1) frequency sweep measurements, where a small strain ($\leq 3\%$) is used to characterize the dynamic response and (2) prolonged, large amplitude oscillatory shear at a chosen frequency. All our measurements are made in the oscillatory shear mode. We study the response of the sample to a sinusoidal strain: $\gamma = \gamma_o \sin \omega t$, where γ_o is the magnitude of strain. The stress in the linear viscoelastic regime is described by $\sigma = \gamma_o\{G' \sin \omega t + G'' \cos \omega t\}$. The moduli measured at small strains are verified to be independent of strain. However,

the dynamic moduli change during alignment, and hence we will refer to them as effective moduli (G'_{eff} and G''_{eff}).

During oscillatory shear, the dichroism in the 1,3-plane $\Delta n''_{13}$ has a displacement component and a complex amplitude, analogous to the behavior of N_3:

$$\Delta n''_{13} = (\gamma_o)^2[\omega^2\psi^d_{3,D} + \omega^2\psi'_{3,D}\sin\omega t + \omega^2\psi''_{3,D}\cos\omega t], \tag{6.1}$$

where $\psi^d_{3,D}$ and $\psi^*_{3,D} = \psi'_{3,D} - i\psi''_{3,D}$ are the displacement coefficient and complex amplitude of the 1,3-dichroism. The evolution of $\psi^d_{3,D}$ for the during and after the alignment process will be monitored.

To study the mechanical properties of the magnetically aligned sample, we annealed the samples in a 7 Tesla superconducting magnet, prior to dynamic mechanical measurements. The magnetic field aligns the mesogens along the direction of the field due to the anisotropic diamagnetic susceptibility of the mesogens compared to the backbone. The sample was loaded in the flow cell (Figure 2.3), and placed in the magnetic field so that the mesogens can be aligned along a chosen direction. The sample temperature of the flow cell while in the magnet was controlled to within $\pm 1°C$ (Omega^{TM} controller CN 2011 with Kapton^{TM} flexible heaters and a Type T thermocouple). Once mounted in the magnet, the sample is heated to 125°C (isotropic) at a rate of 1°C/min and held at 125°C for 20 minutes so that any previous history is erased. It is then cooled to 110°C (nematic state) at a rate of 0.15°C/min, and held at 110°C for 12 hours. After this long annealing period, the sample is brought to room temperature (to the glassy state) at 0.5°C/min. In contrast to an opaque, un-

aligned nematic glass, after this procedure the sample has considerable transmittance (typically 30% of that in the isotropic state), indicating that the magnetic field was effective in aligning the sample, but did not produce a monodomain sample. However, there must be a significant enhancement in alignment and a decrease in the number of defects, for such a thick sample to appear translucent (0.7 mm). The flow cell is then loaded into the RSA II and tested at temperatures $T_g \leq T \leq 110°C$ with small strain frequency sweeps.

6.3 Results

6.3.1 Alignment Experiments on PMd6M-30

The effect of shear on the transmittance and effective dynamic modulus is very dramatic and depends strongly on the strain amplitude and frequency. The light transmittance is referenced to that of the isotropic phase ($T = \frac{I}{I_{iso}}$), in which there are no orientational defects to scatter light. Upon transition into the nematic phase, the transmittance drops effectively to zero due to the formation of domain structures with a macroscopically isotropic director distribution. If left at rest in the absence of an applied field, no appreciable increase in transmittance is observed even after a period of hours.

When an unaligned, opaque nematic sample is subjected to shear, we observe a measurable increase in the transmitted intensity after the first cycle of shearing at 1 r/s at 110°C. The monotonic increase in transmittance with continued shearing is

shown in Figure 6.1a. Experiments were repeated with different strain amplitudes. For 34% and 64% strain amplitude the IR transmittance increases to that of the isotropic state after 600s and 100s, respectively. After 1200s the sample appears clear to the eye and is found to be highly birefringent when viewed through crossed polarizers.

Upon cessation of shear, part of the transparency gained during the shear-induced orientation process is lost, finally remaining constant at some intermediate value (Figure 6.1b). After stoppage of shearing at 34% strain, the IR transmittance reduces to about 17% in 2 hours. As the strain amplitude is increased to 64%, the relaxation of IR transmittance is much slower and reaches about 60% in 6 hours.

During shear, the magnitude of the effective dynamic modulus ($|G^*| = \sigma/\gamma$) decreases by about 5-15%, where σ is the shear stress and γ is the strain. The dynamics of the change in fluid microstructure manifested in $|G^*(t)|$ and the ultimate stationary state depend on the strain amplitude, as is evident from the difference in behavior for the 34% and 64% cases shown in Figure 6.2a. The modulus appears to increase with increase in strain. $|G^*(t)|$ at 64% is higher than that at 34%. The effect of strain on the modulus seems to be more pronounced upon alignment (Figure 6.2a). The backbone response was also observed during flow alignment using 34% strain. The IR dichroism in the 1,3-plane is an even function of the shear rate. During oscillatory shear at frequency ω, the relevant components are the steady displacement $(0 \cdot \omega)$ and second harmonic $(2 \cdot \omega)$ coefficients [2]. The magnitude of the second harmonic ($|D^*|$) and the displacement ($|D^d|$) coefficients of the dichroism reflect the strength

of the distortion of the chains by the oscillatory shear. During the first 100s, both of these quantities decrease (Figure 6.2b). However, after 100s, both of them increase with time. Within the next 400s, they increase significantly and reach a steady value.

6.3.2 Alignment Experiments on PM6M-11

To compare shear-induced alignment with magnetic field induced alignment and to observe the stability of shear-induced alignment, we use PM6M-11. Before shear, the sample is a polydomain nematic and appears turbid due to the large density of defects. Within the first cycle of shear at 0.1 r/s, 100% strain at 110°C, the sample becomes translucent (Figure 6.3a). The transmittance at 633 nm reaches a value more than 80% within the first five minutes. Upon prolonged shearing the transmittance does not change appreciably. During shear, the effective dynamic moduli decrease (Figure 6.3b). The decrease in the dynamic moduli upon shear alignment is nearly 10% and the decrease is a more gradual process than the increase of the transmittance. The dynamic moduli measured at small strains before and after the alignment process are indicated by arrows in the vertical axis. There is a significant *increase* in the moduli with increase in strain, indicative of strain hardening. As the strain is varied from 3% to 100%, G' increases by nearly 73% while G'' increases by 16%. Upon shear-induced alignment, the strain hardening is even more dramatic in the case of G'. As the strain is varied from 3% to 100%, G' increases by nearly 100% while G'' increases by 16%.

Over three decades of frequency (0.1 rad/s to 100 rad/s) at 110°C, we find that

the modulus is independent of strain amplitude, when the strain is varied from 0.06% to 3% (linear regime).

Upon cessation of large amplitude shearing, there is a decrease in the transmittance of the sample (Figure 6.4a). It decreases to about 73% within the first few minutes, followed by a more gradual decrease. When the sample is held at 110°C for a period of 10 hours, the transmittance decreases slowly and ultimately reaches nearly 40%. After shear alignment at high strains, we also perform frequency sweeps on the sample at small strains, to characterize the stability of alignment and the effect of recovery on the mechanical properties. Above a critical frequency, G' and G'' are insensitive to the state of alignment ($\omega_c' \approx 40$ rad/s, $\omega_c'' \approx 2$ rad/s). Below these critical frequencies, when measured within minutes after alignment, there is a significant drop in the low frequency moduli due to alignment (Figure 6.5). However, after several hours at 110°C, the moduli recover towards the values measured in the unaligned nematic state.

Based on the shear-induced alignment experiments conducted at various frequencies and durations of shear, we found that, qualitatively, the degree and stability of orientation tends to increase with higher strain amplitude, longer duration and lower frequency [2].

Using the protocol outlined in the previous section, we aligned the mesogens of the present SG-LCP in a magnet. Two directions of alignment have been investigated: along the shear direction and along the vorticity direction. A comparison of shear alignment and magnetic alignment (Figure 6.4) on the small strain dynamic moduli

at 110°C over four decades of frequency (0.01 - 100 rad/s) reveals the following features : (1) Above the critical frequencies (ω_c' and ω_c'') the moduli are insensitive to macroscopic (magnetic or shear-induced) alignment; (2) Throughout the experimental frequency range, the dynamic moduli of the unaligned sample, and both of the magnetically aligned sample are nearly the same.

6.4 Discussion

6.4.1 Magnetic Alignment

A comparison of the dynamic moduli of the magnetically aligned and shear-aligned samples provides important clues regarding the factors that influence the alignment process. After annealing in a magnetic field, the director is predominantly oriented along the direction of the magnetic field, with the backbone slightly biased to orient perpendicular to the director [4]. In the frequency range used in this study, the dynamic moduli of the magnetically aligned samples, measured at small strains, are insensitive to magnetic field induced alignment. This suggests the following three conclusions:

- A particular macroscopic director orientation does not minimize the modulus. This discounts an alignment mechanism based on anisotropy in the viscoelastic properties;

- Elimination of a significant amount of defects alone cannot explain the drop in the low frequency modulus observed upon shear-induced alignment;

- At small strains, the distortion of the macroscopic director field does not contribute significantly to the moduli. On the other hand, the moduli may be dominated by the distortion of the polymer backbone (even below ω_c'). This is reasonable, because at the length scale of the backbone, the director orientation is uniform, irrespective of the state of alignment.

6.4.2 Strain Hardening

The present SG-LCP exhibits strain hardening behavior when the strain is increased beyond the linear regime. Most flexible chain homopolymers are 'strain softening' in the nonlinear viscoelastic regime (the modulus decreases with increase in strain), and the non-linearity becomes significant when $\gamma_o \geq 100\%$. Strain hardening is usually observed only during extension and at high strains [18, 19], associated with chain branching, a high degree of entanglement or strain induced crystallization. It has also been observed recently in thermotropic LCP solutions in extensional flow [20], and attributed to the presence of residual crystallinity, polydispersity or contributions from the distortion of the director field. None of these applies to the present SG-LCP.

In the present SG-LCP, strain hardening may arise from the anamolous strain dependence of the distortion of the backbone, distortion of the director field, or the coupling between the two. Since the flexible chain characteristics of the SG-LCP would suggest strain softening, and the distortion of the director field does not contribute significantly to the stress in the frequency range of interest, we focus on the role of the coupling between the backbone and the mesogens as a possible source

of strain hardening.

The domain size (*i.e.*, the length scale over which the director orientation is uniform) in an unaligned nematic is typically of the order of microns and the radius of gyration of the SG-LCP is nearly 200 Å[21], there are many polymer chains within a single domain. Based on a model suggested by Götz et al. [22] for a static sample in the nematic, the chain conformation within a domain can be described by a director $\hat{n}_B$ oriented at an angle ϕ_B with respect to a reference axis, with the local nematic field described by a director $\hat{n}$ oriented at an angle ϕ. On a molecular scale, the backbone and the mesogens tend to be perpendicular to each other ($\phi - \phi_B \approx 0$) (Figure 6.6a). The mesogen order parameter (S) within a domain will be denoted as S_o.

It is useful to consider how the nearly random configuration of the backbone is directly affected by strain, and how that couples to the local director field through the spacer. Under shear, the polymer backbone conformation is likely to be biased along the extensional axis of shear. In fact, IR dichroism of the backbone labeled PMd6M-30 (Figure 6.2b) over a period of one cycle at 1 r/s, suggests that the polymer backbone responds strongly to shear. During prolonged shear, the backbone responds more and more strongly, as is evident from the significant increase in the magnitude and the dc component of the dynamic IR dichroism. Therefore, shear changes the aspect ratio of the ellipsoid of gyration. This can be viewed as changing the relative orientation of the directors $\hat{n}_B$ and $\hat{n}$. The mesogens are subjected to two competing influences: they would prefer to be perpendicular to the backbone, but are also constrained

by the director orientation within a domain. This competition would result in the mesogen choosing an intermediate orientation, perhaps causing a reduction in the order parameter ($S \leq S_o$) (Figure 6.6b). This can be thought to produce a stress (σ_C), arising from the energy penalty for changing the mesogen orientation from that dictated by the local director. Therefore, in a simplistic sense, the stress response can be described by $\sigma_T = \sigma_B + \sigma_C$, where σ_T is the observed shear stress, σ_B is the contribution from the distortion of the polymer backbone and σ_C is the contribution due to the coupling between the mesogen and the backbone.

We believe that at small strains, the backbone distortion from the initial configuration is so small ($\phi - \phi_B \approx 0$) that the contribution arising from the distortion of the local director field σ_C is negligible relative to σ_B. Since σ_B is expected to scale linearly with strain, we observe linear behavior. If this picture is correct, then the observed strain hardening would indicate that σ_C vary nonlinearly with strain (even at $\gamma_0 \approx 10\%$). As the strain is increased beyond the linear regime, the backbone conformation is distorted appreciably, causing a significant change in the relative orientation between $\hat{n_B}$ and $\hat{n}$. (*i.e.*, $\phi - \phi_B$ is appreciable) (Figure 6.6b). This produces a measurable contribution from σ_C to σ_T, manifested in the strain hardening behavior.

6.4.3 Melt Fracture During Shear?

Shear-induced alignment is accompanied by a significant drop in the low frequency dynamic moduli measured at small strains which recovers slowly (Figure 6.3). Such

a drop in modulus is *not* observed in magnetically aligned samples. The decrease in the modulus of the flow-aligned sample may reflect a change in the SG-LCP conformation (*e.g.*, backbone orientation or relative orientation of mesogens relative to the backbone), or it may simply reflect large scale changes in fluid structure that occur in some polymer melts under large amplitude oscillatory shear (*e.g.*, "melt fracture").

To address the possibility that melt fracture may be occurring in our samples, we performed experiments at different strains, frequencies and temperature and observed the sample before, during and after shear alignment. (1) After alignment, if there were melt fracture, it would be evident in the moduli measured at all the frequencies. However, we observe a drop in the modulus, only below a critical frequency ($\omega_c' \approx$ 40 rad/s, $\omega_c'' \approx$ 2 rad/s), which coincides with the frequency where the effect of microstructure on the dynamic moduli are evident [1]. (2) Under otherwise identical conditions, flow-alignment at higher strain produces a higher modulus during shear. If melt fracture were indeed occurring, it should be increasingly evident at higher strains, resulting in a larger drop in the modulus during alignment at higher strain. (3) During alignment at high strains, the decrease in the magnitude of stress is only about 10%. This is in contrast with the observations of Chen et al. [14], who observed an order of magnitude drop in stress during shear fracture in polystyrene at comparable strains. When we probe the aligned sample at small strains, we observe a 50% drop in the stress compared to the unaligned state, at the same frequency (Figure 6.2b). Suppose the sample has suffered melt fracture, there is no reason to expect that it will be more pronounced at smaller strains. (4) The strain and stress are sinusoidal throughout the

alignment process. This is in contrast to the results of Hatzikiriakos and Dealy [12] who observed asymmetric, non-sinusoidal waveforms during melt fracture. (5) During shear, we view the sample between crossed polarizers using a long working distance microscope (25X). We do not see any visible evidence of edge fracture, gross melt fracture, or wall slip of the sample during the alignment process. The sample appears nearly homogeneous. (6) In most polymeric materials, melt fracture is observed at large strains, at high stress and frequencies near the glassy regime. In our experiments, we observe a drop in the modulus upon alignment at strains as low as 34%, at stresses as low as $\sim 10^4$ dyn/cm^2, at conditions near the terminal regime.

Based on these observations, it appears that 'melt fracture', at least as it is referred to in the traditional sense, is not taking place in our experiments. Therefore, we believe that the drop in the modulus upon shear alignment reflects some change in SG-LCP conformation induced by the shear.

6.4.4 On the Mechanism of Shear-induced Alignment

This domain size in a nematic side-group polymer grows very slowly if at all in a sample left at rest, in the absence of an aligning field. The increase in transmittance during shear is reminiscent of that observed during the director orientation process in small molecule liquid crystals under the influence of an applied field or surface effect. During such an orientation process, a polydomain sample, turbid due to the large density of defects, becomes transparent due to a decrease in the density of the defects, thus enlarging the average domain size. The elimination of turbidity at

$\lambda = 4.53\mu$m during shear (Figure 6.1a) indicates that domains of a few microns in size are completely transformed upon shearing to larger, uniformly-oriented domains. Regarding the mechanism for flow-induced alignment, we believe that a mechanism similar to the one that causes strain hardening may also cause alignment during prolonged shear. During shear, the backbone is biased along the extensional axis of the flow. Prolonged shearing continuously biases local director orientation to be perpendicular to the extension direction, perhaps forcing the mesogen orientation to propagate to macroscopic dimensions.

Upon cessation of shear, part of the transparency gained during the shear-induced orientation process is lost, finally remaining constant at some intermediate value (Figure 6.1b). This value depends on the amplitude of the applied strain indicating that the stability of the orientation gained during shear is a function of the shear history of the sample. This memory effect is in contrast to the domain orientation obtained in a low molecular weight SG-LCP fully aligned by an external magnetic field [23], where the alignment was stable even after the field had been removed. At the end of prolonged shear, the SG-LCP is left in a distorted state. This may involve a distorted backbone conformation, unfavorable relative orientation of the backbone and the director field, and/or defects being forced near each other by shear. At 110°C on a time scale of sixty seconds, or one cycle at 0.1 rad/s, entanglements are largely relaxed, and Rouse modes and more local segmental rearrangements are certainly relaxed. On the other hand, the terminal relaxation of the chains is not complete, and larger scale structures, such as domains, have much slower dynamics

and, consequently, can be significantly perturbed by the flow.

The macromolecular relaxation should be the most rapid process, with a similar relaxation time in the two cases. Based on the dynamic moduli of this sample, the molecular relaxation is expected to be complete on a time scale of about 1000s at 100°C [1]. This suggests that restoring forces of the elongated backbone are responsible for the short-time decay of domain orientation after cessation of shear. On longer time scales, the defect structures that remain may be distorted and, due to Frank elasticity [9], relax in the quiescent fluid with a characteristic time that is governed by the balance between distortional and viscous stresses. Indeed, this could explain the existence of very slow ($\sim 10^5$s) relaxation processes evident in the decay of the transmittance.

6.5 Concluding Remarks

We have discovered that SG-LCP melts can be macroscopically aligned using oscillatory shear. The dynamics of the alignment process appear to be complex, arising from a combination of the dynamics of the backbone, the director field, and the coupling between the two introduced by the spacer. This makes shear-induced alignment qualitatively different and perhaps more effective compared to magnetic field induced alignment. By studying the dynamics during alignment we have found that:

- Viscoelastic measurements on magnetically aligned samples reveal that the dynamic moduli are insensitive to macroscopic director alignment, at small strains.

- In the linear regime (at small strains), the distortion of the polymeric backbone appears to dominate the viscoelastic response. In the nonlinear regime, (at large strains), the energy penalty associated with the distortion of the local director field due to the coupling between the mesogen and the backbone, contributes significantly to stress, causing strain hardening.

- The drop in the low-frequency moduli observed upon shear-induced alignment appears to be an indicator of the peculiar state of SG-LCP conformation, rather than due to fracture instabilities. Over a long period of time, the drop in the modulus appears to recover to those obtained in the unaligned state upon cessation of shear.

- During shear, the backbone conformation is biased along the extensional axis of the flow. This causes the mesogens to choose an intermediate orientation between the direction dictated by the backbone and that dictated by the local director field. Prolonged shearing continuously biases local director orientation to be perpendicular to the extension direction, perhaps forcing the mesogen orientation to propagate to macroscopic dimensions. . Upon cessation of shear, the sample relaxes back to the equilibrium state in two stages. The relaxation of the backbone takes place over a few minutes, whereas the relaxation of the microstructure takes place over several hours.

6.6 Future Work

The flow-induced alignment in SG-LCPs provides a unique opportunity to study the interplay between the dynamics of the polymeric backbone, the director field, the coupling between the two introduced by the spacer, and the defects. More experimental investigations are required before the mechanism of alignment can be understood completely.

Our current interpretation of the results suggests that the distortion of the backbone drives the alignment. Quantitative IR dichroism measurements during and after the alignment process, on backbone labelled SG-LCPs will provide more insight into the evolution of the backbone conformation during and after shear. This coupled with the IR dichroism measurements on mesogen-labelled samples can be used to monitor the relative macroscopic orientation of the backbone and the director field. Quantitative measurements of the dichroism of the mesogen labelled samples can be used to obtain and monitor the 'macroscopic order parameter', during and after alignment. The 'order parameter' can then be used to compare the efficiency of shear-induced and magnetic field-induced alignment processes.

Bibliography

[1] Kannan, R. M.; Kornfield, J. A.; Schwenk, N.; Boeffel, C., *Macromolecules*, **1993**, 26, 2050.

[2] Kannan, R. M.; Kornfield, J. A.; Schwenk, N.; Boeffel, C., *Adv. Materials*, **1994**, 6, 214.

[3] Wang, X. J.; Warner, M., *J. Phys. A:Math.Gen.*, **1987**, 20 (3), 713.

[4] Boeffel, C.; Spiess, H. W., *Macromolecules*, **1988**, 21 (6), 1626.

[5] McArdle, C. B., ed. *Side Chain Liquid Crystal Polymers:* Chapman and Hall: New York, **1989**.

[6] Schatzle, J.; Finkelmann, H., *Mol. Cryst. Liq. Cryst.*, **1987**, 142, 85.

[7] Zentel, R.; Benalia,M., *Makromol. Chemie.*, **1987**, 188 (3), 665.

[8] Finkelmann, H.; Kock, H-J.; Gleim, W.; Rehage, G., *Makro. Chemie., Rapid Comm.*, **1984**, 5, 287.

[9] de Gennes, P.-G. *The Physics of Liquid Crystals*; Clarendon Press: Oxford, **1974**.

[10] Chandrasekhar, S., *Liquid Crystals*; Cambridge University Press: New York, **1977**, 136.

[11] Taratuta, V. G.; Hurd, A. J.; Meyer, R. B., *Phys. Rev. Lett.*, **1985**, 55, 246.

[12] Hatzikiriakos, S. G and J. M. Dealy, *J. Rheology*, **1992**, 36, 845.

[13] Pearson, D. S.; Rochefort, W. E., *J. Poly. Sci., Poly. Phys.*, **1982**, 20, 83).

[14] Chen, Y-L.; Larson, R. G.; Patel, S. S., "Shear fracture of polystyrene melts and solutions," Submitted to *Journal of Rheology*, **1994**.

[15] Winey, K. I.; Patel, S. S.; Larson, R. G.; Watanabe, H., *Macromolecules*, **1993**, 26 (10), 2542.

[16] Dames, B., *Ph. D. Thesis*, Mainz **1990**.

[17] Johnson, S. J.; Frattini, P. L.; Fuller, G. G., *J. Colloid Sci.*, **1985**, 104 (2), 440.

[18] Meissner, V.J., *Rheo.Acta*, **1971**, 10, 230.

[19] Münstedt, H.; Laun, H. M., *Rheo.Acta*, **1981**, 20, 211.

[20] Wang, T. S.; Baird, D. G., *J. Non-newton. fluid mech.*, **1992**, 44, 85.

[21] Kirste, R. G.; Ohm, H. G., *Makromol.Chem.,Rapid Comm.*, **1985**, 6,179.

[22] Götz, S.; Stille, W.; Strobl, G.; Scheuermann, H., *Macromolecules*, **1993**, 26, 1520.

[23] Schwenk, N., unpublished results.

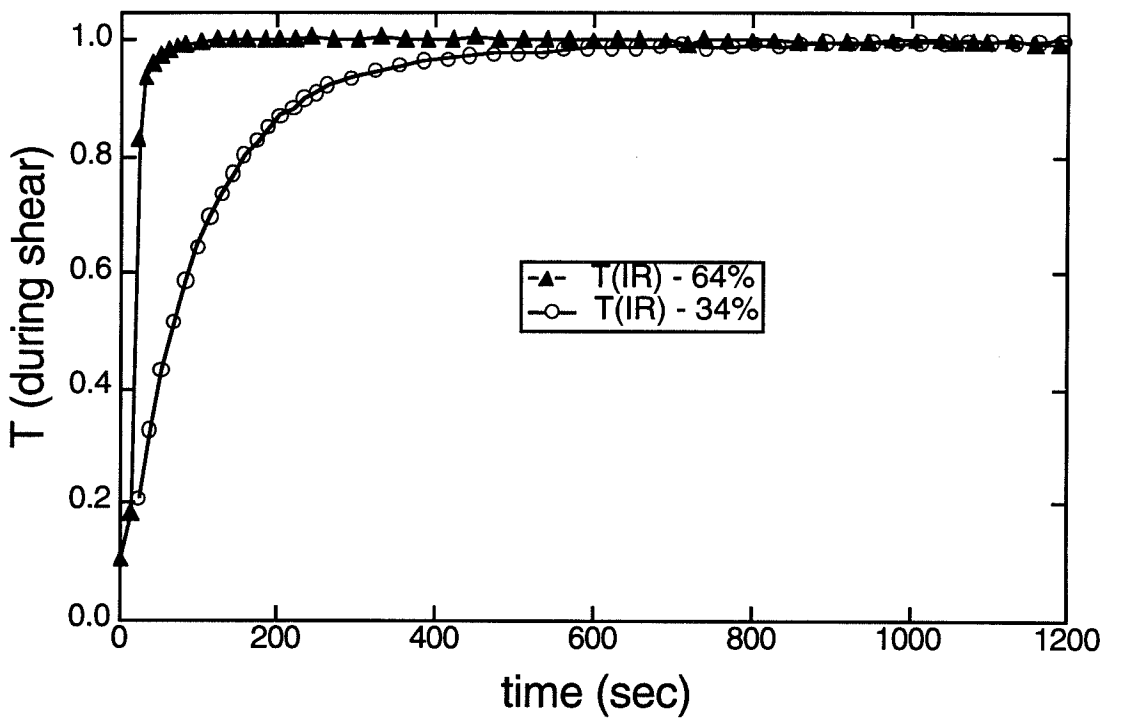

Figure 6.1a: Increase of the IR transmittance of PMd6M-30 with time during large amplitude oscillatory shear.The transmittance is referenced to the isotropic state: $T(t) = I(t)/I_{iso}$, where $I(t)$ is the transmitted intensity at time t and I_{iso} is the transmitted intensity in the isotropic state.

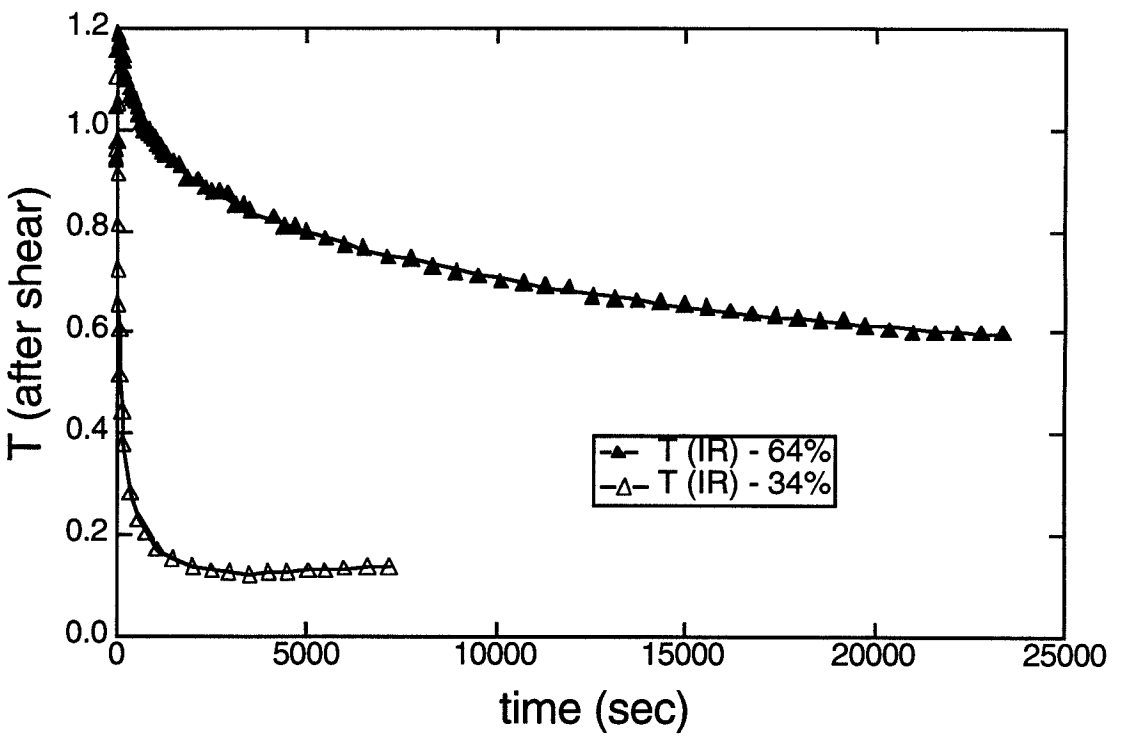

Figure 6.1b: Partial decay of the IR transmittance of PMd6M-30 with time following the cessation of shearing.

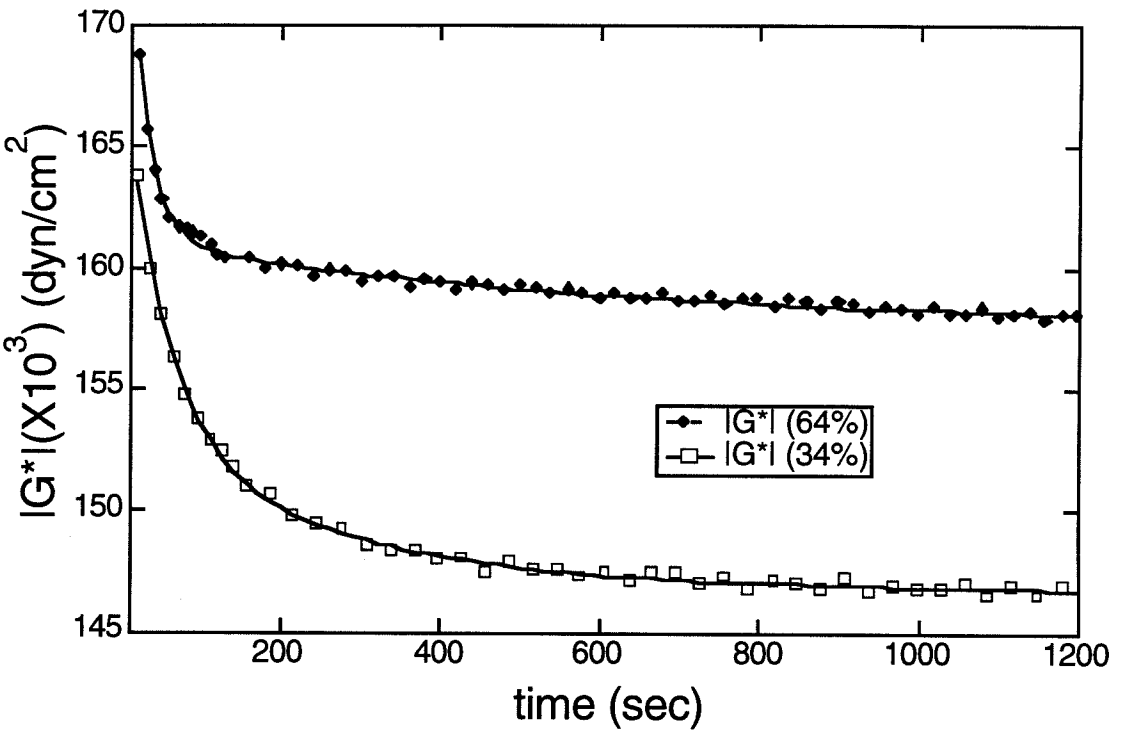

Figure 6.2a: Moduli measurements on PMd6M-30 during shear.**(a)** Decrease of the effective dynamic modulus of PMd6M-30($|G^*|$) during large amplitude oscillatory shear.

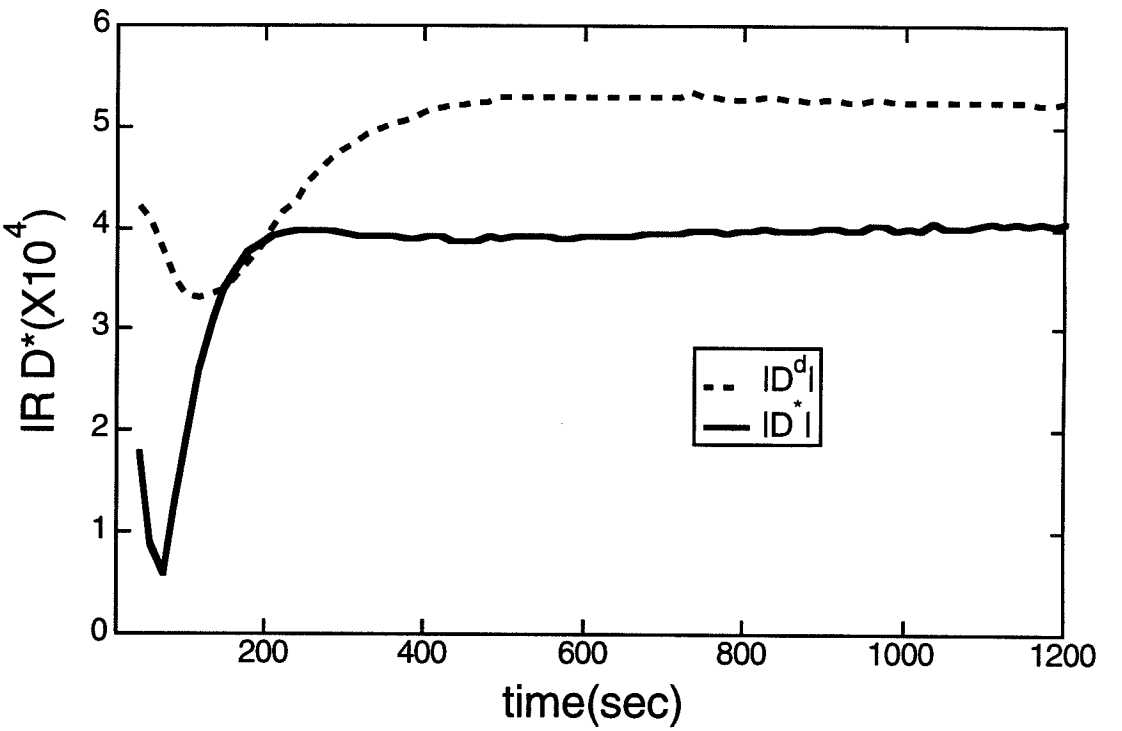

Figure 6.2b: Magnitude of the amplitude ($|D^*|$) and displacement ($|D^d|$) components of the dynamic infrared dichroism in the 1,3-plane during 34% amplitude oscillatory shear.

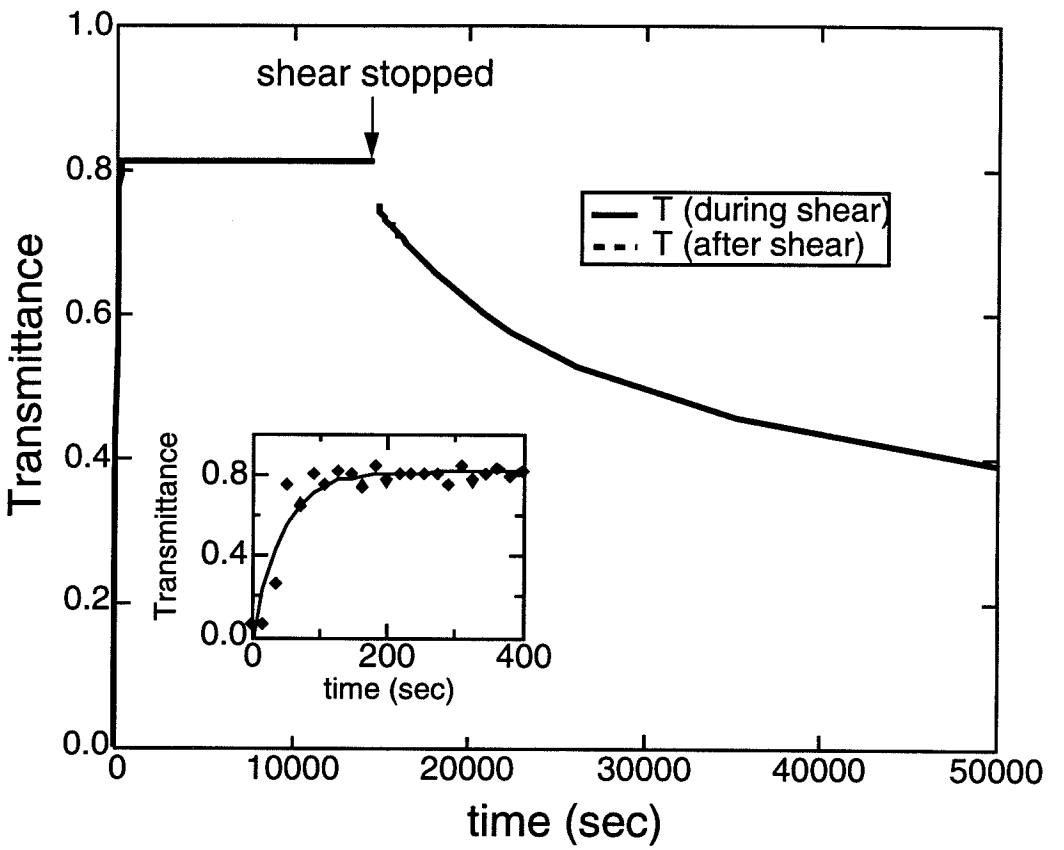

Figure 6.3a: Evolution of transmittance at 633nm, during and after shear-induced alignment at 0.1 r/s, 100% strain at 110°C for 4 hours on PM6M-11.

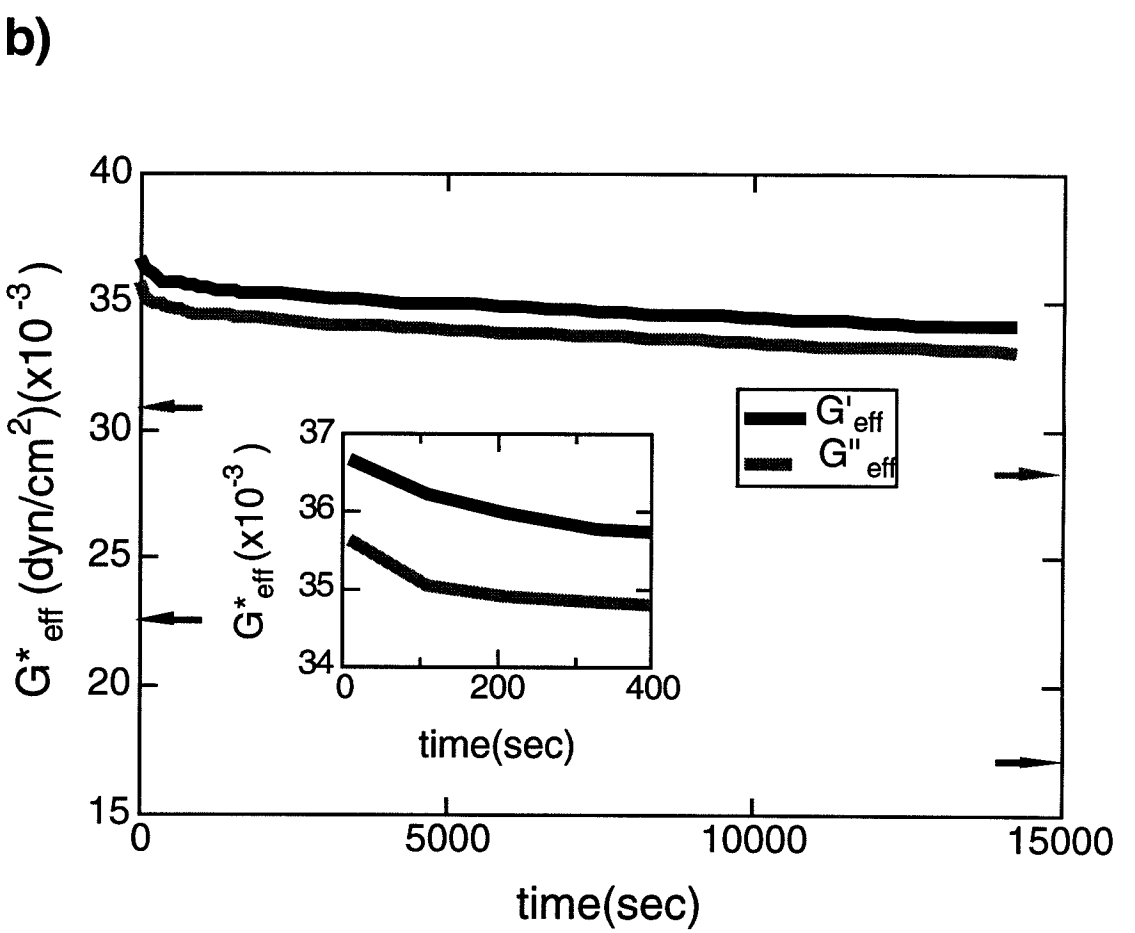

Figure 6.3b: Evolution of the effective storage (G'_{eff}) and loss (G''_{eff}) moduli during shear-induced alignment at 0.1 r/s, 100% strain at 110°C for 4 hours on PM6M-11. The arrows indicate the modulus measured at small strains before and after the alignment process.

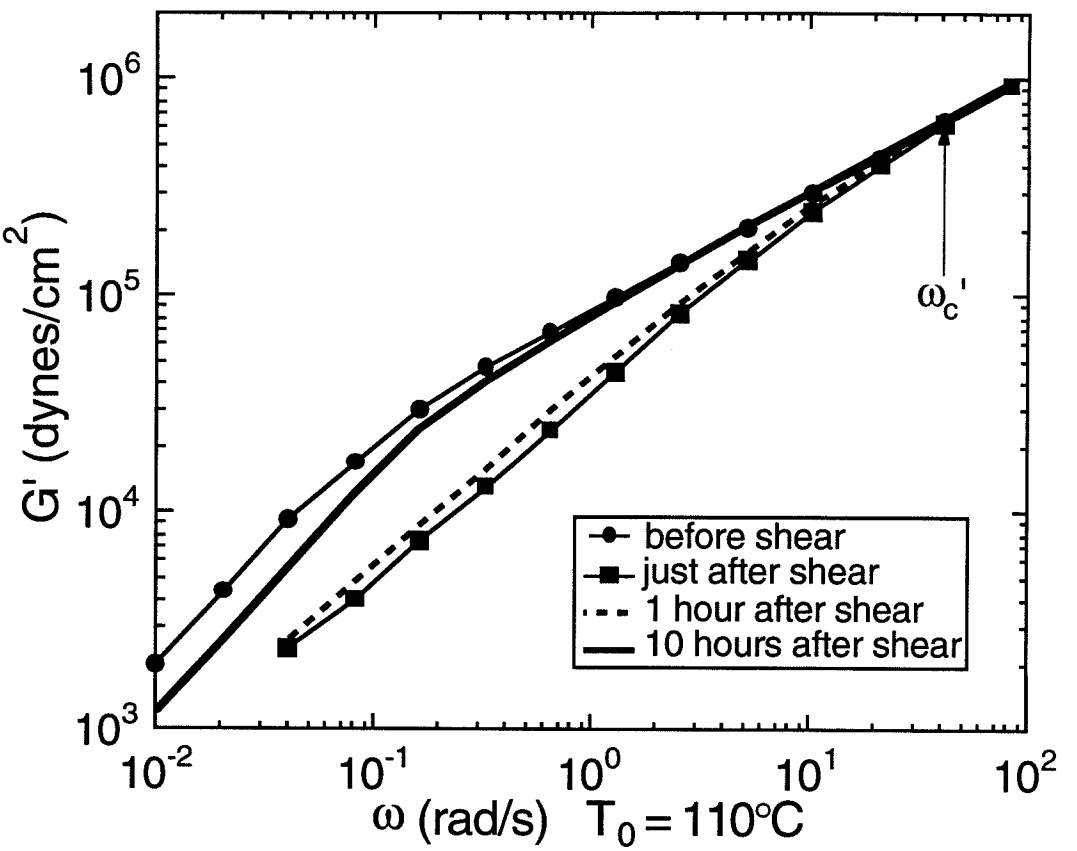

Figure 6.4a: The recovery of the storage modulus measured at small strains after shear-induced alignment at 0.1 r/s, 100% strain at 110°C for 4 hours on PM6M-11. Lines have been drawn through the data points just to guide the eye.

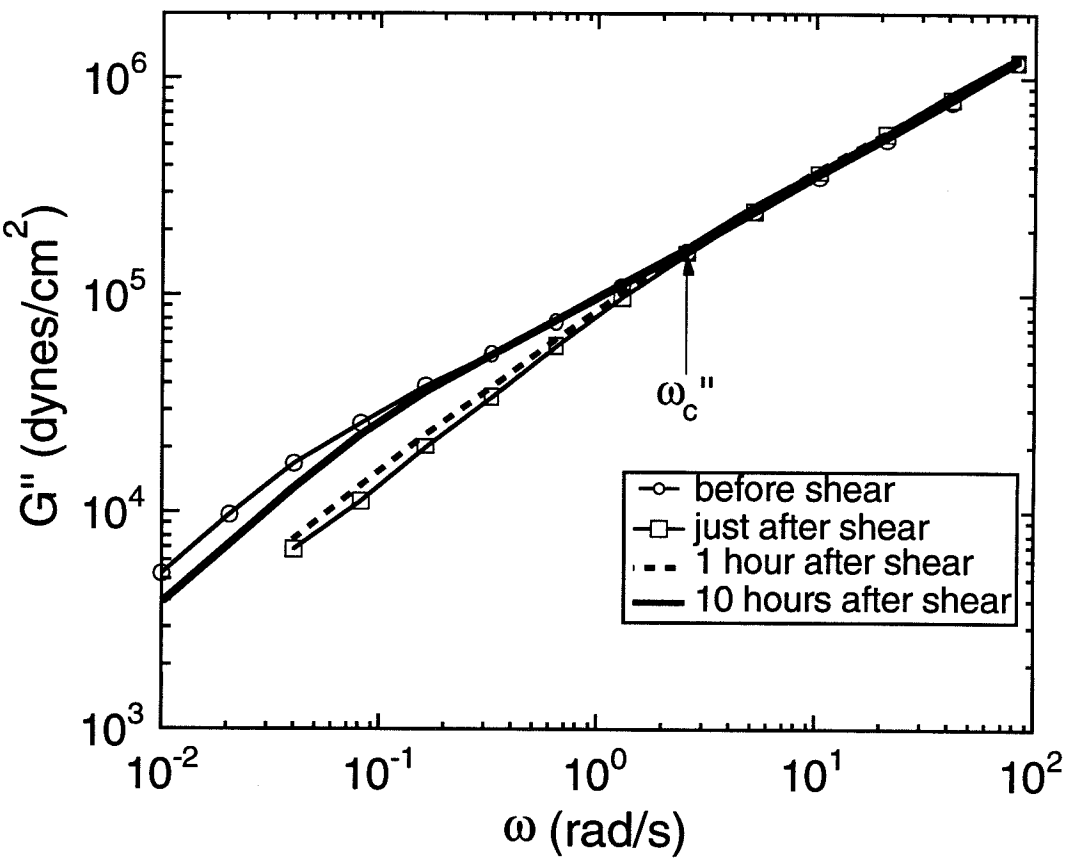

Figure 6.4b: The recovery of the loss modulus measured at small strains after shear-induced alignment at 0.1 r/s, 100% strain at 110°C for 4 hours on PM6M-11. Lines have been drawn through the data points just to guide the eye.

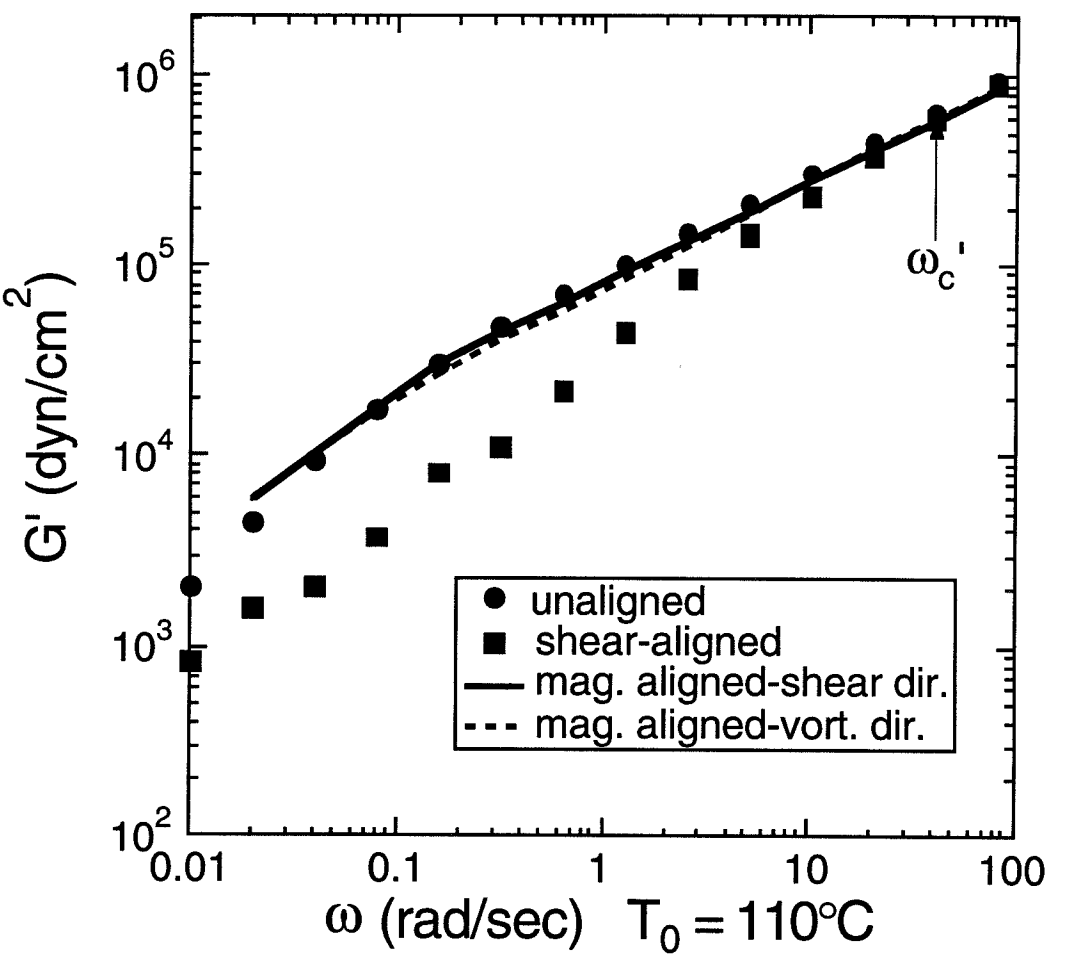

Figure 6.5a: Comparison of the effect of magnetic field-induced alignment and shear-induced alignment on the storage modulus of PM6M-11. The data on the magnetically aligned sample are represented by lines through the data points, for clarity.

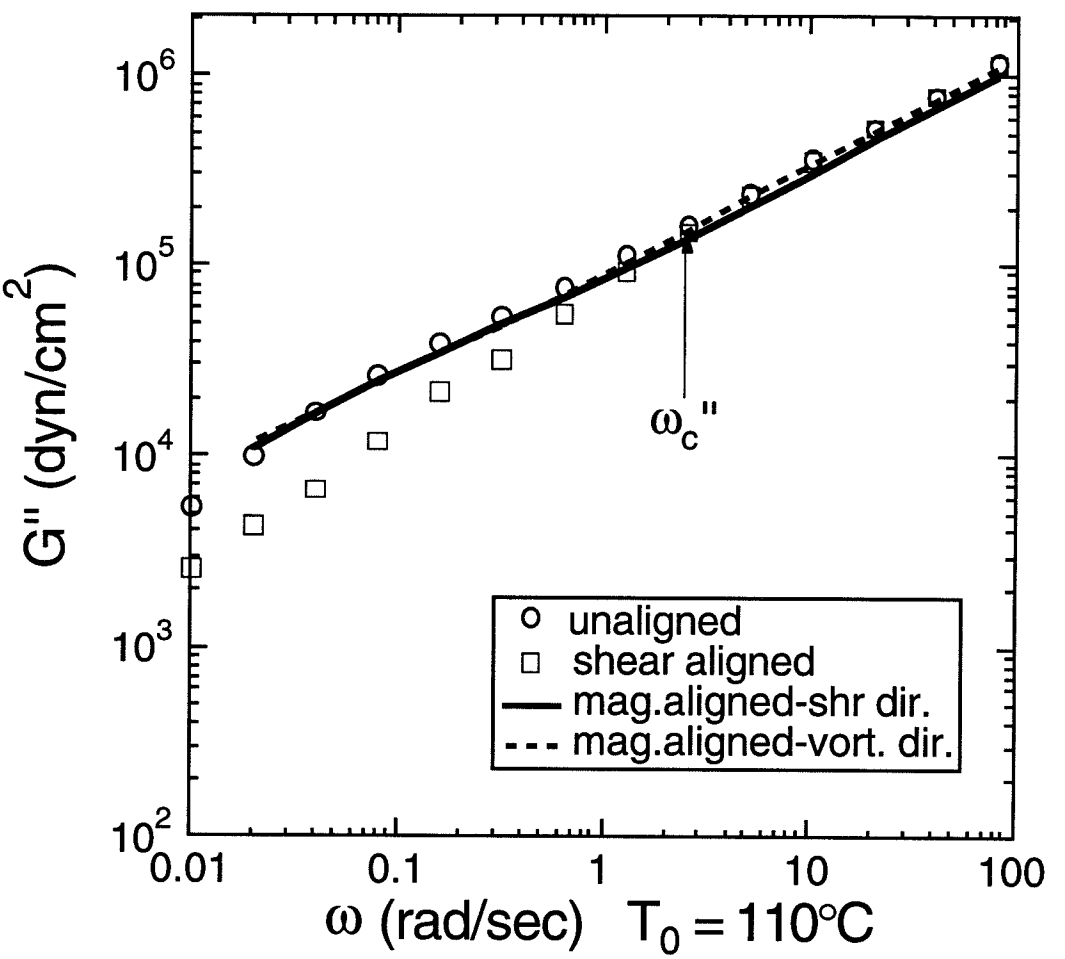

Figure 6.5b: Comparison of the effect of magnetic field-induced alignment and shear-induced alignment on the loss modulus of PM6M-11. The data on the magnetically aligned sample are represented by lines through the data points, for clarity.

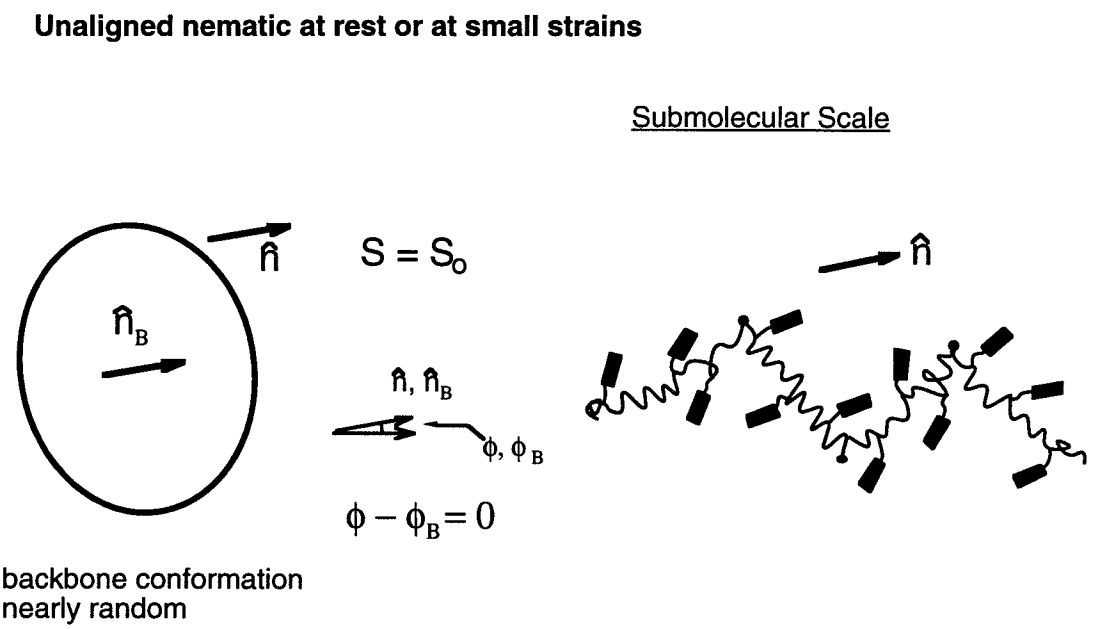

Figure 6.6a: Schematic of the backbone and the mesogens conformation of SG-LCP molecule. Typical size of a domain in the nematic state is 1 micron. Therefore, a domain contains several polymer backbones ($\sim 200\mathring{A}$). At small strains, deformation of the backbone does not result in any distortion of the director field within a domain. However, at large strains, deformation of the backbone results in a significant distortion of the director field.

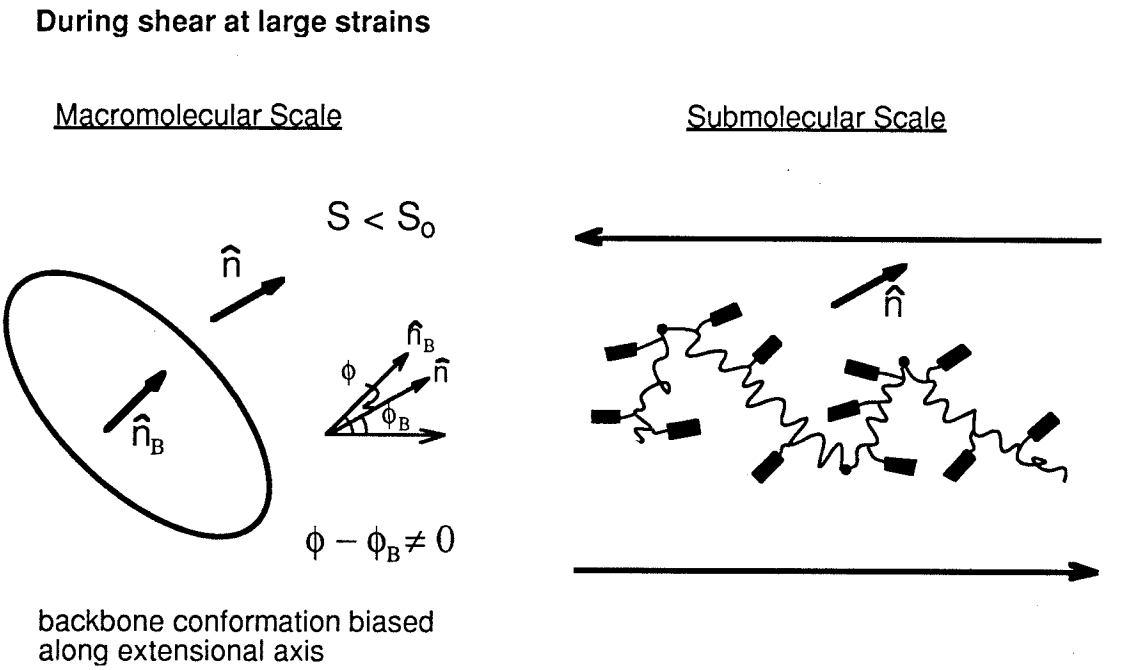

Figure 6.6b: Schematic representation of the mechanism which may be responsible for strain hardening. Various time scales that are relevant for understanding the dynamics of flow-alignment. At high frequencies, we probe the local, glassy modes. At lower frequencies, entanglement effects become important. As frequency is reduced further, we approach the terminal relaxation time of the backbone. At still lower frequencies, slower dynamics of the defects become important. Typically, shear-induced alignment is performed at time scales faster than the relaxation time scales of defects and the backbone.

Chapter 7

Flow-alignment in Lamellar Diblock Copolymers

7.1 Introduction

Block copolymers (BCP) are made of sequences of chemically distinct repeat units connected contiguously into chains. They are widely used as adhesives, thermoplastic rubbers, surfactants and compatibilizers [1], and have been the subject of extensive scientific investigation [2, 3] because of their rich thermodynamics, intriguing rheological behavior, and their value as model systems for understanding general classes of phase transitions [4] and flow phenomena [5, 6].

In this chapter, we focus on the flow behavior of ordered block copolymer melts whose local viscoelastic properties, like colloidal and liquid crystals, are intrinsically anisotropic. Flow fields can be used to introduce a preferred alignment of the microstructure of an ordered BCP, producing materials with highly anisotropic properties [7, 8, 9, 10, 11, 12]. Numerous studies of the effect of shear on cylindrical and lamellar-ordered phases have shown that the axes of the cylinders can be aligned along the flow direction, and the normal to the lamellae can be aligned along the velocity gradient direction ('parallel' alignment) (Figure 7.1). Recently, it has been discovered that, simply by changing the flow conditions, the direction of flow-induced alignment in lamellar diblock copolymers can be 'flipped' to orient the normal to the lamellae ($\hat{\mathbf{n}}$) along the vorticity axis ('perpendicular' alignment) [5, 6, 13, 14]. This discovery may lead to new applications that use BCP melts as 'switchable' materials, and has generated renewed interest in understanding flow alignment of BCP melts.

Although the phenomenon of flow alignment has been known for over two decades [7], the mechanism is not yet understood. Based on the observed changes in mi-

crostructural alignment produced by flow, various notions regarding possible mechanisms of alignment have been proposed [9, 10, 11, 5, 13, 14]. However, a lack of information regarding the dynamic response of the microstructure and macromolecules during flow has made it impossible to discriminate among the concepts put forth in the literature. To address the need for direct observations of the dynamics of flow alignment, we monitor the evolution of the microstructure using simultaneous mechanical and optical measurements. Here, we present the first measurements of stress and birefringence *during* the flow-alignment process. The flow response of a lamellar diblock copolymer melt during 'parallel' alignment is compared with its response during the 'perpendicular' alignment process (Figure 7.1).

We begin by reviewing the previous experimental studies, the conceived mechanisms of flow alignment that motivate our research, and the basis for using birefringence measurements to characterize evolution of the microstructure during flow alignment. Next, we describe the model polymer, apparatus and methods used in this study. Section 7.4 presents the results of dynamic stress and birefringence measurements, characterizing both the effects of flow alignment on the dynamics of a BCP melt and the development of flow alignment as it occurs. We conclude by discussing the implications of these results and directions for future work.

7.2 Background

The phase behavior of diblock $(A-B)$ copolymers in the bulk are largely determined by two factors: χN and f, where χ is the $A-B$ segment-segment interaction param-

eter, N is the overall length of the polymer and f is the fraction of the A component [2]. When the repulsive interaction ($\sim \chi N$) is sufficiently weak, entropy dominates and the polymer exists in a compositionally-disordered phase. As χN increases, the repulsive interactions favor a reduction in the number of $A - B$ contacts. Above a critical value of χN, the two blocks segregate into ordered microstructures. This transition is referred to as the order-disorder transition (ODT). The morphology of the ordered microstructure depends on f. When the BCP orders, the orientation of the principal axes of the microstructure vary with position in the sample, and various defects are trapped in the material [12, 13, 14]. In the absence of a symmetry-breaking field, the ordered material is isotropic on a macroscopic scale [7, 10].

7.2.1 Flow-Induced Alignment

While a preferred orientation can be introduced by electric fields [15] or surface effects [16], flow provides the most potent means to manipulate the macroscopic alignment of the microstructure of ordered block copolymers [5, 7, 8, 9, 10, 11, 12]. Flow-induced alignment of BCPs was discovered in a styrene-butadiene-styrene (SBS) triblock copolymer with a cylindrical ordered morphology [7, 8]. Subsequently, it was shown that oscillatory shear is effective in orienting cylindrical and lamellar-ordered phases of block copolymers [9]. The resulting alignment of the long axis of the cylinders was found to be along the flow direction. Lamellae were found to align normal to the velocity gradient.

To explain flow alignment, Hadziioannou *et al.* [9] offered the following concepts

regarding possible mechanisms: selective rotation of "grains"[1] in the material, selective melting of grains, and defect migration. The first of these notions attributes flow alignment to the anisotropic viscoelastic properties of the ordered microstructure, which was hypothesized to lead to a progressive alignment of grains along the direction that minimizes their resistance to flow. Selective melting was offered as an alternative or supplemental mechanism that produces alignment by selectively disordering domains in which the microstructure is oriented in 'unfavorable' directions, resulting in a progressive elimination of all but one alignment. Indeed, in a shear flow, there is a 'least favorable' alignment: lamellae oriented with their normal $\hat{\mathbf{n}}$ along the flow direction $\hat{\mathbf{n}} \cdot \mathbf{v} = 1$ would experience layer compression if they deformed affinely; whereas lamellae with $\hat{\mathbf{n}} \cdot \mathbf{v} = 0$ can shear without layer compression. Thus, regions with $\hat{\mathbf{n}} \cdot \mathbf{v} = 1$ are relatively rigid and more likely to be subjected to destabilizing distortions of their lamellar spacing [17]. Finally, defect migration was added as a mechanism for grain boundaries to anneal out of the material once the grains themselves had been aligned. Unfortunately, without any information on the dynamics of flow alignment itself, it was not possible to test the validity of these general notions, nor to develop a more precise description of the actual mechanism of flow alignment.

The quest for a mechanism for flow alignment became a search for at least three mechanisms when Koppi *et al.* [5] discovered that the direction of orientation of lamellar diblock copolymers is not always along the flow direction, but could be flipped 90° (Figure 7.1) by changing the flow conditions. This behavior was found to be restricted

[1]Regions in which the orientation is uniform are limited in extent by various defects. The terms "grains," "domains" and "crystallites" have all been used to describe these regions.

to temperatures near the ODT and to frequencies that were slow when compared to molecular relaxation (ω_x), but fast when compared to some critical frequency. The precise limits of the 'perpendicular' regime are not yet known, but there appears to be an island surrounded by conditions producing parallel alignment at lower frequency and/or stronger ordering. Bates and co-workers have also found that shearing the sample just above the ODT can induce ordering, and the lamellae form aligned along the 'perpendicular' direction [6]. Regarding the mechanism that produces 'perpendicular' alignment, the observation that this orientation is found only near the ODT suggests that fluctuations play a key role. Perpendicular alignment has since been observed in a polystyrene-polyisoprene (12.5k-9.5k, denoted SI 12/9) lamellar diblock, also at frequencies that are slow compared to macromolecular relaxation and at temperatures close to the ODT [14]. However, a regime of parallel alignment at frequencies below those producing perpendicular alignment has not yet been reported in any other system; in contrast, SI 12/9 is driven toward 'parallel' alignment at sufficiently high shear frequencies such that the rheology is dominated by the polymeric contributions (Rouse and glassy modes) [13]. Together, these observations suggest that three different mechanisms of flow alignment may exist and that entanglement, viscoelastic contrast between the lamellae, and the strength of order are likely to be important factors in determining the flow behavior of BCPs.

The first steps toward investigating the evolution of flow alignment were taken by Morrison *et al.* [10, 11], who examined samples of a styrene-butadiene-styrene (SBS) triblock with cylindrical morphology quenched at intermediate states of alignment.

Based on their observations, they proposed that below a critical stress flow alignment occurred due to the flow of 'grains' such that the domains are not disrupted and may flow as a unit; above the critical stress, flow alignment occurred by selective melting or by a combination of the flow of grains and selective melting. Their results reinforce questions that have persisted in the literature regarding the microrheology of flow alignment, its dependency on proximity to the ODT, proximity to the glass transition of one or both blocks, and shear rate or shear stress.

To address the need for information on the dynamics of block copolymers during flow alignment, one requires experimental methods to characterize the changes in the microstructure induced by flow, and their relationship to changes in the macroscopic viscoelastic properties of the material. Rheo-optical methods are particularly well suited to observe the development of alignment of the ordered structures in BCPs, and the molecular and microstructural responses that lead to it. The general principle behind optical-rheometry is to use the connection between the state of the microstructure of a fluid and the observable anisotropies in its optical properties [19]. We take advantage of the relationship between BCP microstructure and anisotropy in its refractive index, or birefringence.

7.2.2 Flow Birefringence of Block Copolymers

The birefringence of a quiescent, ordered block copolymer carries information about the orientation distribution of the microstructure. Two contributions can be distinguished: the tendency of the chains to align perpendicular to interfaces in the mate-

rial (intrinsic birefringence) and the anisotropy of the phase-separated microstructure (form birefringence). In the case of lamellar and cylindrical morphologies, *both* contributions are coaxial, so that the principle axes of the refractive index tensor coincide with those of the ordered structure [20]. Thus, in a sufficiently weak flow that the conformation of the chains is not significantly distorted from equilibrium, the birefringence of a lamellar block copolymer provides a means to measure the second moment of the orientation distribution of the layer normal.

In a quiescent homopolymer melt, all orientations of the end-to-end vector are equally probable and the polymer is optically isotropic. When subjected to stress, the melt flows and the conformation of the chains is perturbed. The bias in the orientation distribution of chain segments is manifested in anisotropic optical properties. For homopolymer melts and concentrated solutions over a wide range of flow conditions, birefringence is related to stress by the stress-optical rule: the deviatoric parts of the stress tensor and the refractive index tensor are proportional to each other [21].

Ordered block copolymers can be birefringent even at rest. Therefore, the stress-optical rule cannot be valid in general. Nevertheless, under flow conditions that perturb the chain conformations significantly from that dictated by the microphase structure, the stress and birefringence might both be dominated by the contributions associated with the distortion of the chain conformation. This is most likely to be the case when the time scale of the flow is rapid compared to conformational relaxation. In this regime, the stress can be expected to disturb the segmental orientation distribution of the molecules, producing a contribution to intrinsic birefringence. If this

contribution dominates over the birefringence associated with the microstructure, the stress-optical rule would then be found to hold in this regime of rapid deformation. As the time scale of the flow slows, the birefringence associated with the microstructure becomes increasingly important relative to the birefringence arising from the distortion of chain conformation, and there is no reason to expect the stress-optical rule to hold. Therefore, it is of interest to examine the conditions for applicability of the stress-optical rule to block copolymers and the way the stress-optical rule fails when it does.

Previous studies of flow alignment motivate us to investigate the mechanisms that lead to parallel and perpendicular alignment. In order to achieve this, we monitor the evolution of the microstructure by measuring stress and birefringence before, during and after the alignment process. While stress is sensitive to the macroscopic response, birefringence is sensitive to both the molecular and microstructural responses. Here we show that, together, they provide insight regarding the mechanism of flow alignment.

7.3 Experimental Section

7.3.1 Material

The polymer used in this study is a nearly symmetric poly(ethylenepropylene)-poly(ethylethylene) diblock copolymer of $M_w = 50,100$ g/mol (PEP-PEE-2) synthesized by F. S. Bates [22]. The synthesis, characterization and the viscoelastic

properties of this polymer have been described previously by Bates and co-workers [22, 23]. It possesses good thermal and oxidative stability, a readily accessible ODT ($T_{ODT} = 96°C$), blocks that are long enough to be entangled, and a narrow molecular weight distribution ($M_w/M_n = 1.07$). 'Flipping' was discovered in PEP-PEE-2D, the partially deuterated counterpart of the present material [5]. It has been shown that when PEP-PEE-2 is subjected to prolonged oscillatory shear at $T/T_{ODT} = 0.97$ with 100% strain amplitude, using a shear frequency $\omega = 0.02$ rad/s enhances parallel alignment, and using $\omega = 1$ rad/s produces perpendicular alignment [5].

7.3.2 Apparatus

The mechanical and stress-optical properties of this block copolymer were characterized using a rheo-optical apparatus developed in our laboratory described in Chapter 2. The center of the apparatus is the Rheometrics RSA-II dynamic mechanical testing system, which was modified to permit optical measurements. Dynamic birefringence was measured using a polarization-modulation scheme (optical train, Figure 2.2) [24]. This rheo-optical apparatus is described in detail elsewhere [25, 26]. It is uniquely suited for simultaneous, quantitative measurements of dynamic stress and birefringence over a wide range of frequency (0.01 to 100 rad/s) and temperature (-100 to 400°C).

Rheo-optical experiments were performed using the 'shear-sandwich' geometry, with the optical axis either along the velocity gradient direction or along the vorticity direction (Figure 2.3), thus enabling us to probe two different projections of the

anisotropic refractive index tensor. This is particularly useful because the projection that is most sensitive to the evolution of the microstructure depends on the direction of the lamellar alignment. Birefringence in the 1,2-plane or 1,3-plane is measured with the optical axis along the vorticity direction (axis 3, Figure 2.3) or the velocity gradient direction (axis 2, Figure 2.3), respectively.

7.3.3 Stress and Birefringence in BCPs

In shear flow with the coordinate system of Figure 2.3, the stress tensor has the following nonzero terms:

$$\sigma = \begin{bmatrix} \sigma_{11} & \sigma_{12} & 0 \\ \sigma_{12} & \sigma_{22} & 0 \\ 0 & 0 & \sigma_{33} \end{bmatrix}. \tag{7.1}$$

By symmetry we expect the shear stress σ_{12} to be an odd function of the strain, and the normal stress differences $N_1 = \sigma_{11} - \sigma_{22}$ and $N_2 = \sigma_{22} - \sigma_{33}$ to be even functions of the strain. In the case of oscillatory shear $\gamma(t) = \gamma_o \sin \omega t$, if γ_o is small we expect only the leading terms to dominate. Thus, σ_{12} is expected to be sinusoidal with the same frequency as the applied strain. While flow certainly can perturb the microstructure and consequently the viscoelastic properties of block copolymer melts, there may exist sufficiently small strain amplitudes that the complex amplitude of the stress oscillation is linear in the strain and independent of time during prolonged shear. When this is the case we can define storage and loss moduli, $G'(\omega)$ and $G''(\omega)$, for the block copolymer that depend on temperature and on the previous (large

amplitude) flow history of the material:

$$\sigma_{12} = \gamma_o[G'\sin\omega t + G''\cos\omega t]. \tag{7.2}$$

There may exist an intermediate range of γ_o for which the shear stress can be described in terms of effective dynamic moduli G^*_{eff}, which change with time during prolonged shear due to flow-induced changes in fluid structure [27].

We restrict ourselves here to sufficiently small strains that the shear stress is simply sinusoidal at the frequency ω. We perform two types of experiments. One type ("frequency-sweep") uses such small strain amplitude that no change in viscoelastic properties is observed even after completing experiments over a wide range of frequency. The second type ("flow-alignment") uses strain amplitude large enough to produce alignment of the lamellae, but with small enough strain that the stress can be described using G^*_{eff}, which is monitored as a function of time during prolonged shearing.

In a shear flow, the refractive index tensor $\mathbf{n}$ has a form similar to the stress tensor:

$$\mathbf{n} = \begin{bmatrix} n_{11} & n_{12} & 0 \\ n_{12} & n_{22} & 0 \\ 0 & 0 & n_{33} \end{bmatrix}. \tag{7.3}$$

Regarding the birefringence, we are concerned with two particular projections of $\mathbf{n}$. The projection on the 1,2-plane, $\mathbf{n}_{12}$, is observed when the optical axis coincides with

the vorticity axis:

$$\mathbf{n}_{12} = \begin{bmatrix} n_{11} & n_{12} \\ n_{12} & n_{22} \end{bmatrix}. \tag{7.4}$$

The magnitude of the birefringence in the 1,2-plane, Δn_{12}, is equal to the difference between the principle eigenvalues of $\mathbf{n}_{12}$. In terms of the experimentally observed Δn_{12} and orientation angle α of the principle axis of $\mathbf{n}_{12}$ with respect to the flow direction,

$$n_{12} = \frac{1}{2}\Delta n_{12} \sin(2\alpha), \tag{7.5}$$

and

$$n_{11} - n_{22} = \Delta n_{12} \cos(2\alpha). \tag{7.6}$$

The projection of $\mathbf{n}$ on the 1,3-plane, $\mathbf{n}_{13}$, is probed when the optical axis is along the velocity gradient. The principal axes of $\mathbf{n}_{13}$ coincide with axes 1 and 3 (*i.e.*, $\alpha = 0$), so its anisotropy is completely described by the magnitude of the birefringence $\Delta n_{13} = n_{11} - n_{33}$.

Neglecting the symmetry breaking involved in the choice of the initial and final shearing directions, we expect similar small strain regimes for n_{12} as for σ_{12}. We define a complex birefringence coefficient $B^* = B' + iB''$ for n_{12} by [28]

$$n_{12} = \gamma_o[B'\sin\omega t + B''\cos\omega t]. \tag{7.7}$$

Like the shear stress, there may exist a regime of sufficiently small strain that B^* is simply a function of the shear frequency and the state of the microstructure. At

somewhat larger strains, the effect of oscillatory shear on the microstructure of the fluid may be manifested in changes in the dynamic birefringence with time, which can be described by $B^*_{eff}(t)$ [27].

Again, neglecting the symmetry breaking involved in choosing an initial flow direction, one does not expect n_{12} to build up due to oscillatory shear (*i.e.*, it will oscillate about zero). Consequently, if a particular orientation of the projection of the lamellar normal in the 1,2-plane were enhanced by oscillatory shear, it would be directed along one of the axes (1 or 2) and would be manifested in $n_{11} - n_{22}$. Similarly, if a particular orientation of the projection of the lamellar normal in the 1,3-plane tends to be aligned by flow, it will be manifested in $n_{11} - n_{33}$. Thus, the evolution of the steady offset in $n_{11} - n_{22}$ and $n_{11} - n_{33}$ is sensitive to the development of alignment.

To characterize the relative magnitude of the birefringence compared to stress, we define three stress-optic ratios based on the magnitude, the real part, and the imaginary parts of the complex birefringence coefficient and the dynamic modulus:

$$SOR = \frac{|B^*|}{|G^*|} , \tag{7.8}$$

$$SOR_{Re} = \frac{B'}{G'} , \tag{7.9}$$

and

$$SOR_{Im} = \frac{B''}{G''} . \tag{7.10}$$

For homopolymer melts, under the relatively mild flow conditions of interest here, the stress-optical rule would hold and SOR, SOR_{Re} and SOR_{Im} would be inde-

pendent of frequency and all equal to the stress-optic coefficient, C. For BCPs, the specific way in which the stress-optical rule breaks down may offer clues regarding microstructural dynamics. Examining the stress-optical behavior using these ratios exposes different regimes of flow response in terms of the relationship between molecular/microstructural orientation and stress.

7.3.4 Methods

Two types of oscillatory shear protocols were used, as described above: (1) frequency sweeps at small-strain amplitudes ($\leq$ 9%) to characterize the state of the sample before and after alignment, and (2) prolonged, large amplitude (roughly 100%) oscillatory shear at a fixed frequency to induce macroscopic alignment of the microstructure. Stress and birefringence were recorded simultaneously during both types of experiments.

We report rheo-optical measurements during the flow-alignment process at two different frequencies at 87°C and 90% strain: (1) at 0.02 rad/s for 92 cycles, and (2) at 1 rad/s for 1800 cycles. As mentioned above, similar conditions have previously been shown to produce 'parallel' and 'perpendicular' alignment, respectively [5]. To establish a reproducible initial condition before each alignment experiment, the sample was heated well into the disordered phase (135°C) and allowed to relax at that temperature for 25 minutes. The sample was then cooled to the desired temperature in the ordered state. This procedure resulted in a reproducible unaligned initial state, confirmed by the rheo-optical measurements before and during the alignment process.

7.4 Results

7.4.1 Stress-Optical Properties Before & After Alignment

The dynamic moduli and complex birefringence coefficient were measured at 22, 45, 65 and 87°C using small amplitude oscillatory shear. Frequency-sweep experiments were performed first on the unaligned BCP, then on the aligned states obtained by prolonged oscillatory shear. The aligned state of the material was designated 'parallel' after 7 hours of shearing at $\gamma_o = 90\%$ and $\omega = 0.02$ rad/s at 87°C (similar to the conditions that produced parallel alignment as indicated by SANS [5]). It was designated 'perpendicular' after 2.5 hours of shearing at $\gamma_o = 90\%$ and $\omega = 1$ rad/s (again based on previous SANS results [5]).

The dynamic moduli (G^*) measured at different temperatures ($T \leq 87$°C) could be superimposed by using appropriate shift factors (Table 7.1). The frequency (a_T) and vertical (b_T) shift factors are very close to the values reported previously [23]. A master curve for the dynamic birefringence (B^*) is obtained with identical frequency shift factors, but with slightly different vertical shift factors ($b_{T,so}$ in Table 7.1) due to the temperature dependence of the effective stress-optic coefficient, described below.

The dynamic birefringence and dynamic modulus master curves of an unaligned BCP are compared in Figure 7.2. At high reduced frequencies, the dynamic birefringence and dynamic modulus may be superimposed by dividing B^* by an effective stress-optic coefficient C_{eff}. This shifted dynamic birefringence is denoted as G^*_{so}. At all accessible frequencies at 22 and 45°C, SOR_{Re} and SOR_{Im} are constant and

equal to each other, leading to the values of C_{eff} given in Table 7.1. At 65 and 87°C, C_{eff} is calculated using the results at high enough frequencies that SOR_{Re} and SOR_{Im} are independent of frequency and equal to each other. The temperature dependence of C_{eff} is in accord with that observed for PEP homopolymer melts [25], and accounts for the difference in vertical shift factors for G^* and B^* (Table 7.1).

Thus, the stress-optical rule appears to hold above a critical frequency. With decreasing frequency, deviations from the stress-optical rule are first evident in the elastic-like character (G' and G'_{so}), below a critical frequency $\omega'_{c,so}$. Deviations are evident in the loss-like behavior (G'' and G''_{so}) only at much lower frequency, below $\omega''_{c,so}$. Both of these are at least an order of magnitude smaller than the frequency where the storage and loss moduli cross (ω_x).

The dynamic moduli and birefringence are modified by flow alignment. In the low-frequency regime where viscoelastic properties are sensitive to the order-disorder transition [23], the dynamic moduli of PEP-PEE-2 are reduced by flow alignment (Figure 7.3). The dynamic moduli observed using $\gamma_o \leq 2\%$ are in agreement with those reported previously [5], for both the perpendicular and parallel-aligned states. For comparison with earlier work, the critical frequencies, below which the storage and loss moduli are sensitive to the ordering transition, are indicated by ω'_c and ω''_c, respectively (Figure 7.3). At the lowest reduced frequencies, we resorted to using a higher strain (9%), which was accompanied by a noticeable decrease in the storage modulus.

The way that the stress-optical rule fails at low frequency (Figure 7.4) is also

modified by flow alignment. In particular, the regime in which the stress-optical rule appears to hold extends to lower frequency in flow aligned states. To compare the unaligned, 'parallel' and 'perpendicular' samples, we use the stress-optic ratio SOR based on the amplitudes of the oscillatory stress and birefringence (Figure 7.4). For the unaligned material, this ratio is constant at high enough frequencies (above $\omega_{c,so} \approx 2$ rad/s, consistent with the results shown in Figure 7.2). Below this frequency the birefringence per unit stress increases with decreasing frequency. Although the results in this regime do not cover a wide dynamic range, they suggest that there may be a power-law regime ($\sim \omega^{-\frac{1}{2}}$ is shown for comparison in Figure 7.4). The two aligned states have similar $SOR(\omega)$, each with a critical frequency that is an order of magnitude smaller than that observed for the unaligned state.

7.4.2 Stress-Optical Behavior During 'Parallel' Alignment

During prolonged large amplitude shear at 0.02 rad/s at constant strain amplitude, the magnitudes of the σ_{12} and n_{12} oscillations decrease and a displacement develops in $n_{11} - n_{22}$ (Figure 7.5). The decrease in the amplitude of the oscillation of n_{12} is more dramatic than that of σ_{12}. The magnitude and time scale of the growth of the displacement of $n_{11} - n_{22}$ appear to be correlated with the magnitude and rate of the decrease in the amplitude of n_{12}.

Both σ_{12} and n_{12} oscillate with the same frequency as the applied strain. Thus, they can be described in terms of complex coefficients $G^*_{eff}(t)$ and $B^*_{eff}(t)$. The effective storage and loss moduli (Figure 7.6a) decrease over seven hours of shearing,

but the decay in G'_{eff} is more pronounced than that of G''_{eff}. For reference, the moduli observed at 9% strain are indicated by arrows. During the parallel alignment process B^*_{eff} decreases more strongly than G^*_{eff}, with B'_{eff} falling by an order of magnitude and B''_{eff} dropping by a factor of four (Figure 7.6b). Thus, the relative magnitude of the birefringence compared to the stress, SOR, decreases significantly, and this decrease is associated with the elastic-like response of the material SOR_{Re} (Figure 7.6c).

7.4.3 Stress-Optical Behavior During 'Perpendicular' Alignment

The development of perpendicular alignment is monitored in a similar way, with the distinction that the displacement of the birefringence in the 1,3-plane is recorded to monitor the progressive alignment of the lamellae. The shear stress and birefringence n_{12} are again described by $G^*_{eff}(t)$ and $B^*_{eff}(t)$ (Figure 7.7a,b). The lossy character (G''_{eff} and B''_{eff}) is almost unchanged as alignment progresses. During the first 3000 s, G'_{eff} and B'_{eff} decrease together. The monotonic development of perpendicular alignment is manifested in the displacement component of $n_{11} - n_{33}$ (Figure 7.7c). The sharp increase in $|(n_{11} - n_{33})(d)|$ during the first 200 s coincides with the period when most of the decrease in G'_{eff} and B'_{eff} occurs. Nevertheless, the displacement $|(n_{11} - n_{33})(d)|$ doubles over the next 4000 s, while G'_{eff} decreases only 25% and B'_{eff} becomes erratic.

7.5 Discussion

7.5.1 Dynamics of the Unaligned, Lamellar Melt

Comparison of the dynamic shear stress and birefringence in the ordered but unaligned BCP melt reveals a frequency regime where the stress-optic rule appears to hold ($\sigma_{12} \propto n_{12}$) (Figure 7.2). Since the form birefringence is negligible compared to the intrinsic birefringence in PEP-PEE diblock copolymers [20], the birefringence reveals the segmental orientation of the chains. In the regime where $\sigma_{12} \propto n_{12}$, both the shear stress and the dynamic birefringence n_{12} are primarily associated with the distortion of chain conformation. Indeed this behavior is confined to frequencies near and above the terminal molecular relaxation time ($\omega \geq \frac{1}{4}\omega_x$). As frequency decreases, there is a cross-over to a regime where the relative magnitude of n_{12} with respect to σ_{12} increases with decreasing frequency. This cross-over occurs first in the storage components (G' and B'), as the elastic character associated with the relaxation of entanglements becomes less significant than the elasticity associated with the microstructure. In unaligned PEP-PEE-2, G' and G'_{so} diverge below a critical frequency $\omega'_{c,so}$ that is only slightly lower than ω'_c (the frequency below which G' is sensitive to the ordering transition). The critical frequency $\omega''_{c,so}$ below which the lossy character shows deviations between G'' and G''_{so} is far below not only $\omega'_{c,so}$, but also ω''_c. Its value corresponds to ω_d reported by Koppi *et al.* [5] in unaligned, ordered PEP-PEE-2 and which they associated with defect motions ($\omega_d a_T \approx 0.4$ rad/s for $T_o = 87°C$). We believe that the regime between $\omega'_{c,so}$ and $\omega''_{c,so}$ is that in

which the viscoelastic response is governed by the layered structure in the material, as is described next.

Just below ω_c' and ω_c'' there is a power-law region where $G' \sim G'' \sim \omega^{0.7}$, as has been reported previously [23]. This type of behavior, intermediate between a solid and liquid, appears to be characteristic of layered liquids in general [30]. Kawasaki and Onuki have shown that for a layered liquid with modulus B for layer compression, viscosity η_o and isotropic distribution of lamellar orientation, at frequencies below a critical frequency $\omega_c \equiv B/\eta_o$, the dynamic moduli are $G' \approx G'' \approx \frac{\pi}{24\sqrt{2}}(B\eta_o\omega)^{\frac{1}{2}}$ [31]. This regime is cut-off at low frequency by the contributions of defect structures. If the layer spacing is λ_s and the typical distance between defects is l_D, then this lower-frequency cross-over is anticipated at $\omega(\lambda_s/l_D)^2$. Extending this analysis to the stress-optical behavior, Milner and Fredrickson have shown that in this intermediate range of frequencies where the layer structure dominates the viscoelasticity, the stress-optic ratio should scale as $SOR \sim \omega^{-\frac{1}{2}}$ [32].

This theoretical picture explains the existence of an intermediate range of frequency in which the viscoelastic relaxation shows power-law behavior. In this region it is anticipated that the stress-optic rule will fail, with a power-law dependence of SOR. This regime is limited on the high-frequency side by the domain in which the viscoelasticity is dominated by molecular relaxation, and on the low frequency side by the contribution of the larger-scale structure (presumably focal conic defects and grain boundaries). Our results provide strong support for this physical picture of the dynamics of an unaligned, lamellar BCP melt.

7.5.2 Effect of Alignment on Dynamics

Stress-optical measurements on aligned samples show that the frequency regime in which the stress-optical rule appears to hold extends to lower frequencies in aligned samples than in unaligned PEP-PEE-2 (Figure 7.4). Since the dynamics that enhance SOR at low frequency are eliminated by alignment, the deviations from the stress-optical rule are associated with inhomogeneous orientation and/or defect structures trapped in an unaligned or partially aligned BCP. This is reasonable, since a sample with perfect lamellar alignment, in either the parallel or the perpendicular orientation, subjected to oscillatory shear of $\gamma_o \leq 100\%$ would not experience significant distortion of the layer spacing or curvature. Thus, the shear stress and n_{12} would be primarily associated with the distortion of the conformation of the polymers, and the stress-optical rule would be expected hold for the n_{12} and σ_{12} in an ideal, aligned BCP.

With respect to the oscillatory shear conditions used to induce alignment, the perpendicular alignment has the smaller dynamic moduli at both of the frequencies used for flow alignment (Figure 7.3). Thus, the simple notion that the system adjusts itself to minimize its resistance to flow [9] cannot describe the 'flipping' of alignment direction that is observed in PEP-PEE-2. Instead, it is likely to be dictated by a change in the time scale of the flow with respect to a characteristic time scale of the BCP dynamics [5]. Among the characteristic frequencies exhibited by the unaligned BCP ($\omega'_{c,so}$, $\omega''_{c,so}$, ω'_c, ω''_c and ω_x), the one that lies between the frequency used to produce parallel alignment (0.02 rad/s) and that used for perpendicular alignment (1 rad/s) is $\omega''_{c,so}$. Here, it is tempting to speculate that the mechanism of parallel

alignment overcomes that of perpendicular alignment when the viscoelastic behavior is dictated by microstructural dynamics (*i.e.*, $\omega < \omega''_{c,so}$). At higher frequencies and near the ODT, the mechanism that leads to perpendicular alignment dominates, perhaps due to the dynamics manifested by $\omega'_{c,so}$. At yet higher frequencies ($\omega > \omega_x$) that only probe chain entanglement, it is likely that another regime of behavior will be found; we expect no alignment to occur there, because the excited modes are so local and the viscoelastic properties of PEP and PEE are so similar. Certainly, further experiments are required to identify cross-over frequencies between different regimes of behavior and their relationship to the characteristic frequencies of the BCP [33].

In generalizing the results obtained for PEP-PEE-2, it is necessary to note that some aspects of its behavior are not universal. In a lamellar 12k-9k PS-PI diblock, Winey *et al.* [14] do not find a low-frequency regime of parallel alignment below the range where perpendicular alignment is observed. On the other hand, they find that parallel alignment occurs at a frequency well into the Rouse-like regime. In this regime, parallel alignment may be a consequence of the viscoelastic contrast between the lamellae and may require that chains not be entangled.

7.5.3 Development of Parallel Alignment

The decay in the amplitudes of both σ_{12} and n_{12} during the parallel alignment process (Figure 7.5) can be described by a double exponential with time scales of approximately 480 s ($\sim$ 1.5 cycles) for the fast mode and 4000 s ($\sim$ 13 cycles) for the slow mode. During the first several hundred seconds, the stress and birefringence

amplitudes decrease together and the stress-optic ratio SOR is essentially constant (Figure 7.6c). In contrast, the magnitude of the slow decay is much greater in n_{12} than in σ_{12}; this is manifested by a decrease in SOR (Figure 7.6c).

The large decrease in $|B^*_{eff}|$ while $|G^*_{eff}|$ is barely changing ($t > 4000$ s, Figures. 7.6a,b) indicates that there exists a mode of dynamic response associated with a large dynamic birefringence per unit energy relative to the birefringence associated with distortion of chain conformation. This mode of dynamic response is eliminated progressively during flow alignment. The increase in the magnitude of the displacement of $n_{11} - n_{22}$ during the first 10,000 s is correlated with the decrease in the amplitude of n_{12} [34]. The development of the $n_{11} - n_{22}$ component of birefringence is consistent with the enhancement of parallel alignment determined previously by SANS.

One possible interpretation of the behavior of σ_{12}, n_{12} and $n_{11} - n_{22}$ involves inhomogeneous deformation within a polydomain-ordered BCP, as has been observed in smectic liquid crystals [30]. In layered liquids, two factors can give rise to inhomogeneous deformation: one is the variation in the local shear modulus due to variation in lamellar orientation, the other is the presence of focal conics that act as rigid structures suspended in the material. Due to the orientation dependence of the viscoelastic properties, oscillatory shear could produce a 'wagging' or 'rocking' of the lamellar normal, particularly the projection in the plane of the flow (1,2-plane). The amplitude of this rocking depends on the local orientation of the lamellae.

Over the course of one cycle, the rocking of the normal may not be completely

reversed, as can be illustrated by considering a region with lamellar normal along the flow direction ($\hat{\mathbf{n}}$ //$\mathbf{v}$). As discussed above, such a region is rigid relative to the mean field around it, which initially consists of isotropically-oriented lamellar domains and various defect structures. The region with $\hat{\mathbf{n}}$ //$\mathbf{v}$ will behave initially like a rigid particle embedded in the medium and will rotate. As it rotates, its effective modulus will decrease. This decrease in stiffness reduces the tendency of the domain to rotate rather than deform. At the end of the cycle the component of $\hat{\mathbf{n}}$ along $\mathbf{v}$ is less than unity, and the orientation distribution of the surrounding material is no longer isotropic. Due to both of these factors, the reverse cycle of strain does not produce a reversal in the trajectory of $\hat{\mathbf{n}}$. In particular, this region is expected to be less rigid than it was in its initial orientation, and smaller forces are expected to act on its periphery; therefore, this region is expected to rotate 'back' to a lesser extent than it rotated 'forward' during the first half-cycle of strain. Thus, the net effect of one cycle of strain is to reduce the component of $\hat{\mathbf{n}}$ along $\mathbf{v}$, increasing the component along the velocity gradient.

This picture of irreversible rocking can be applied to arbitrarily-oriented regions and used to explain progressive alignment induced by subsequent cycles of strain. This schematic view of the microrheology of parallel alignment is consistent with the decrease in dynamic birefringence n_{12} and its correlation with the increase in the displacement of $n_{11} - n_{22}$. Further, it is plausible that inhomogeneous deformation could produce larger dynamic birefringence per unit of stress than is associated with distortion of chain conformation, because the rocking of a whole domain can contribute

strongly to the birefringence for a small energy cost per unit volume, since only the material at the periphery is distorted. The monotonic decrease in the inhomogeneity of the deformation as alignment occurs is also consistent with the monotonic decrease in the stress-optic ratio, ultimately to the level associated with the distortion of chain conformation (Figure 7.6c). Comparison of the moduli at small strain (arrows at the margins of Figure 7.6a) with those observed at 90% strain shows that the nonlinear dependence on strain is modest for the conditions that produce parallel alignment. This is consistent with the flow being so slow that the microstructure is not highly perturbed, allowing domains to respond as dictated by their local orientation and immediate surroundings. Later this will be compared to the quite different behavior that leads to perpendicular alignment.

This conceived model is consistent with the observation of Bates and co-workers [5] that a sample, having been previously aligned perpendicular, remains in the perpendicular alignment if it is subjected to a shearing that would produce parallel alignment of an initially isotropic sample. Since the present picture of the mechanism of parallel alignment involves the biased rocking of the projection of the layer normal in the 1,2-plane, it would have no effect on a sample that has $\hat{\mathbf{n}}$ along the vorticity axis. Finally, it is consistent with the SANS patterns observed for parallel aligned samples, which showed that the parallel orientation is enhanced, but perpendicular alignment also remains. In the present view of the dynamics of parallel alignment, the projection of the layer normal along the vorticity axis is largely unaffected by the process. The presence of this orientation in the initial isotropic distribution is carried

through to the final parallel aligned state.

The notion of irreversible rocking of grains does not address the detailed dynamics of defects in the system. Winey *et al.* [14] have shown that flow-induced alignment is associated with a reduction in the number of wall and focal conic defects in a lamellar diblock copolymer (SI 12/9) [13]. While wall defects might be eliminated by rotation of adjacent domains, focal conic defects can be eliminated only by local rupture of lamellae. This indicates that 'grain rotation' alone cannot completely explain the annihilation of defects that occurs during the process.

Regarding the possibility of relaxation upon cessation of flow, in PEP-PEE-2 when large-amplitude shearing is interrupted and resumed, the stress and birefringence responses resume with essentially the same amplitudes and displacement just as they had before the interruption. No evidence of relaxation has been observed. This is unlike the behavior reported recently [13] for a 12k-9k polystyrene-polyisoprene lamellar diblock copolymer in which the dynamic modulus recovers after cessation of shearing at an amplitude large enough to induce parallel alignment [35].

7.5.4 Development of Perpendicular Alignment

At a frequency of 1 rad/s, the value of G' of the perpendicular state is more than an order of magnitude smaller than that of the unaligned state (Figure 7.3a), and the ratio of G'_{so}:G' is one-fifth as large as in the unaligned material (Figures 7.2 and 7.4). This leads one to expect a ten-fold drop in G'_{eff} during flow alignment, and an even greater reduction in B'_{eff}. However, there is only a four-fold decrease in G'_{eff}, and

B'_{eff} and G'_{eff} decrease in a similar manner during the first 4000 s. The discrepancy between what is expected based on the small strain behavior ($\gamma_o \leq 2\%$) and what is observed during flow alignment can be understood in light of the strain dependence of B' and G'. During the very first cycle of large amplitude strain, G'_{eff} is immediately one-tenth as large as G' (shown by the arrow labeled G' on the vertical axis at $t = 0$). Almost all of the enhancement of G' due to the microstructure of the unaligned sample is lost at high strains. Consequently the alignment of the microstructure has a much smaller effect on $G'_{eff}(1rad/s)\gamma_o = 90\%$ than expected, based on $G'(1$ rad/s) ($\gamma_o \leq 2\%$). In relation to the notion that flow alignment is driven by the tendency of the fluid to minimize its resistance to flow, there is negligible driving force for alignment during this process.

In contrast to the parallel alignment process, during which the amplitude of n_{12} decreases much more than that of σ_{12}, the magnitude of the two decrease proportionately during perpendicular alignment (Figures 7.7a, b). The amplitude-based stress-optic ratio SOR during the process is nearly equal to C_{eff} determined at high frequency ($\omega > \omega'_{c,so}$) and small strain amplitude. This is expected because the stress is dominated by the loss component and the frequency of prolonged shear falls above ω''_{so} in the region where the loss modulus is dominated by molecular rather than microstructural relaxation (Figure 7.2); therefore, G''_{eff} and B''_{eff} are expected to be insensitive to flow alignment and remain proportional.

The magnitude of the displacement of $n_{11} - n_{33}$ increases with time, consistent with the SANS observation that similar conditions induce perpendicular alignment.

The increase in $n_{11} - n_{33}$ also appears bimodal with a fast time scale of roughly 100 s and a slow time scale of ~ 400 s. The sharp initial rise in $n_{11} - n_{33}$ correlates with an abrupt drop in G'_{eff} and B'_{eff}. On the longer time scale, there is a significant increase in $n_{11} - n_{33}$, while G^*_{eff} and B^*_{eff} remain almost unchanged. That G^*_{eff} and B^*_{eff} are insensitive to lamellar alignment is consistent with observation that both appear to be dominated by polymeric rather than microstructural contributions under the flow conditions that produce perpendicular alignment. Under such conditions, if the behavior of $n_{11} - n_{33}$ was not observed, the plateau in G^*_{eff} and B^*_{eff} might be interpreted incorrectly as indicating that the alignment of the microstructure is no longer changing.

7.5.5 Static Birefringence of Aligned Samples

The magnitude of the $n_{11} - n_{33}$ birefringence in the perpendicular-aligned sample and the magnitude of the $n_{11} - n_{22}$ birefringence of the parallel-aligned sample are comparable to each other, with that of the perpendicular sample being somewhat higher than that of the parallel sample. This is consistent with earlier SANS results [5] showing that the degree of alignment is higher in perpendicular than in parallel PEP-PEE-2. Both aligned samples have static birefringence that is orders of magnitude smaller than an estimate of $\Delta n \approx 7 \times 10^{-4}$, based on analysis of strongly-segregated lamellar BCPs applied to the case of PEP-PEE-2 [20]. As a result of the small refractive index difference between PEP and PEE ($n_{PEP} = 1.48$, $n_{PEE} = 1.487$), the intrinsic contribution dominates this birefringence (intrinsic:form $\approx$ 40:1). Since the

static birefringence of PEP-PEE-2 is dominated by the segmental orientation distribution, the discrepancy between the theoretical and observed birefringence suggests that in the weakly-segregated conditions of our experiments the chains are much less oriented with respect to the interfaces of the lamellae than they would be in the strongly-segregated state assumed in the Lodge-Fredrickson analysis [20].

7.6 Conclusions

This study demonstrates that stress-optical measurements can provide valuable information regarding both the effect of lamellar alignment on the dynamics of ordered BCPs and the development of the flow-induced alignment of their microstructure. In PEP-PEE-2 at conditions near the ODT, the behavior of the shear stress and birefringence during the process suggest that parallel alignment is associated with the irreversible rocking of domains in the material, while perpendicular alignment occurs under conditions in which the microscale deformation is essentially homogeneous. The selection of the direction of flow alignment of PEP-PEE-2 is not dictated by the orientation that minimizes the modulus, nor is the progress of alignment always manifested by a decrease in the magnitude of the shear stress. Both for parallel and perpendicular cases, much of the alignment is induced by a 'fast' process on a time scale that is comparable to the period of the oscillatory shear. During this fast process the dynamic birefringence and stress decrease together. The degree of alignment improves further on a much longer time scale (an order of magnitude slower than the 'fast' process), but this change is hardly manifested in the macroscopic mechanical

properties.

Because these rheo-optical measurements are performed in real-time, *in situ* they are well suited to screening many conditions of frequency and temperature in an efficient manner. Thus, it is natural to apply this approach to determine the cross-over frequencies from one direction of alignment to another, the effect of χN on these cross-over frequencies, and the characteristic time scales or strain scales that control the rate of alignment and their dependence on ω, γ_o and χN. The influence of entanglement and viscoelastic contrast between the lamellae should also be explored, with the goal of understanding the differences in the observed behavior between PEP-PEE and PS-PI. These issues are central to understanding the mechanisms of flow alignment, which would ultimately permit the design of BCPs for applications or processing strategies that take advantage of 'flipping'.

Bibliography

[1] Aggrawal, S.L., ed. *Block Copolymers:* Plenum Press: New York, **1979**.

[2] Bates, F.S.; Fredrickson, G.H.;. *Annu. Rev. Phys. Chem.* **1990**, *41*, 525.

[3] Bates, S. *Science* **1991**, *251*, 898.

[4] Leibler, L. *Macromolecules* **1980**, *13*, 1602.

[5] Koppi, K.; Tirrel, M.; Bates, F.S.; Almdal, K, Colby, R.H.; *J. Phys. II* **1992**, *2*, 1941.

[6] Koppi, K.; Tirrel, M.; Bates, F.S.; *Phys. Rev. Lett.*, **1993**, *70*, 1449.

[7] Keller, A.; Pedemonte, E.; Willmouth, F.M. *Colloid Polym. Sci.*, **1970**, *238*, 25.

[8] Folkes, M.J.; Keller, A.; Scalisi, F.P. *Colloid Polym. Sci.*, **1973**, *251*, 1.

[9] Hadziioannou, G.; Mathis, A.; Skoulious, A. *Colloid Poly. Sci.* **1979**, *257*, 15, 136, 344.

[10] Morrison, F.A.; Winter, H.H. *Macromolecules.* **1989**, *22*, 3533.

[11] Morrison, F.A.; Winter, H.H.; Gronski, W.; Barnes, J.D. *Macromolecules.* **1990**, *23*, 4200.

[12] Albalak, R.J.; Thomas, E.L. *J. Polym. Sci., Polym. Phys.*, **1993**, *31*, 37

[13] Winey, K.I.; Patel, S.S.; Larson, R.G.; Watanabe, H. *Macromolecules* **1993**, *26*, 2542.

[14] Winey, K.I.; Patel, S.S.; Larson, R.G.; Watanabe, H.; on "Morphology of a Lamellar Diblock Copolymer Aligned Perpendicular to the Sample Plane: TEM and SAXS," *Macromolecules* **1993**, submitted.

[15] Amundson, K.; Helfand, E.; Davis, D.D.; Quan, X.; Patel, S.S.; Smith, S.D. *Macromolecules* **1991**, *24*, 6546.

[16] a) Thomas, H.R.; O'Malley, J.J. *Macromolecules* **1979**, *12*, 323; b) Hasegawa, H.; Hashimoto, T. *Macromolecules* **1985**, *18*, 589; c) Coulon, G.; Russell, T.P.; Deline, V.; Green, P.F. *Macromolecules* **1989**, *22*, 2581.

[17] Amundson, K.; Helfand, E.; *Macromolecules*, **1993**, *26*, 1324.

[18] Bruinsma, R.; Rabin, Y. *Phys. Rev. A*, **1992**, *45*, 994.

[19] Fuller, G. G. *Ann. Rev. Fluid Mech.*, **1990**, *22*, 387.

[20] Lodge, T.P.; Fredrickson, G.H.; *Macromolecules* **1992**, *25*, 5643.

[21] Janeschitz-Kriegl, H. (1983) Polymer Melt Rheology and Flow Birefringence. Springer, New York.

[22] Bates, F.S.; Rosedale, J.H.; Bair, H.E.; Russell, T.P.; *Macromolecules* **1989**, *21*, 2557.

[23] Rosedale, J.H.; Bates, F.S.; *Macromolecules* **1990**, *23*, 2329.

[24] Johnson, S.J.; Frattini, P.L.; Fuller, G.G.; *J. Colloid Int. Sci.* **1985**, *104*, 440.

[25] Kannan, R.M.; Kornfield, J.A.; *Rheo. Acta* **1992**, *31*, 535.

[26] Kannan, R.M.; Kornfield, J.A.; Schwenk, N.; Boeffel, C.; *Macromolecules* **1993**, *26*, 2050.

[27] As the strain γ_o is increased, the higher-order harmonics (3ω, 5ω, etc.) may become important in the shear stress and the description of σ_{12} by G^*_{eff} will fail. Similarly, it will not be possible to describe n_{12} completely in terms of B^*_{eff} when γ_o is so large that higher-order harmonics become significant.

[28] The complex birefringence coefficient B^* used here is to the complex mechano-optic coefficient S^* of Lodge and Lodge [29] as the dynamic modulus G^* is to the complex viscosity η^*.

[29] Lodge, T.P.; Lodge, S.A. *Rheol. Acta* **1992**, *31*, 32.

[30] Viscoelastic measurements and video-microscopic recording of the behavior of the small-molecule smectic 8CB using rheo-microscopy (presented by Ron Larson at the Society of Rheology Meeting, February 1993).

[31] Kawasaki, K.; Onuki, A. *Phys. Rev. A* **1990**, *42*, 3664.

[32] Presentation "Toward an Understanding of Flow-Alignment of Block-Copolymers," by Scott Milner and Glen Fredrickson at the 2nd International Meeting on Relaxations in Complex Systems, Alicante, Spain, 1993.

[33] One would expect that there is a single characteristic time scale that underlies each pair of critical frequencies (ω'_c,ω''_c) and ($\omega'_{c,so}$,$\omega''_{c,so}$), because the dynamic moduli are associated with a single underlying relaxation function, and assuming that each pair is associated with a particular mode of relaxation. Indeed, the difference between (ω'_c and ω''_c is small enough that it can be attributed to the fact that changes in the near terminal part of the relaxation spectrum are manifested more strongly in G' than in G'', so they are perceptible at higher frequency in G' than in G''. However, the difference between $\omega'_{c,so}$ and $\omega''_{c,so}$ is much larger. This suggests that they arise from different dynamic modes of the polydomain BCP.

[34] At still longer times ($t > 10,000$ s), there appears to be significant baseline drift; therefore, further experiments are required to determine the behavior of $n_{11} - n_{22}$ from 10,000 to 25,000 s.

[35] The reduction in modulus observed in PS-PI 12k/9k has recently been attributed to melt fracture and its recovery due to "healing" of the sample (R. G. Larson's lecture on melt fracture at the AIChE meeting, November '93).

Table 7.1: Shift Factors and Effective Stress-Optic Coefficients of PEP-PEE-2.

T (°C)	a_T	b_T	$b_{T,so}$	$C_{eff} \times 10^{10}$ (cm^2/dyn)
22	380	1.34	1.07	1.5_6
45	35	1.20	1.02	1.4_9
65	5.4	1.09	1.00	1.3_5
87	1	1	1	1.2_4

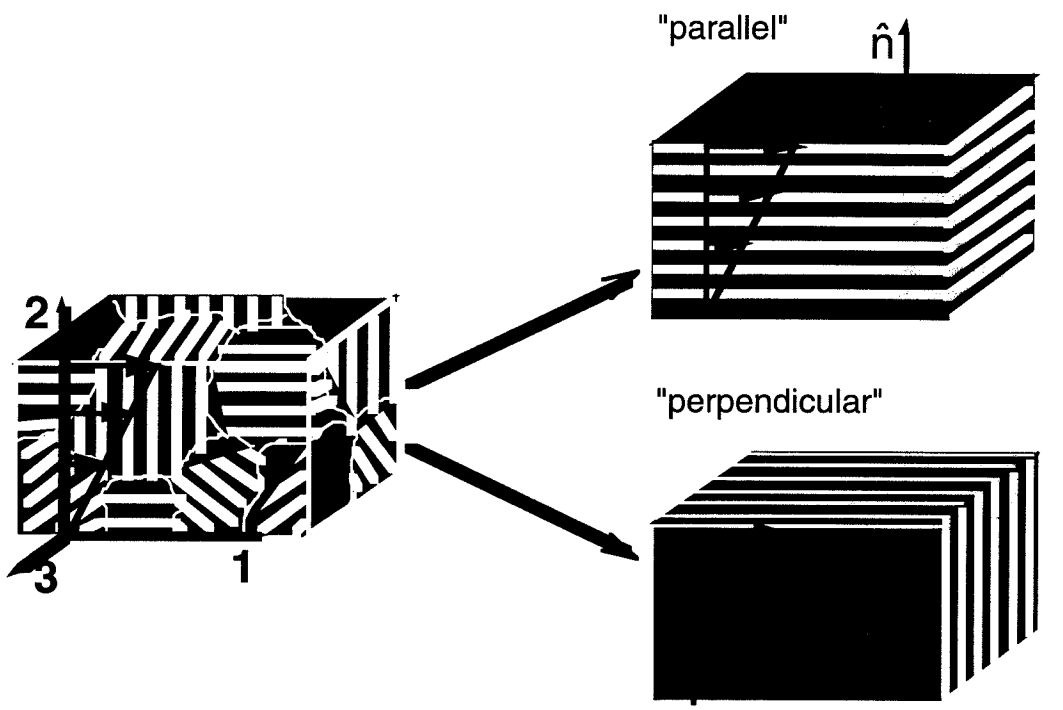

Figure 7.1: Schematic diagram of the two directions of flow-induced alignment of lamellar block copolymers. 'Perpendicular' alignment has been observed in diblock samples subjected to oscillatory shear at frequencies below the cross-over frequency ω_x at temperatures close to the ODT. 'Parallel' alignment has been observed in diblock and triblock samples after either steady or oscillatory shear over a wide range of shear rate and temperature. These cartoons are oversimplified: a rich variety of defect structures are observed, and flow enhances rather than perfects a particular direction of alignment.

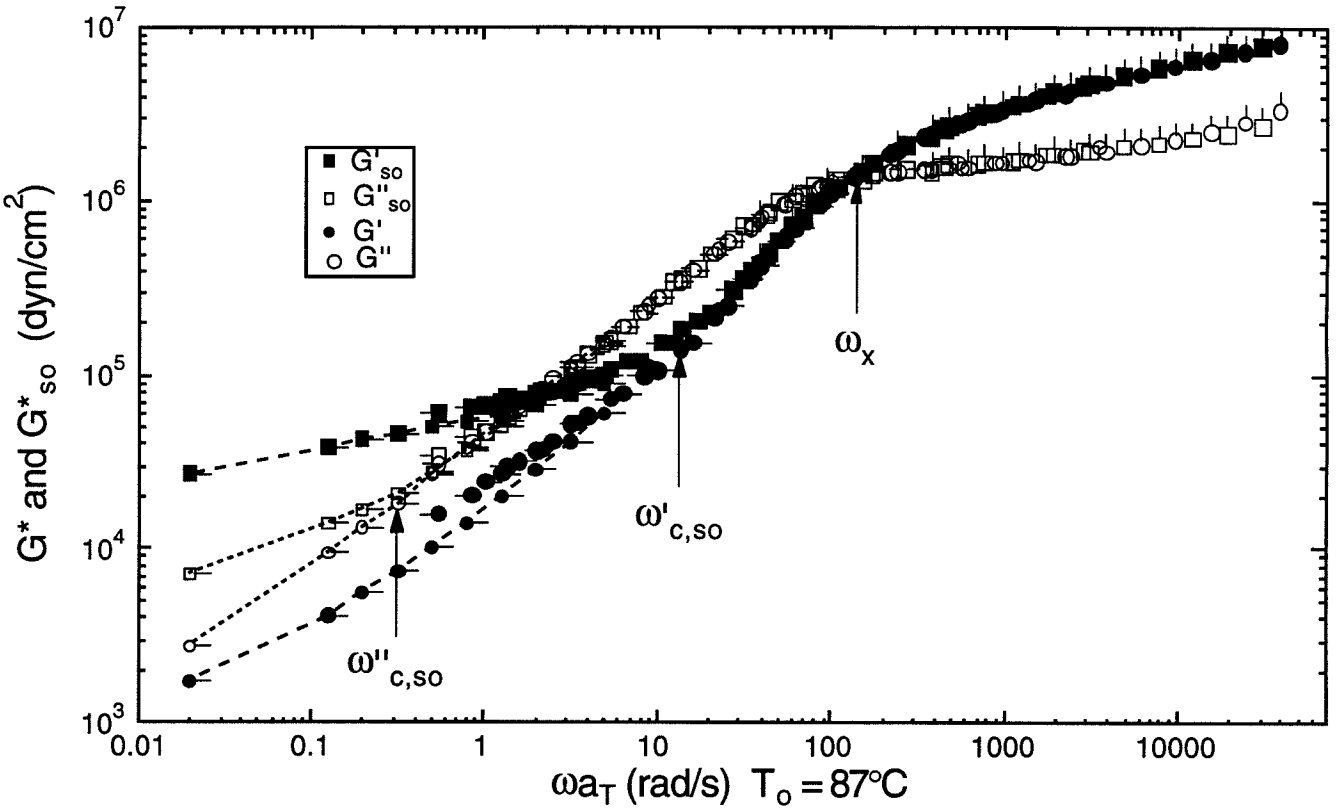

Figure 7.2: Dynamic moduli (G^*) and complex birefringence coefficient scaled by the effective stress-optic coefficient *(see text)* (G^*_{so}) of unaligned PEP-PEE-2. G' •, G'' ○, G'_{so} ■, G''_{so} □. Data at 22°C designated by vertical arm, 45°C by no arm, 65°C by left arm and 87°C by right arm. Larger symbols indicate results at strain amplitude γ_o <2%; smaller symbols connected by dashed lines indicate results with $\gamma_o = 9\%$.

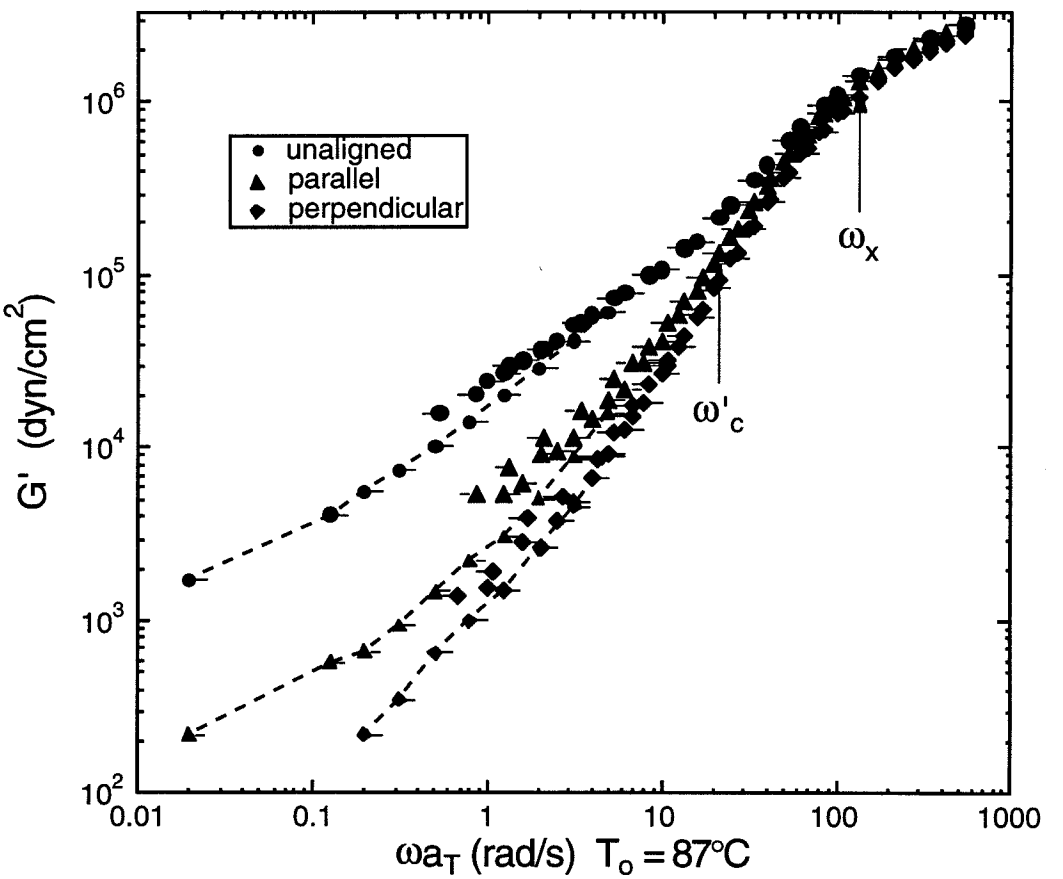

Figure 7.3a: Storage moduli of unaligned (• and ○), 'parallel' (solid △) and 'perpendicular' (solid ◇) aligned PEP-PEE-2. Data at 65°C designated by left arm and 87°C by right arm. Larger symbols indicate results at strain amplitude γ_o <2%; smaller symbols connected by dashed line indicate results with γ_o =9%.

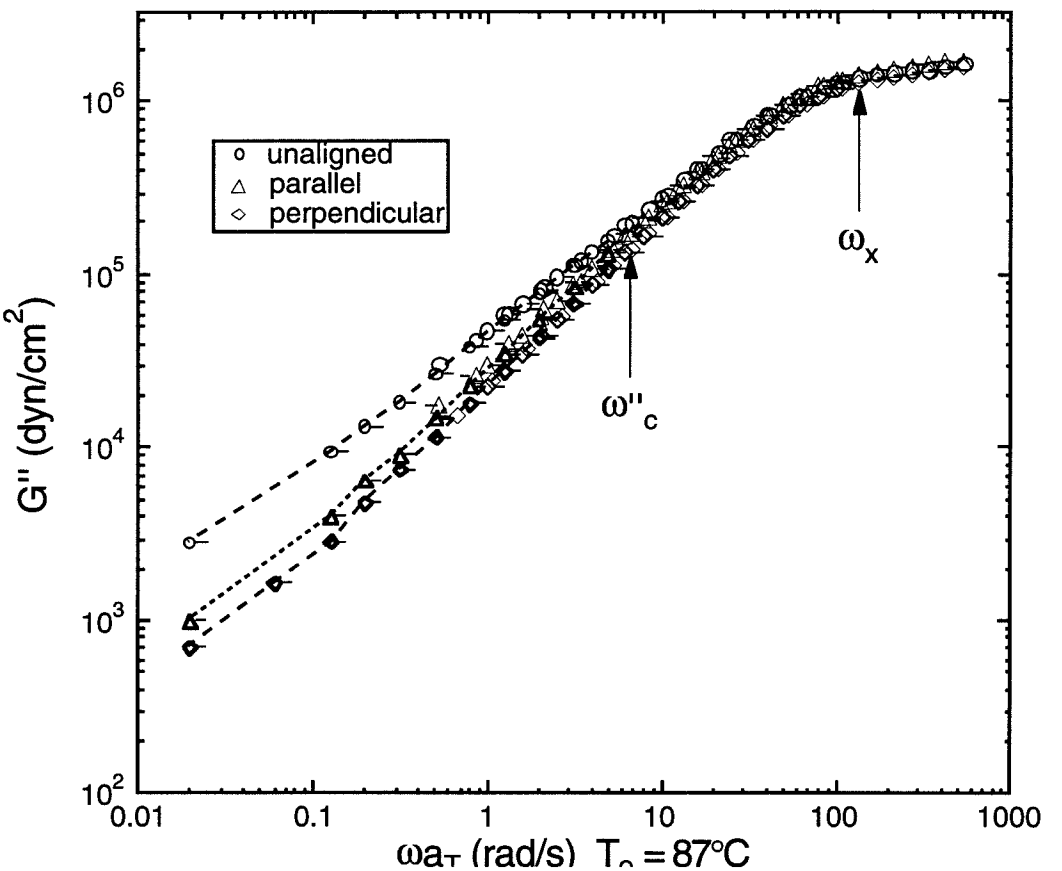

Figure 7.3b: Loss moduli of unaligned (• and ○), 'parallel' (open △) and 'perpendicular' (open ◇) aligned PEP-PEE-2. Data at 65°C designated by left arm and 87°C by right arm. Larger symbols indicate results at strain amplitude γ_o <2%; smaller symbols connected by dashed line indicate results with γ_o =9%.

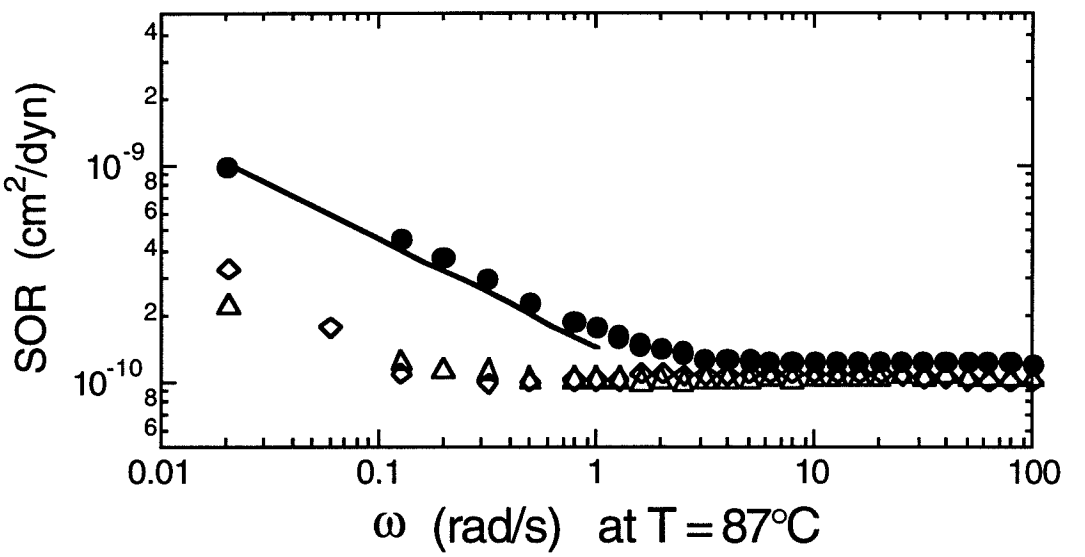

Figure 7.4: Effect of flow alignment on the stress-optic ratio SOR of PEP-PEE-2 in unaligned •, 'parallel' △, and 'perpendicular' ◇ states. For reference, the line shows a $\omega^{-1/2}$ power-law.

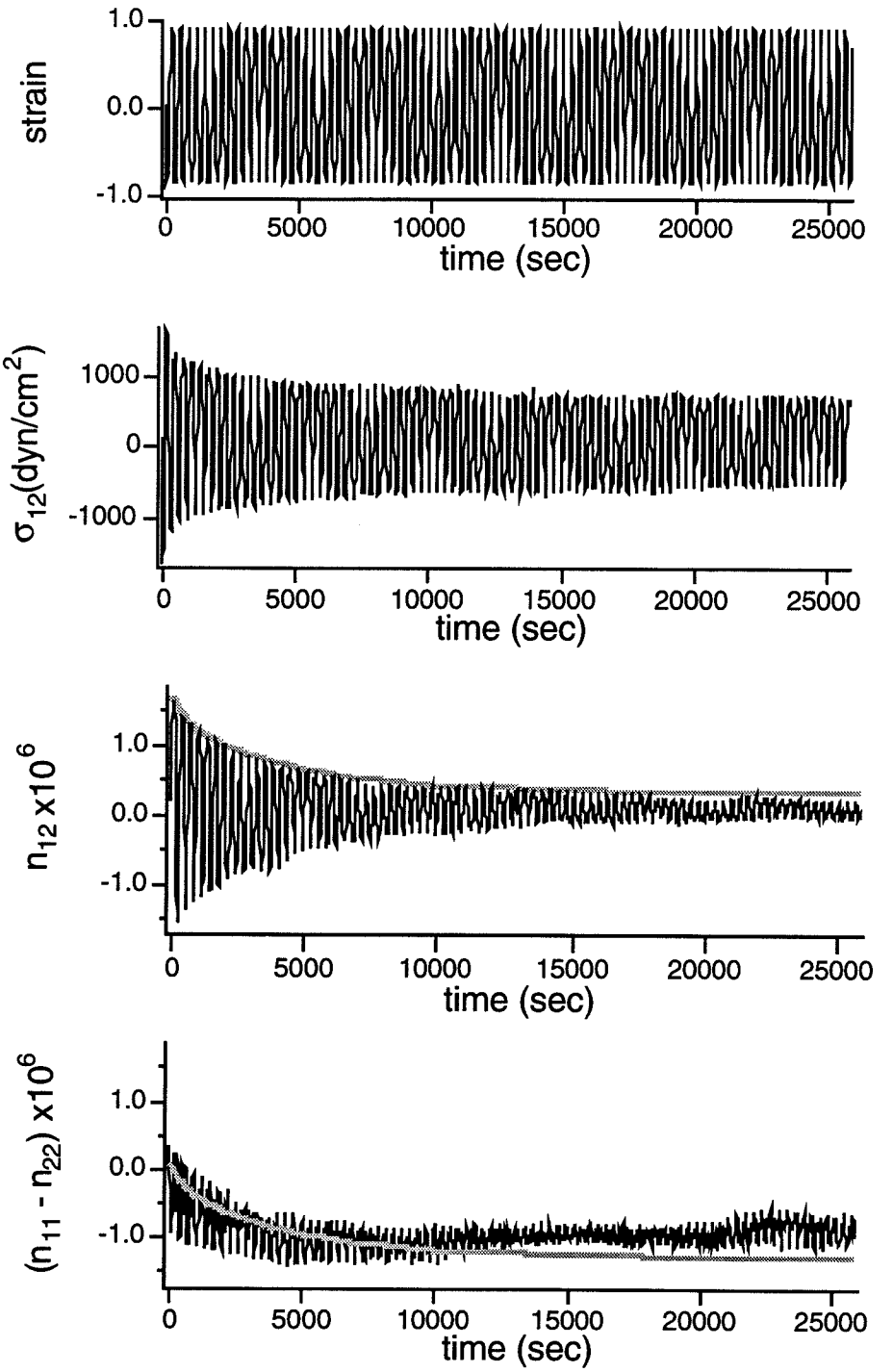

Figure 7.5: Behavior of the shear stress and birefringence in the 1,2-plane (both n_{12} and $n_{11} - n_{22}$) during 80 cycles of sinusoidal shear of $\gamma_o = 90\%$ at $T = 87°C$. Similar conditions have been shown to enhance 'parallel' alignment. The black curves connect the data points. The heavy gray curve approximates the envelope of the decaying oscillation of n_{12}. It is also shown on the graph of $n_{11} - n_{22}$ for comparison.

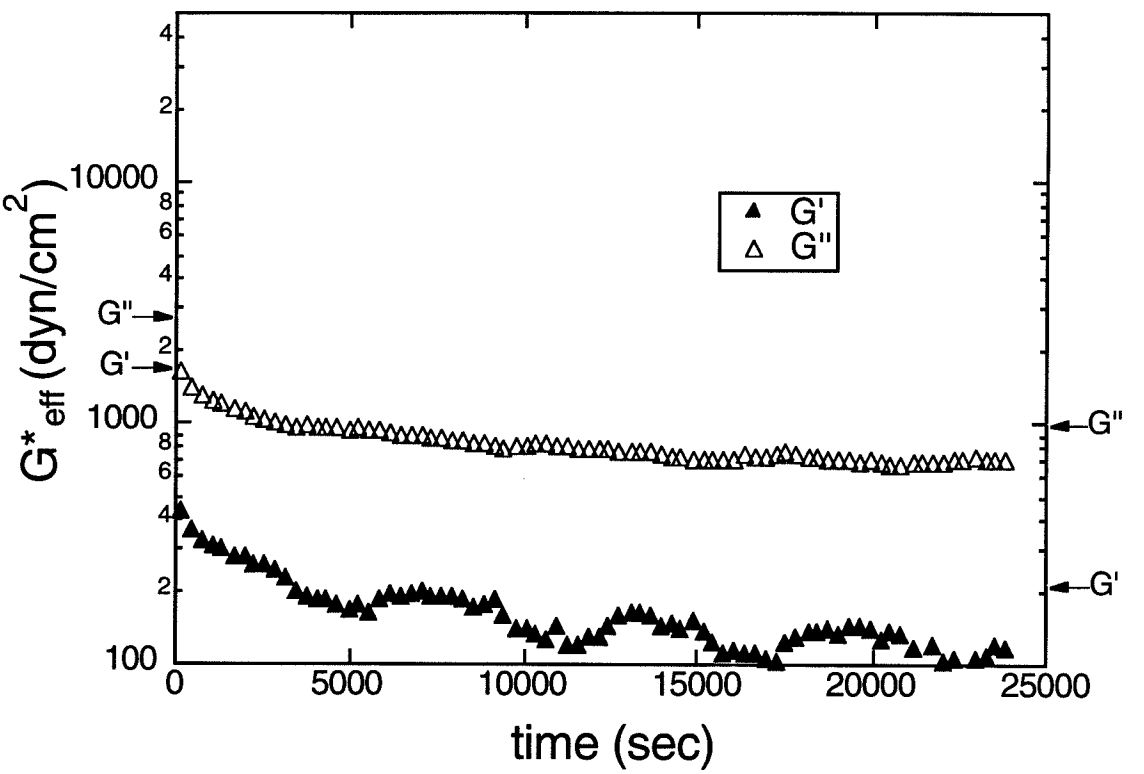

Figure 7.6a: Analysis of the shear-stress and dynamic birefringence n_{12} during the 'parallel' flow alignment process (Figure 7.5) in terms of **effective dynamic moduli**. The arrows at the left and right edges of the graph indicate the values of the dynamic moduli and birefringence coefficient observed at 0.02 rad/s with small strain (9%).

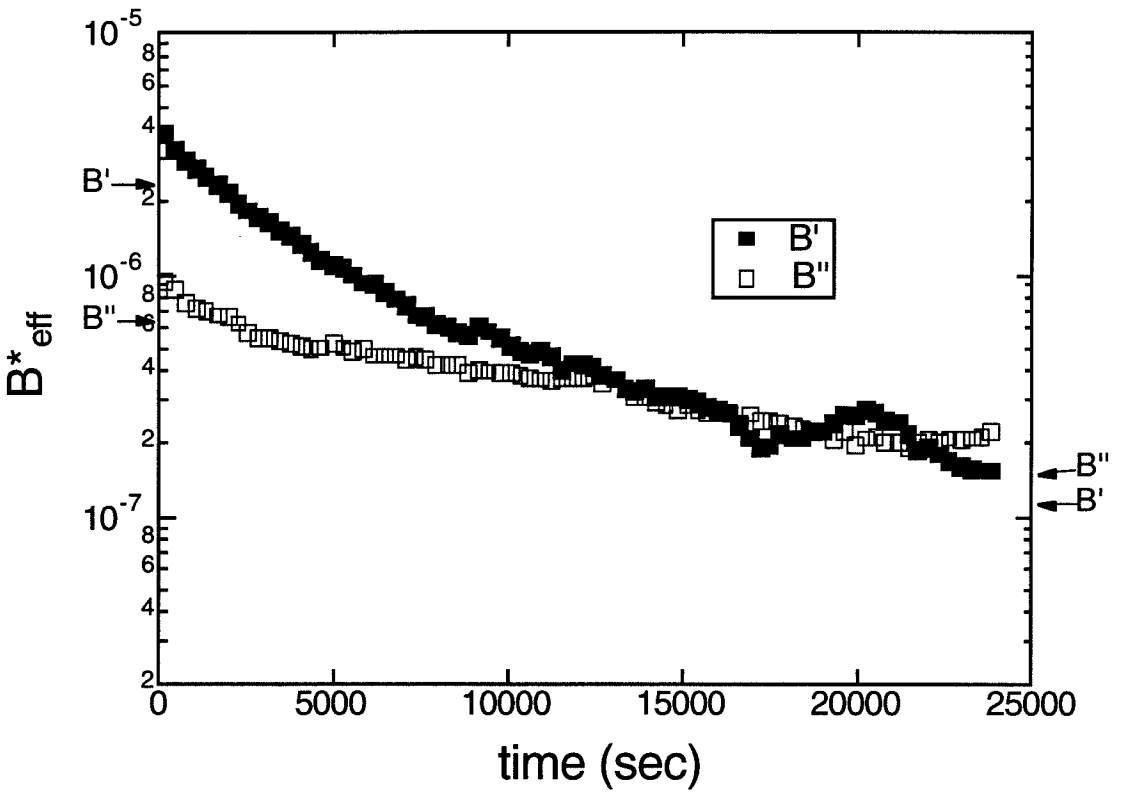

Figure 7.6b: Analysis of the shear-stress and dynamic birefringence n_{12} during the 'parallel' flow alignment process (Figure 7.5) in terms of **effective complex birefringence coefficient**. The arrows at the left and right edges of the graph indicate the values of the dynamic moduli and birefringence coefficient observed at 0.02 rad/s with small strain (9%).

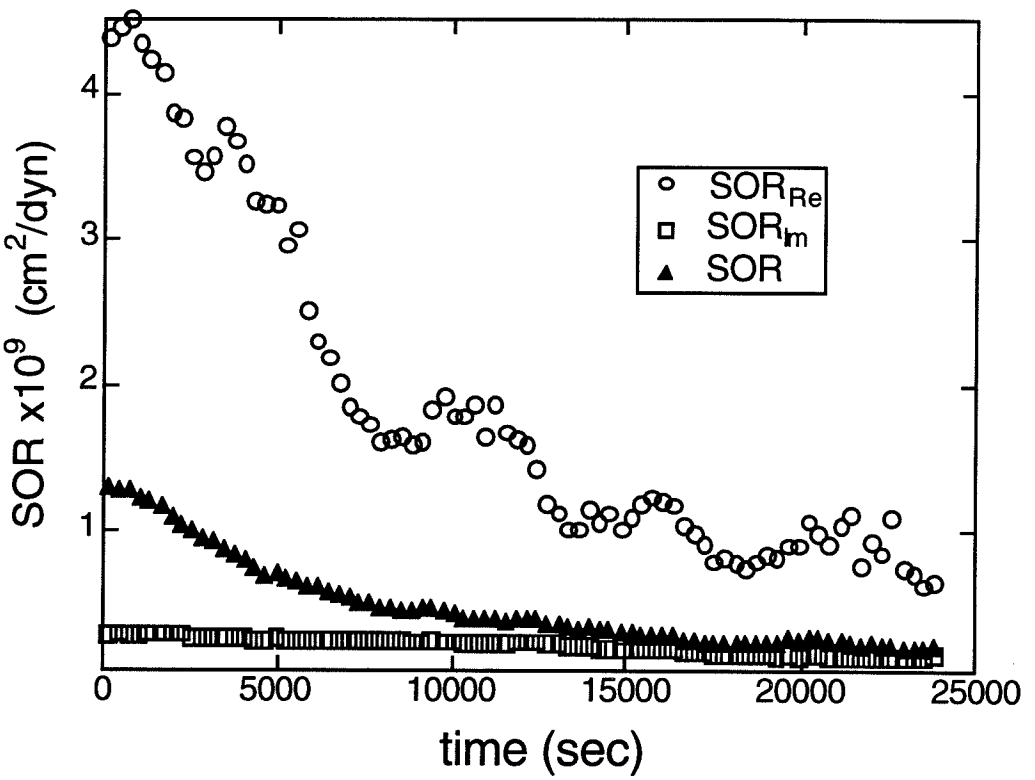

Figure 7.6c: Analysis of the shear-stress and dynamic birefringence n_{12} during the 'parallel' flow alignment process (Figure 7.5) in terms of **amplitude-based stress-optic ratio** SOR.

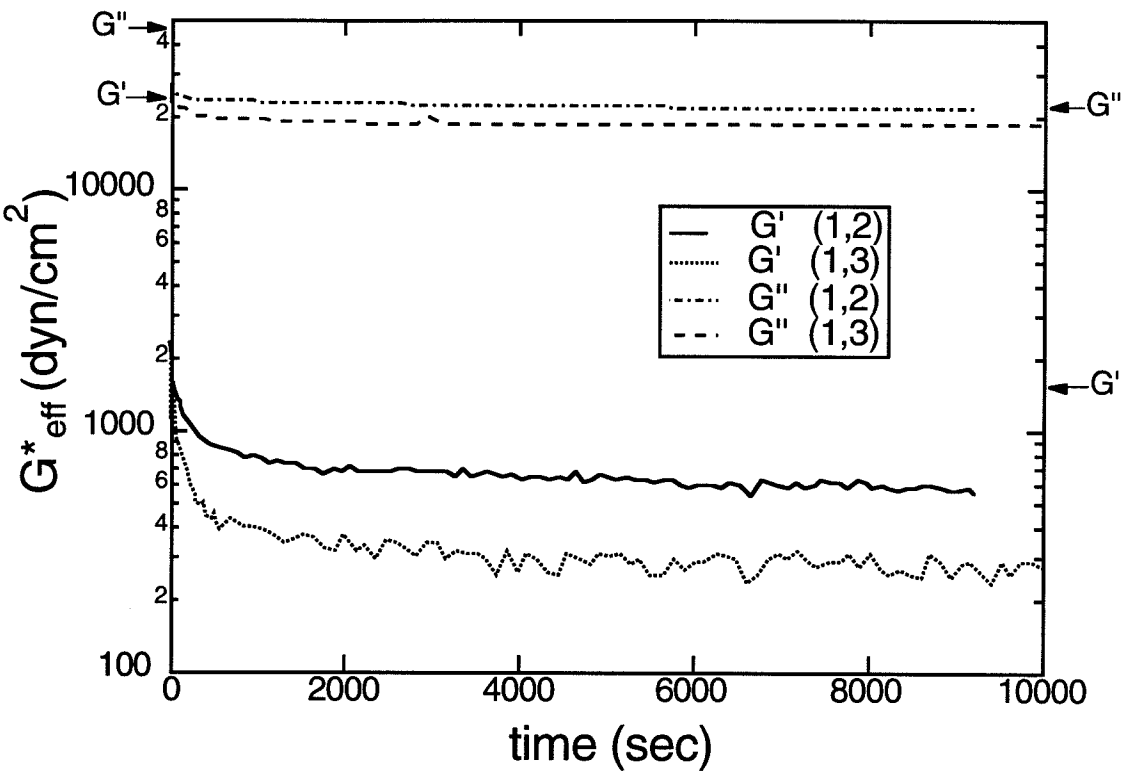

Figure 7.7a: Evolution of shear stress and birefringence during the 'perpendicular' flow-alignment process: **effective dynamic moduli**. The arrows at the left and right edges of the graph indicate the values of the dynamic moduli and birefringence coefficient observed at 1 rad/s with small strain (1%).

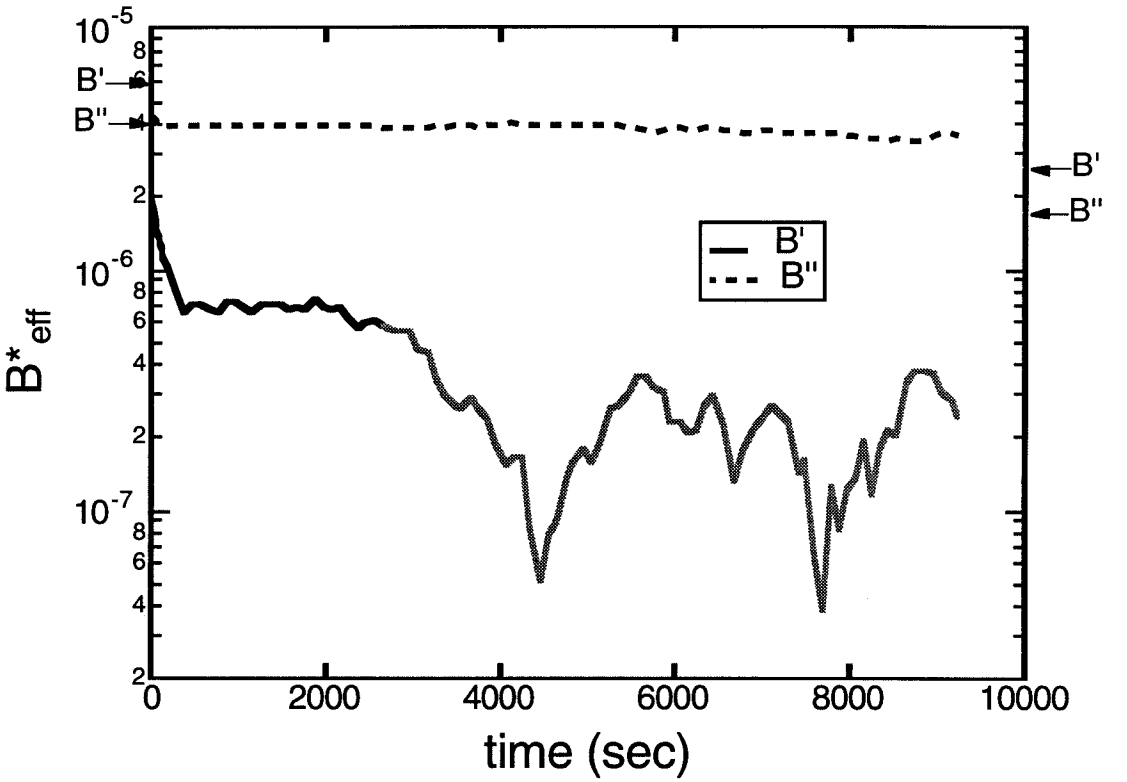

Figure 7.7b: Evolution of shear stress and birefringence during the 'perpendicular' flow-alignment process: **effective complex birefringence coefficient**. The arrows at the left and right edges of the graph indicate the values of the dynamic moduli and birefringence coefficient observed at 1 rad/s with small strain (1%).

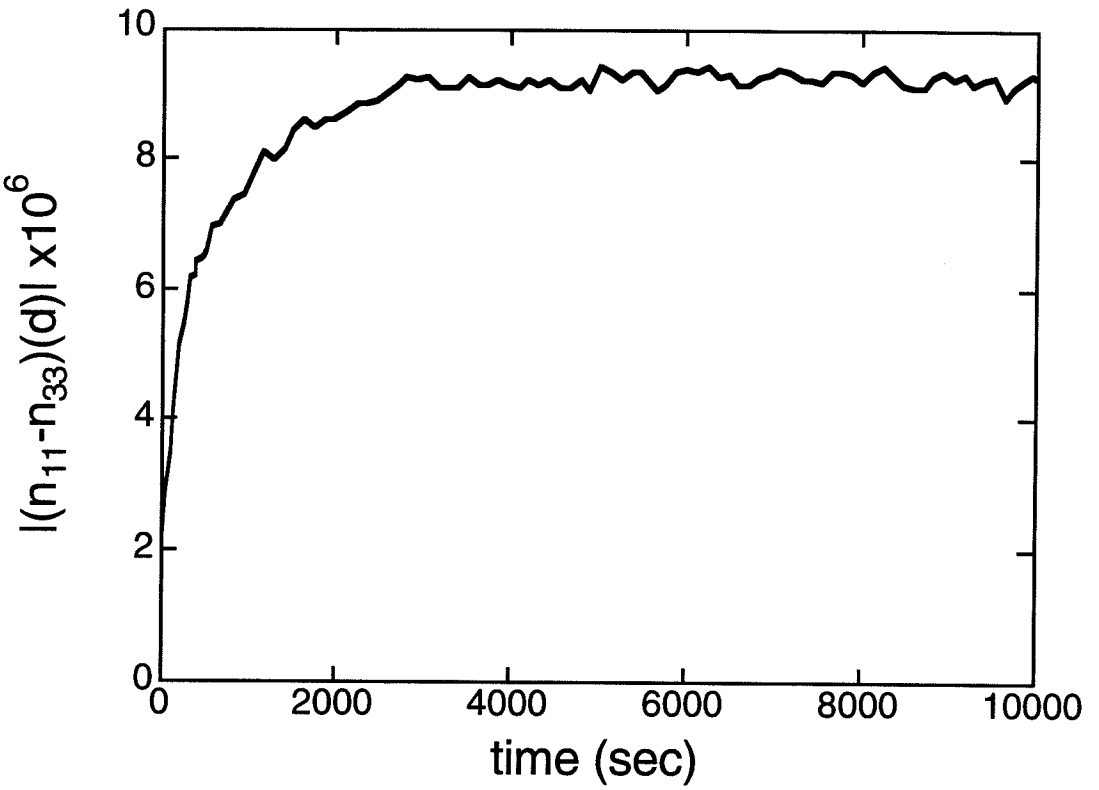

Figure 7.7c: Evolution of shear stress and birefringence during the 'perpendicular' flow-alignment process: **magnitude of the displacement component of the birefringence in the 1,3-plane** ($n_{11} - n_{33}$).. The arrows at the left and right edges of the graph indicate the values of the dynamic moduli and birefringence coefficient observed at 1 rad/s with small strain (1%).

Appendix A

The information given here is for the benefit of those interested in constructing a polarization modulation optical-rheometer using an electro-optic modulator and the optical arrangement used in the dual-axis instrument described in this article. This is intended for the rheologist who does not yet have experience with polarimetry, but is considering implementing the methods presented here.

The arrangement described below uses a quarter wave plate with a linear polarizer to serve the function of the circular polarizer that is placed after the flow cell (**CP** in Figure 2.2). The polarizer and quarter wave plate positioned before the flow cell (**P** and **Q** in Figure 2.2) are referred to as P1 and Q1, respectively. The polarizer and quarter wave plate that function as a circular polarizer (**CP** in Figure 2.2) are designated P2 and Q2. For some EO modulators it is not convenient to rotate the orientation angle of the modulator about the optical axis. Here it is assumed that its angle is fixed at +45°. (A slightly different procedure would be used for modulators that can be rotated.)

Align the laser so the beam is normal to the flow cell. If the laser is polarized, rotate its polarization so it is at 0°. Position P1 so it is normal to and centered on the beam. Rotate it about the optical axis so that its orientation is at approximately 0°. (Later its orientation will be set precisely with respect to the modulator.) Align the detector and view the detected intensity on an oscilloscope. Align the second polarizer. Note the intensity transmitted through the optical train when P2 is parallel to P1. Rotate P2 to extinguish the transmitted beam.

Next align the modulator so that it is centered on and coaxial with the laser beam.

Turn the modulator driver on and drive it with a saw-tooth wave form. Increase the amplitude of the saw-tooth until you are close to the manufacturer's specification for $\pm V_\pi$. The time dependence of the detected intensity approaches a smooth sinusoidal oscillation as the amplitude of the saw tooth voltage reaches $2V_\pi$. The minimum of this sinusoid should nearly equal the baseline signal observed when the beam is blocked. The peak intensity should nearly equal the intensity observed above with P1 and P2 parallel.

The polarizers are crossed with respect to each other, but they are only approximately at $\pm 45°$ with respect to the modulator axis. To refine their relative angles of alignment, recognize that there is a small error in the orientation angles. Denote the actual orientation angle of P1 by ζ radians, and that of P2 by $\theta + \pi/2$, where ζ and θ are the small errors we wish to eliminate. The intensity transmitted by the optical train is (ideally)

$$I(t) = I_{dc}[1 - \sin 2\theta \sin 2\zeta - \cos \Omega t \cdot \cos 2\theta \cos 2\zeta], \tag{A.1}$$

where t is time and Ω is the frequency of the saw tooth modulation. Rotate the angle of each polarizer back and forth to maximize the magnitude of the oscillatory signal. The maximum will occur when ζ and θ are both zero. Send the signal to the lock-in and adjust the phase so the amplitude is all emerging on the cosine output X.

At this point, the modulator is at the correct amplitude, the lock-in phase is set so that the signal is pure X, and the polarizers are aligned with respect to the modulator and each other. The next step is to insert and align the quarter wave plates. First

mount Q2 between the flow cell and P2. To orient it parallel to the modulator axis, consider the intensity that emerges from the optical train when the orientation of Q2 in radians is $\pi/4 + \xi$, where ξ is the error we wish to eliminate. As a function of ξ the intensity emerging from the optical train, is

$$I(t) = I_{dc}[1 + \sin \Omega t \cdot \cos(2\xi) + \cos \Omega t \cdot \sin^2(2\xi)]. \tag{A.2}$$

As the quarter wave plate Q2 rotates, the phase of the signals from the lock-in will change. The $\cos\Omega t$ (X) and $\sin\Omega t$ (Y) outputs alternately pass through extrema and null values; the absolute value of all extrema are nearly equal, X is always positive and Y swings from a positive maximum to a negative minimum. The orientation that maximizes Y and nulls X is the desired angle.

Next, mount Q1 in front of the flow cell, just after the modulator. The intensity transmitted through the optical train is related to the orientation angle ϵ of Q1 by

$$I(t) = I_{dc}[1 + \cos \Omega t \cdot \sin(2\epsilon)]. \tag{A.3}$$

As the quarter wave plate Q1 rotates, Y remains nearly zero, but X swings between positive and negative extrema that have the same magnitude observed above, when rotating Q2. When both the X and Y outputs are nearly zero, the orientation of Q1 is set properly.

At this point if a purely birefringent sample (i.e., having no dichroism) with retardation μ and orientation angle χ is placed in the optical train, the transmitted

intensity is

$$I(t) = I_{dc}[1 - \sin\Omega t \cdot \sin\mu \cdot \cos(2\chi) + \cos\Omega t \cdot \sin\mu \sin(2\chi)]. \qquad \text{(A.4)}$$

Thus the cosine and sine outputs of the lock-in can be normalized by the output of the low-pass filter to determine $\sin\mu$ and $\tan(2\chi)$.

To calibrate the instrument, insert a quarter-wave plate as a sample and rotate it. When it is oriented at 0°, Y reaches a negative extremum and X is zero; when its orientation is +45°, X reaches a positive maximum and Y is zero; as it rotates to +90°, Y becomes a positive maximum; and when it is oriented at +135°, X becomes a negative extremum. The pattern repeats as you complete a full 360° cycle. All eight extrema should have equal magnitude, and ideally the ratio of the extrema to I_{dc} would be unity. Generally these ratios are less than one; use their average as a calibration point for the value of the ratio that corresponds to a retardation of $\pi/2$ (i.e., b in Eq. 2.7 is the reciprocal of the mean magnitude of these eight extrema).